

# ***Performance of a CCD tracker at room temperature***

***T. Tsukamoto (Saga Univ.)***

**T. Kuniya, H. Watanabe (Saga Univ.);**

**A. Miyamoto, Y. Sugimoto (KEK);**

**S. Takahashi, N. Tamura (Niigata Univ.);**

**K. Abe, T. Nagamine, Y. Shirasaki (Tohoku Univ.);**

**T. Aso (Toyama National College of Maritime Technology)**

1

## ***Outline***

- **Introduction**
- **HPK CCD**
- **Experimental setup**
- **Response to charged particles**
  - **S/N, detection efficiency, energy resolution**
  - **Position resolution**
- **Comparison with EEV CCD**
- **Summary**

## ***Advantage of CCD for tracking device***



- **Pixel detector**
  - unambiguous reconstruction/high granularity
- **Thin ←extremely low capacitance**
  - less multiple scattering
- **Serial readout**
  - small number of channels
- **Continuously sensitive**
  - no intrinsic limitation as regards trig. rate
- **Other R&D**
  - driven by commercial interest (video) as well as X-ray astronomer, etc.

3

## ***Vertex detector application in future LC***



- **Low repetition rate**  
~150Hz ↔ serial r/o
- **Highly collimated jets**  
↔ pixel detector
- **Backgrounds**  
↔ pixel detector

**Operation at room temp. ( $\sim 0^\circ\text{C}$ )  
⇒ compact cooling system**

- to reduce material
- to keep mechanically stable
- to avoid interference with the beam monitor

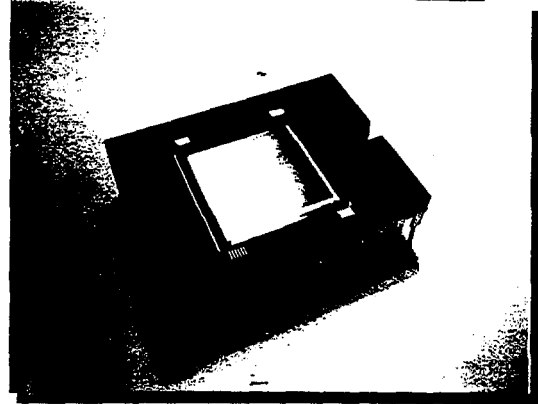
# Hamamatsu (HPK) CCD

- **Feature**

- Full frame transfer type
- 2phase CCD
- MPP operation to reduce dark current

- **Developed for scientific researches**

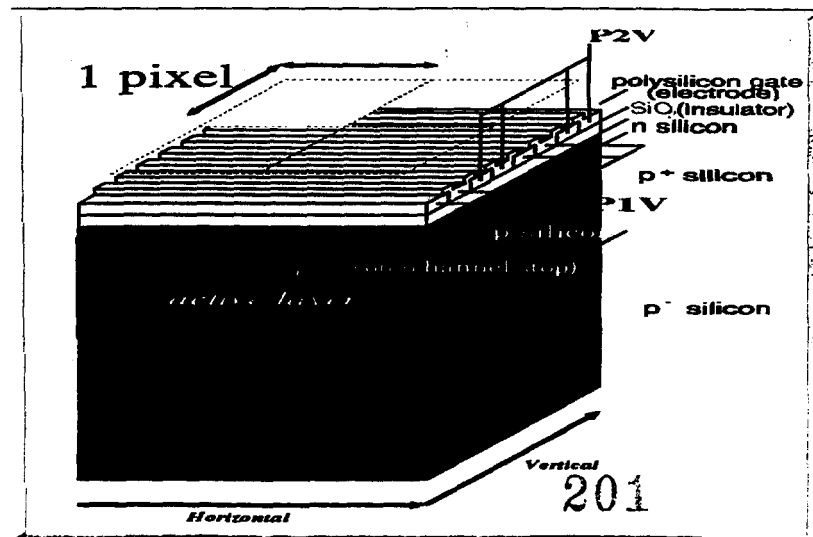
- Low light level measurements (e.g. spectroscopy)
- X-ray astronomy



⇒ **How about MIP detection?**  
Application for high energy physics  
especially at higher temperature

## Structure of CCD

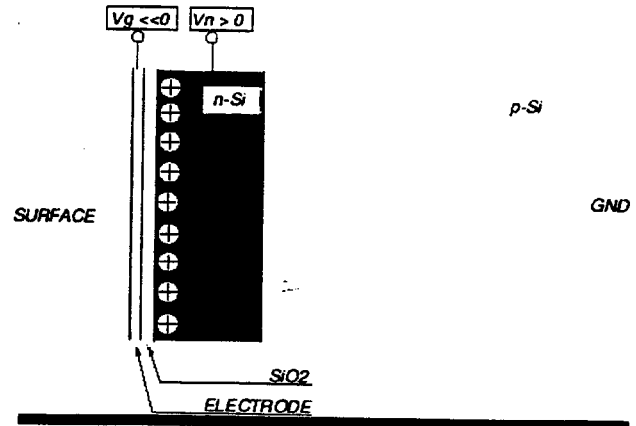
- **HPK S5466: Full Frame Transfer Type (2 phase)**



# MPP(Multi Pinned Phase) Operation

“Inverted Operation” in other words

- Holes are accumulated under Si/SiO<sub>2</sub> interface.
- Thermal excitation of electrons is significantly suppressed.



⇒ Reduction of the dark current by one order of magnitude

7

## Specification

### • CCD: Hamamatsu S5466

Type	2phase FFT-CCD
#pixels	512×512
Sensitive area	24μm×24μm
Active layer in depth	~10μm
Sensitivity	2.0μV/electron
Charge transfer eff.	>0.99995

### • Driver: Hamamatsu C5934-1010

Gain	× 5 5
H - clock	2 5 0 H z
V - clock	6 2 . 5 H z

8

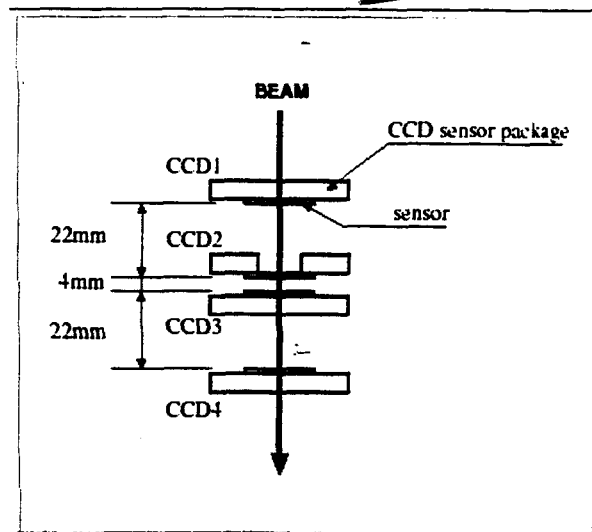
# Experimental setup

- **4 layers**

- to reduce random hits
- minimize multiple scatterings
  - a special package w/ a hole
  - CCD2 & CCD3 as close as possible

- **KEK PS T1 line**

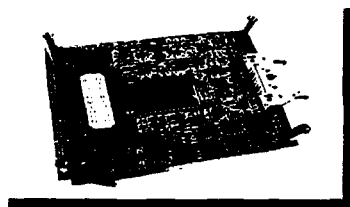
- 4 sec/cycle
- 2.0GeV, 1.0GeV, 0.5GeV ( $\pi^-$ )



9

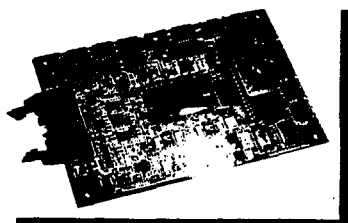
## Setup

- **Standard CCD**



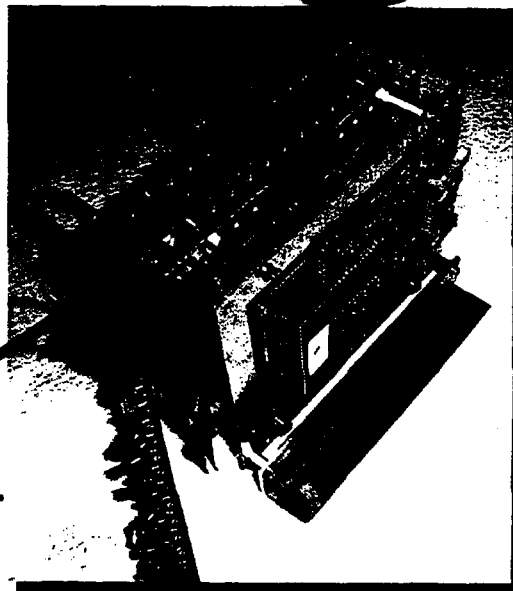
1.2mm  $\text{Al}_2\text{O}_3$  behind the chip

- **Special CCD w/ a hole**



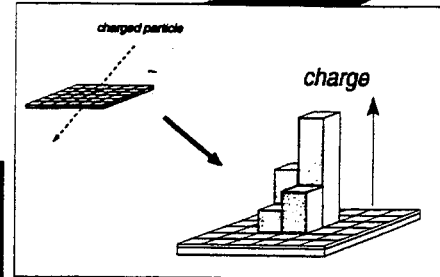
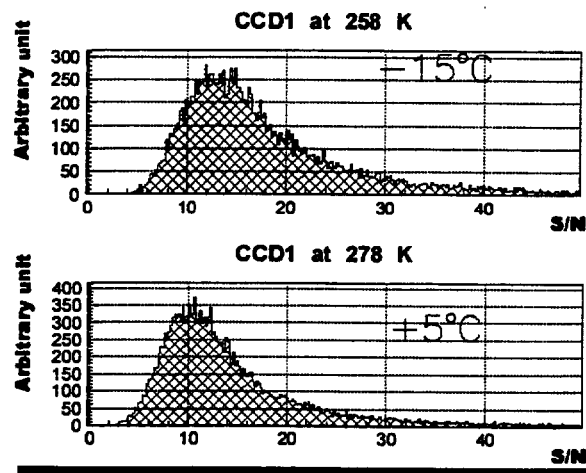
2nd layer

202



# Response to Charged Particles

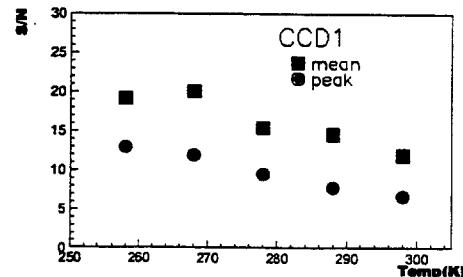
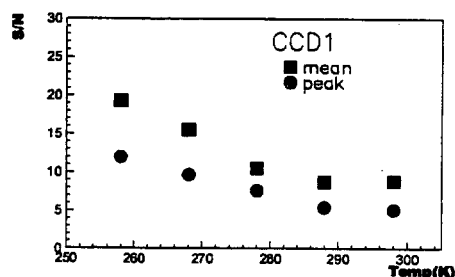
- 2x2 clustering
- S/N



11

## S/N as a function of temperature

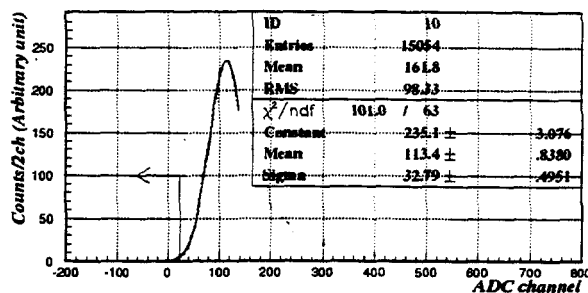
- 4sec readout cycle
- 1.3sec readout cycle



# Detection Inefficiency for MIP

- Detection inefficiency

assume Gaussian shape  
in the low energy side  
of Landau

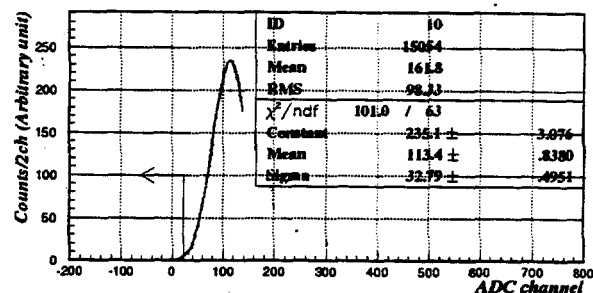


Temp.	Inefficiency (%)
-15°C	0.00 ± 0.03(stat) ± 0.03(sys.)
+5°C	0.05 ± 0.04(stat) ± 0.04(sys.)

13

# Energy Resolution for MIP

- Energy resolution



Temp.	Ereso (%)
-15°C	28.9 ± 0.5
+5°C	33.2 ± 0.5

14

# Position Resolution

- After the careful alignment...

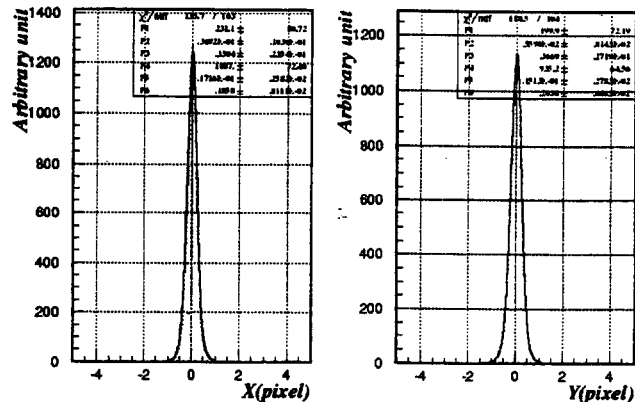


- Position resolution

Two components seen



can fit to double Gaussian



## Charge sharing ↔ Position resolution

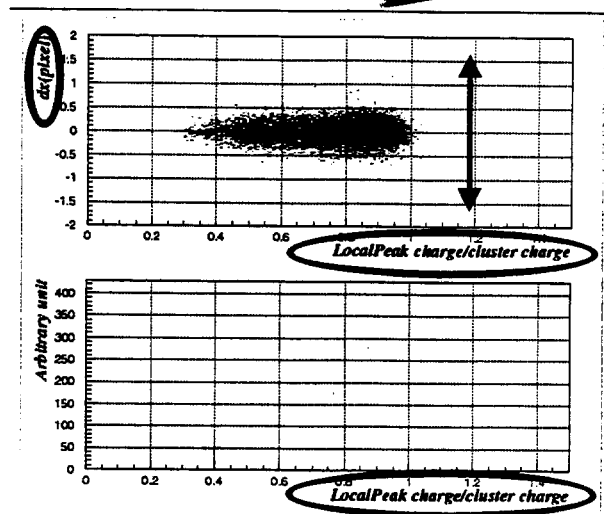
- Charge sharing



As “ratio” gets close to 1,

Position resolution gets worse.

∴  $1/\sqrt{12}$  component increases



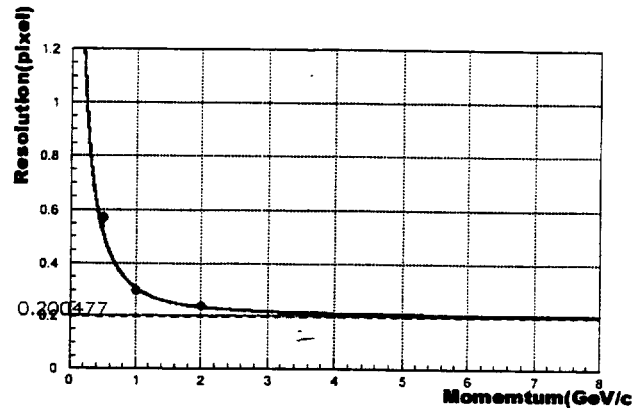


## Momemtum dependence of position resolution

- Position resolution as a function of  $p$
- Fits well to the formula (multiple scattering)

Resolution

→  $0.20 \pm 0.01$  pixel



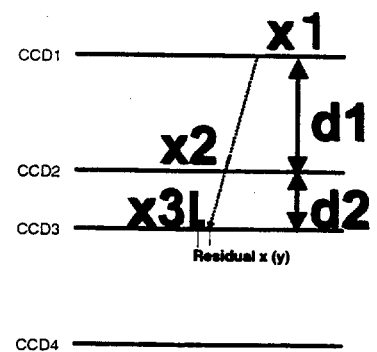
17

## Intrinsic Resolution

- Assuming all the sensors have the same resolution,

$$\begin{aligned}
 (\sigma_{\text{obs}})^2 &= (\sigma_2)^2 + \left(1 + \frac{d_2}{d_1}\right)^2 (\sigma_1)^2 + \left(\frac{d_2}{d_1}\right)^2 (\sigma_0)^2 \\
 &= 2.56 \cdot (\sigma_{\text{intrinsic}})^2
 \end{aligned}$$

$$\text{where } \sigma_{\text{intrinsic}} = \sigma_0 = \sigma_1 = \sigma_2$$



- $\sigma_{\text{intrinsic}} = 3.0 \pm 0.2 \mu\text{m}$  (weighted  $\sigma$  w/ double Gaussian)
- $\sigma_{\text{intrinsic}} = 3.6 \pm 0.2 \mu\text{m}$  (RMS)

207

18

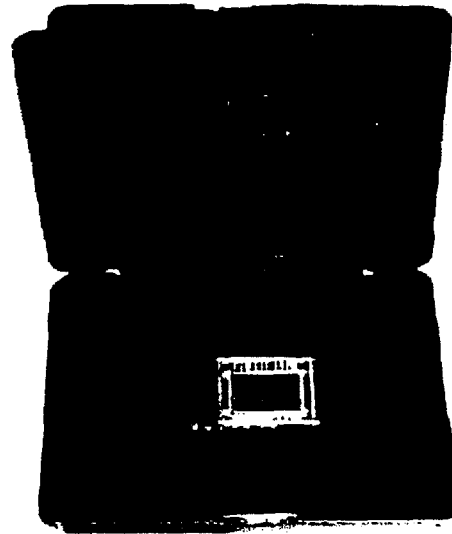
# EEV CCD

- **CCD 02-06**

- #pixels: 385(H)×578(V)
- pixel size: 22 $\mu$ m×22 $\mu$ m
- active depth: 20 $\mu$ m

- **Two operation modes**

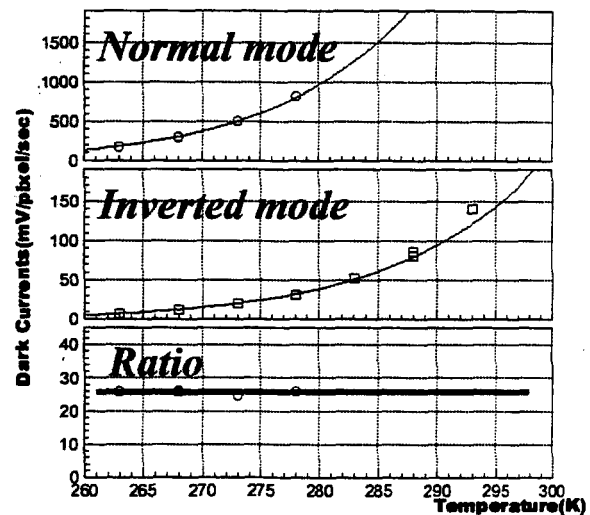
- normal mode
- “inverted mode”  
=“MPP mode” in HPK



## EEV normal mode v.s. inverted mode

- **Dark current**

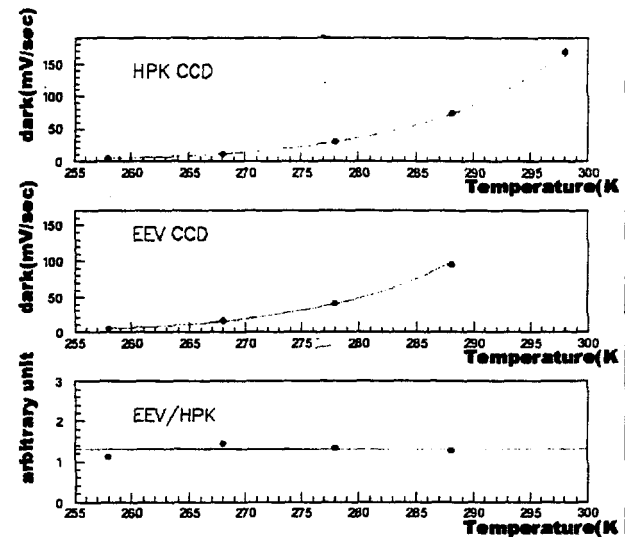
- **Suppression factor ~25**



## Comparison of the dark current

- HPK(MPP) vs EEV(inverted)
- Similar in mV  
 $EEV = HPK \times 1.3$
- But measured gain  
 $EEV = HPK \times 0.5$

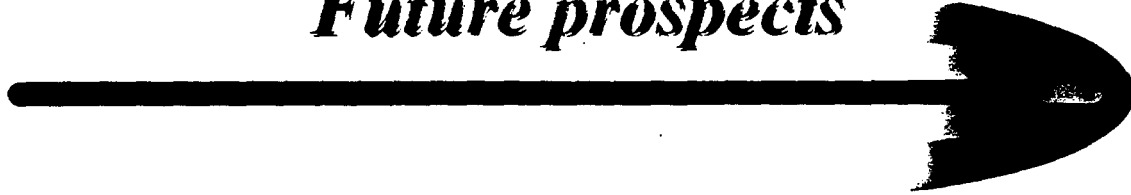
Dark current in electrons  
for CCD's under our study  
 $EEV = HPK \times 2.5$



## Summary

- MIP's are successfully detected using HPK CCD
- Operation at room temperature  $\sim 0^\circ\text{C}$ 
  - $S/N > 10$  up to  $+5^\circ\text{C}$
  - efficiency very close to 100%
  - position resolution:  $3.0\mu\text{m}$
- Comparison with EEV CCD
  - Both “MPP” and “inverted” mode suppress the dark current by one order of magnitude

## ***Future prospects***



- **Tracking performance of EEV CCD will be examined in June.**
- **Radiation damage**
  - **affects CTE(Charge Transfer Efficiency)**
  - **CTE measurements are on-going.**
  - **Irradiation with a strong  $^{90}\text{Sr}$  will take place in the near future.**

# A medical imaging system based on a GaAs pixel detector read-out by a single-photon counting VLSI electronics.

P. Maestro

*Dipartimento di Fisica and INFN, Pisa, Italy*

## Abstract

GaAs pixel detectors have been studied and tested to choose the best ones regarding charge collection properties and to improve the ohmic contacts deposition technology. With a 36-channels read-out electronics operating in single-photon counting mode, images of low-contrast details on a standard mammographic phantom have been collected, showing better imaging capabilities of this detector in comparison with the typical film-screen systems at the energy of the mammographic clinical X-rays tube.

Real application of this system in early diagnosis of the breast disease requires the extension of the detector sensitive area and the development of a VLSI read-out electronics, capable of handling many thousand channels and bump-bonded to the GaAs pixels. A front-end chip (MEDIPIX) has been designed by the CERN micro-electronics group and electric threshold measurements have been performed using a custom read-out system composed of three standard VME boards and a C language software.

## 1 Digital mammography

Radiography is based on the measurements of the differential attenuation of X-rays passing through non-uniform biological tissues. In standard radiography a photographic emulsion is used to detect the photons transmitted through the patient, together with a fluorescent screen which improves the detection efficiency. The film carries all of the information contained in the image, which is displayed as an optical density pattern [1].

The term "digital radiography" indicates systems capable of recording images in numerical form and of handling the data after the acquisition. The image is made of an array of pixels, each one associated with a grey level deriving from the analog to digital conversion of the detector signals. Then an image

processing software, improving contrast resolution and signal-to-noise ratio, allows digital radiography to obtain different views of the examined tissue with a single patient exposure and to increase diagnostic informations. Moreover the choice of a detector more sensitive to radiation than the screen-film system can reduce the dose to the patient.

Mammography in particular would largely take advantage of an improved performance in terms of contrast, due to the little difference in the X-rays attenuation coefficients between healthy breast tissues and tumourous masses (as large as few mm), which makes the early detection of the disease dramatically difficult [2].

## 2 The detector choice

Gallium Arsenide is a good candidate in the construction of a detector for medical imaging. Its high Z-number (31, 33) implies a great photoelectric absorption cross-section in the diagnostic energy range (20-60 KeV), and a consequent higher detection efficiency with respect to silicon, in spite of the fact that the latter exploits a more consolidated development technology.

At the mammography X-rays average energy (20 KeV) a GaAs 200  $\mu\text{m}$  thick detector shows a 100% efficiency, greater than either a 300  $\mu\text{m}$  thick silicon detector (about 24%) or a film-screen system (about 55%). Germanium, though being more favoured due to its higher Z, is excluded from this kind of applications because of the low required temperature operation.

Gallium Arsenide offers also the advantages of a great resistivity (order of  $10^8 \Omega \cdot \text{cm}$ ), which reduces the leakage current, and of a high electron mobility, which means faster detector response signals [3].

GaAs detectors differ for construction technique and kind of ohmic contact. These technologies are often empirically developed by industry and aim at the improvement of the charge collection and efficiency properties of the detectors.

The most used methods of growing GaAs crystals are the Liquid Phase Epitaxy (LPE) and the Liquid Encapsulated Czochralski (LEC). The LPE GaAs detectors show on one side a maximal bias independent charge collection efficiency (c.c.e.), thanks to the absence of trapping and recombination centers in the crystal (such as in silicon detectors), and on the other side a low detection efficiency, because the material built in this way is characterized by a thin depth [3, 4]. On the contrary, the LEC GaAs detectors are thicker and then more efficient, but worse regarding the charge collection properties, because of the high concentration of crystal impurities. Therefore the c.c.e. can be increased developing new ohmic contacts on LEC SI-GaAs crystals, which intensifies the electric field in the depletion region [5, 6].

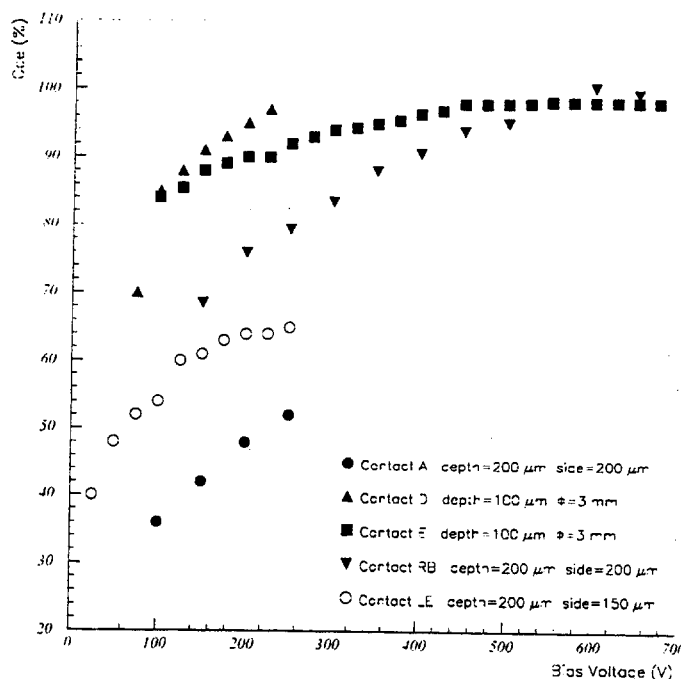


Figure 1: Charge collection efficiency as a function of the bias voltage of six GaAs detectors, differing for ohmic contact type, thickness and geometry. The measured errors are 5% on the detectors called A, RB, LE, 12% on D and E.

Concerning the read-out electronics, the approach we have considered is a single photon counting system, which allows to reach a better contrast definition than an integrating readout system ([7]). The pixel detector architecture is the most suitable topology for a 2-dimensional reconstruction of the image. Each pixel has linear dimensions of the order of hundred microns, so to meet the stringent requirement of submillimetric spatial resolution in the imaging applications, and is read-out by a corresponding electronics channel.

A first prototype of digital mammography detector has been built; it consists of a 36-pixels LEC SI-GaAs 200  $\mu\text{m}$  thick detector, with ohmic contacts studied to obtain a complete c.c.e. (fig. 1) [8, 9], and of a discrete-components electronics, where each channel has a preamplifier, a shape amplifier, a discriminator with externally adjustable threshold and a counter.

Images of low-contrast details on a standard mammographic phantom have been obtained by this system (fig. 2). It has been verified that the GaAs detector can "see" details with contrasts lower than 3%, limit achievable by traditional film-screen systems [10].

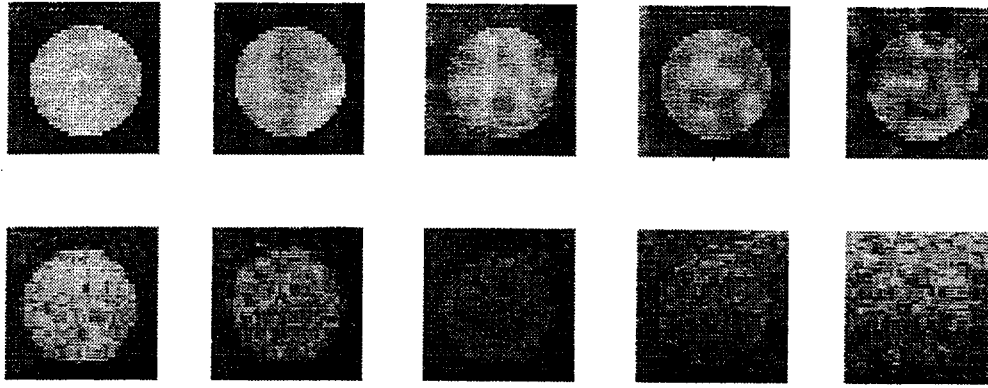


Figure 2: Details no. 1-5 from the TORMAS phantom: nominal contrast here are from left to right respectively 8.5%, 5.5%, 3.8%, 2.6% and 2.0 %. The upper images are produced with 36-pixels GaAs detector, the lower ones with a traditional film-screen system. Distance focus-detector 64 cm. Exposure 12.5 m.As.

### 3 The Front-End Electronics and Read-Out System

In order to cover surfaces of diagnostic interest a front-end chip (MEDIPIX) has been designed to read-out the GaAs detector with thousands of pixels [11]. The chip is derived from the OMEGA3 chip [12], developed at CERN. MEDIPIX contains  $64 \times 64$  square cells with side  $170 \mu\text{m}$ , each one provided with a bump-pad ( $24 \mu\text{m}$  diameter) on which the corresponding single pixel of the detector is to be bump-bonded. The chip has been built with SACMOS  $1 \mu\text{m}$  technology, by FASELEC (Zurich). The total area covered by the chip is  $1.7 \text{cm}^2$ , consequently a wider major surface can be obtained assembling many chips in ladders.

Figure 3 shows a scheme of the MEDIPIX architecture. Each channel is composed by a charge sensitive preamplifier, a comparator with an externally set threshold, a shaping delay and a 15-bit pseudo-random counter. The preamplifier receives as input, either the detector signal, via the bump-bonding pad, or a test signal from an external pulse generator.

The operation mode of each cell is configured via 5 bits. This array of  $5 \times 4096$  bits is called mask. The chip is self-triggering i.e. after a reset, the comparator is sensitive to signals larger than the threshold. In addition to a common threshold (the same for the 4096 pixels), each pixel threshold can be separately adjusted, with a 3-bit resolution, so to compensate for non-uniformities among channels (three of the five bits in the cell's mask).

Moreover 5 currents have to be externally set as analog biases to MEDIPIX: two of them are used to fix the working point of the preamplifier, one sets the length of the shaped signal, two adjust the levels of the common and single channel thresholds. The single-photon counting is performed by the chip at a



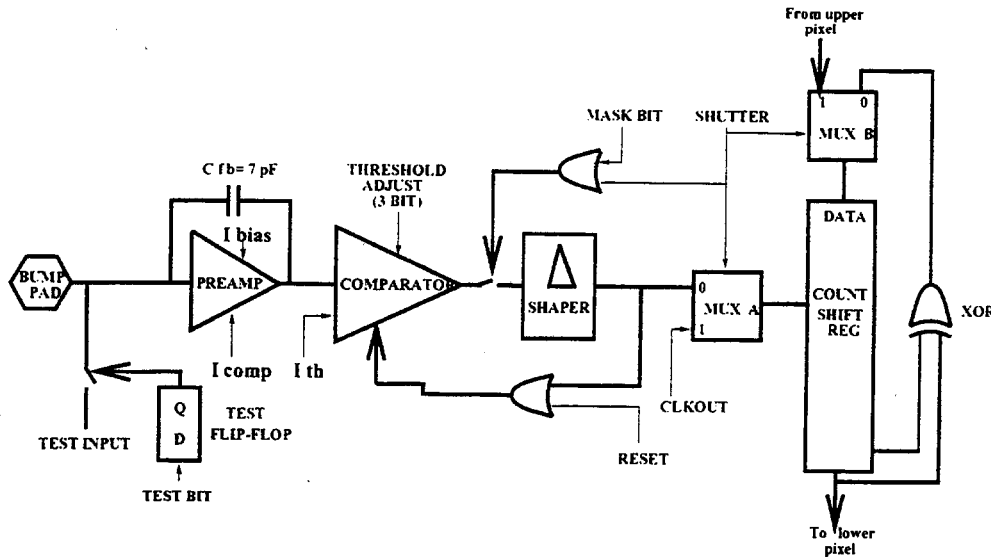


Figure 3: *MEDIPIX: chip electric scheme.*

maximum acquisition rate of 500 kHz, while its maximum read-out frequency is 10 MHz.

MRS (MEDIPIX Read-Out System) is the read-out system, designed and produced in collaboration with LABEN (Italy) to test and handle data from MEDIPIX. MRS is based on standard VME and consists of 3 boards: the VMEboard, the MOTHERboard and a custom CHIPboard.

The present CHIPboard hosts two chips and contains the circuits to transmit the analog currents MEDIPIX needs. The MOTHERboard is a stand-alone card without active elements but only containing the digital buffers for the differential signal transmission from VMEboard to chip. The VMEboard is a standard 6U single slot VME card divided into two parts; the analog one with the DACs generating the analog biases and the power supplies for MEDIPIX, and the digital one containing all the system logic controls and organized in four FPGA (Master, Decoder, Mask-Data and Counter-Data).

MRS allows four operation phases:

1. SETUP phase. This includes the mask loading, the setting of the analog biases and power supplies to the chip, the counters reset.
2. ACQUISITION phase. MEDIPIX acquires data from the detector.
3. TEST phase. MEDIPIX acquires data from a pulse generator interfaced to the system.
4. READOUT phase. The system stops acquisition and reads the chip counters.

The software to control MRS (Medisoft) has been written in C on a OS9 environment. It has a menu structure which allows the operator to select and execute the different routines in the four operation phases and to implement new functions which prove useful during the test of the system, without changing the main architecture of the software itself.

## 4 Electric threshold calibration of MEDIPIX

A set of MEDIPIX chips on a wafer have been electrically tested, before being bump-bonded to the detector.

After checking the digital part of each chip (writing and reading-out masks on the counters), the correct working values of the analog biases have been searched and then the pixels thresholds in each MEDIPIX have been calibrated sending pulses from a generator to the test input (1 mV pulse corresponds to about 100 electrons charge on the test capacitance of 16 fF).

The threshold should be set as low as possible because the goal is to detect signals of about 4000 electrons i.e. the charge collected by a 90% efficient GaAs detector every time a 20 keV photon is stopped in the crystal; a 5 standard deviations cut means to have a threshold of  $2500 e^-$  with a noise of  $300 e^-$ . So the first operation is to set a common (to all 4096 pixels) threshold low enough to avoid wrong counts induced by electronic noise (fig. 4).

Then the fine threshold adjustment has been performed setting the 3-bit mask so to narrow the distribution (fig. 5). In this way the final result is an average threshold in the most performing chips of 1400 electrons, with a 80 electrons spread on the 4096 pixels, better than the initial requirements.

## 5 Conclusions

Test on the "brick" obtained by the bump-bonding of the GaAs pixel detector to MEDIPIX will start in the next months and will consist first of the threshold calibration of each pixel using radioactive sources, and then of the production of phantoms images, such as it has been done with the 36-channels prototype. At the same time Montecarlo simulations are being run in order to evaluate (in terms of low dose, minimum image faking and costs) the best detector's scanning configurations, when more "bricks" will be assembled to form a sensitive area of mammographic interest (typically  $18 \times 24 \text{ cm}^2$ ).

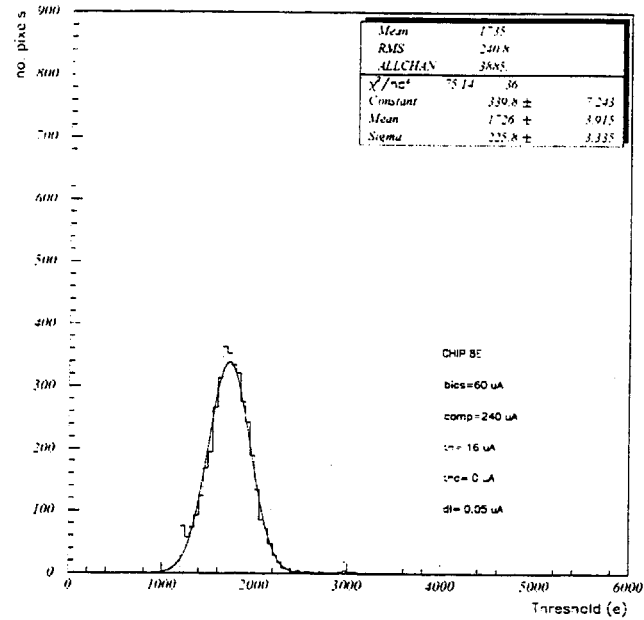


Figure 4: Distribution of thresholds for the MEDIPIX named 8E (from the position on the wafer) with the common setting of threshold current.

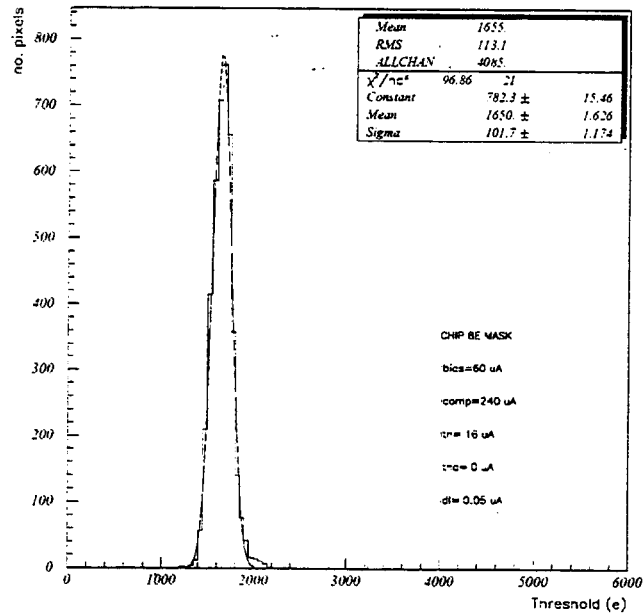


Figure 5: Distribution of thresholds for the MEDIPIX 8E after the threshold currents adjustment in each single pixel.

## References

- [1] *R.M.Harrison* "Digital Radiography", in **Phys.Med.Biol.**, 33, 1988(751).
- [2] *S.A.Feig et al.* "Digital mammography, computer-aided diagnosis, and telenmammography", in **RCNA**, 33, 1995(1205).
- [3] *S.McGregor et al.* "Evidence for field enhanced electron capture by EL2 centers in semi-insulating GaAs and the effect on GaAs radiation detectors", in **J.Appl.Phys.**, 75, 1994(12).
- [4] *S.P.Beaumont et al.* "Charge transport properties of undoped SI-LEC GaAs solid-state detectors", in **NIM A**, 326, 1993(313).
- [5] *A.Cola et al.* "A study of the electrical and charge-collection properties of semi-insulating GaAs detectors", in **NIM A**, 380, 1996(66).
- [6] *A.Cola et al.* "Field assisted capture of electrons in semi-insulating GaAs", in **J.Appl.Phys.**, 81, 1997(997).
- [7] *E.Pernigotti* "Comparison between integrating readout systems and single photon counting systems for digital mammography", in **Phys. Med.** 1998(to be published).
- [8] *S.R.Amendolia et al.* "Charge collection properties of SI-GaAs detectors equipped with new ohmic contacts" in **NIM A** 1998 (to be published).
- [9] *S.R.Amendolia et al.* "Experimental study of LEC GaAs detectors for X-ray digital radiography", in **NIM A**, 380, 1996(410).
- [10] *S.R.Amendolia et al.* "Imaging Performance of a GaAs Pixel Detector", in **Nuovo Cimento** 1998 (to be published).
- [11] *M.Campbell et al.* "Development of a pixel readout chip compatible with large area coverage", in **NIM A**, 342, 1994(52).
- [12] *E.H.M.Heijne et al.* "A semiconductor pixel detector readout chip with internal, tunable delay providing a binary pattern of selected events", in **NIM A** 1996(to be published).

## A 5 Million Frame per Second Radiography System Using High Energy Protons

The author list, which is fairly long is:

H.-J. Ziock, K. J. Adams, K. R. Alrick, J. F. Amann, J. G. Boissevain, M. L. Crow, S. B. Cushing, J. C. Eddleman, C. J. Espinoza, T. T. Fife, R. A. Gallegos, J. Gomez, T. J. Gorman, N. T. Gray, G. E. Hogan, V. H. Holmes, S. A. Jaramillo, N. S. P. King, J. N. Knudson, R. K. London, R. P. Lopez, J. B. McClelland, F. E. Merrill, K. B. Morley, C. L. Morris, C. T. Mottershead, K. L. Mueller, Jr., F. A. Neri, D. M. Numkena, P. D. Pazuchanics, C. Pillai, R. E. Prael, C. M. Riedel, J. S. Sarracino, H. L. Stacy, B. E. Takala, H. A. Thiessen, H. E. Tucker, P. L. Walstrom, G. J. Yates, J. D. Zumbro  
(Los Alamos National Laboratory, Los Alamos, NM 87545)

E. Ables, M. E. Aufderheide, P. D. Barnes Jr., R. M. Bionta, D. H. Fujino, E. P. Hartouni, H.-S. Park, R. Soltz, D. M. Wright  
(Lawrence Livermore National Laboratory, Livermore, CA 94550)

M. Amman, JF. Beche, E. Beuville, V. Douence, L. Fabris, F. Goulding, N. Madden, J. Millaud, B. Turko, J. Walton, J. Zaninovich  
(Lawrence Berkeley National Laboratory, Berkeley, CA 94720)

S. Balzer, P. A. Flores, R. T. Thompson  
(Bechtel, Nevada, Los Alamos Operations, Los Alamos, NM 87545)

R. Prigl, J. Scaduto, E. T. Schwaner  
(Brookhaven National Laboratory, Upton, NY 11973)

A. Saunders  
(University of Colorado, Boulder, CO 80309)

J. M. O'Donnell  
(University of Minnesota, Minneapolis, MN 55455; current address: Los Alamos National Lab)

### Abstract:

We have developed a technique for taking multiframe radiographic images of dynamic objects up to hundreds of g/cm<sup>2</sup> thick using high energy protons as the probing particles. The technique is capable of simultaneously determining the amount, location, and types of material present in the object. The basic principles of the technique will be presented as will be radiographs taken using 10 GeV protons at the Brookhaven AGS, and 800 MeV protons at the Los Alamos LANSCE facility. Finally detector system concepts for this application will be presented.

The work presented in the poster session is covered in detail in two papers which are to appear in Nuclear Instruments and Methods as part of the proceedings of the 3rd International Symposium on Development and Application of Semiconductor Tracking Detectors, Melbourne, Australia, December 9-12, 1997. The preprints of those papers, LA-UR-98-1015 and LA-UR-98-1368, are included herein.

The work presented in the poster session is covered in detail in two papers which are to appear in Nuclear Instruments and Methods as part of the proceedings of the 3rd International Symposium on Development and Application of Semiconductor Tracking Detectors, Melbourne, Australia, December 9-12, 1997. The preprints of those papers, LA-UR-98-1015 and LA-UR-98-1368, are included herein.

## DETECTOR DEVELOPMENT FOR DYNAMIC PROTON RADIOGRAPHY

H.-J. Ziock, K. R. Alrick, R. A. Gallegos, J. Galyardt, N. T. Gray, G. E. Hogan, V. H. Holmes, S. A. Jaramillo, N. S. P. King, T. E. McDonald, Jr., K. B. Morley, C. L. Morris, D. M. Numkena, P. D. Pazuchanics, C. M. Riedel, J. S. Sarracino, G. J. Yates, J. D. Zumbro  
[Los Alamos National Laboratory (LANL)]

M. Amman, JF. Beche, E. Beuville, V. Douence, L. Fabris, F. Goulding, N. Madden, J. Millaud, B. Turko, J. Walton, J. Zaninovich  
[Lawrence Berkeley National Laboratory (LBNL)]

### ABSTRACT

The development of high frame rate imaging charged particle detector systems for proton radiography at an advanced hydrotest facility (AHF) is discussed. The detector systems being developed are to be capable of providing a movie of dynamic events with inter-frame times as short as 200 nanoseconds and with spatial resolutions of 1/2 mm or better. Initial results from beam tests of a 1024 frame  $8^2$  pixel silicon detector prototype device and a four frame 1024<sup>2</sup> pixel electro-optically shuttered camera system will be presented.

### INTRODUCTION

A promising new technology, proton radiography, for performing dynamic radiography on thick objects (100's of gm/cm<sup>2</sup>) is being developed as part of the US Science Based Stockpile Stewardship program. The general concept of proton radiography (PRAD) is addressed in a separate paper in these proceedings<sup>1</sup>. In this paper we discuss the detector systems being developed for the PRAD project. The detector performance that we hope to achieve is given in Table 1. The detector development effort is broken into two separate parts. The first is aimed at providing limited multi-frame capability in a short time scale for rapid experimental verification of the PRAD concept. The second is longer term and addresses the full set of requirements given in Table 1, and if possible maintains a flexible design, capable of expanding to go beyond those requirements as they are likely to be a moving target. Before proceeding to the details of the detector development effort, we briefly review the basic detector options and their limitations.

Protons, being charged particles, themselves interact with the detector medium leaving an ionization trail that can be detected directly or indirectly. In ionization detectors, gaseous or solid state, the positively charged ions and negatively charged ions or electrons of the ionization track are separated and collected to form the signal directly. For silicon detectors it takes 3.6 eV of energy loss by the incident particle to generate one electron-hole (eh) charge pair on the average, although the fundamental energy loss mechanism for charged particles involve  $\sim 17$  eV quanta<sup>2</sup>. The specific ionization energy loss for a minimum ionizing particle (MIP) in silicon results in an average of about 80 eh pairs per  $\mu\text{m}$ . The other means of signal generation is indirect, such as in a scintillator where the ionization is turned into light, which is collected and turned back into a second electric signal by, for instance, a photocathode or a photodiode. This entire process is rather inefficient, requiring on the order of 100 eV of energy loss in plastic scintillator to produce a photon which is difficult to collect and turn back into an electrical signal. The specific ionization in the plastic scintillator we used resulted in about 17,000 photons emitted into  $4\pi$  steradians per cm of plastic scintillator for a MIP. Mirroring the back surface of the scintillator is at best only about 80% efficient so one can only achieve about 15,000 forward (into  $2\pi$  steradians) photons.

### LIGHT COLLECTION

Schematically a light based detector system for PRAD will resemble what is shown in Fig. 1. Light is generated in a scintillator, which is located in the image plane of the PRAD magnetic lens<sup>3</sup>, reflected by

Table 1: Detector Performance Goals

Frames to be read out	$\sim 100$ or more
Time spacing of frames	$\sim 200$ nsec
Duration of frame (strobed)	$\sim 10$ nsec
Spatial resolution at object	$\sim 1/4$ mm pixel
Region to be imaged	$\sim 10$ cm
Mass density accuracy	$\sim 1\%$ or better
Particles detected / element	$\geq 25,000$
Maximum signal per pixel	$\sim 250\text{k}$ particles
Accuracy	$\sim 12$ bit

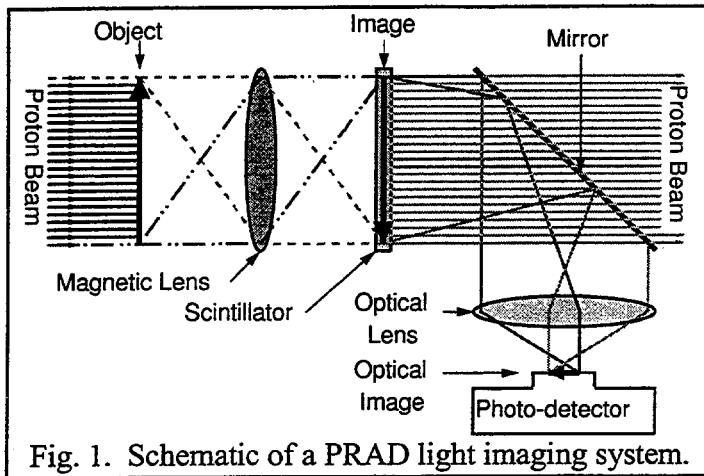


Fig. 1. Schematic of a PRAD light imaging system.

a 45° mirror out of the path of the proton beam, and then collected and imaged by an optical lens onto the photo-detector plane that creates the electrical signal. The above assumes that the photo-detector is itself sensitive to charged particles and must therefore be out of the proton beam. Although one could in principle use fiber optics to carry the light directly from the scintillator to the photo-detector, and thereby avoid the use of the mirror and lens, in practice this results in undesirable complications. First, the clear fiber array must have the same dimensions as the scintillator which according to Table 1 is on the order 10 cm on an edge if we assume that the magnetic lens is an identity lens.

In bending the fibers at 90° to the beam direction, in order to get them out of the beam requires a depth for the clear fiber array of at least 1/2 the scintillator edge dimension and in reality it will be somewhat larger, especially if a 90° kink can't be made and instead one needs a smooth bend. These clear fibers will introduce a substantial amount of undesirable material in the beam creating background problems. This would severely limit the feasibility of using multiple planes of detector. The second problem is that Cerenkov light will be generated in the clear fibers. This becomes a problem as the fibers are being diverted to exit the region of the beam. At that point, light will be generated in clear fibers which are not connected to the ones that the proton will strike in the scintillating fiber array, resulting in an additional background problem. The Cerenkov problem can be minimized as the Cerenkov light is emitted in a forward direction and is broadband. This would however require the complication of using narrow bandpass filters for the scintillation light and choosing the proper fiber geometry.

Instead of trying to cope with all the problems associated with a fiber readout, we decided to use the mirror-lens coupled solution which has its own, but much more straight forward problem, namely the small amount of light captured by a lens system. This is especially true when the lens is operated with a magnification which is less than unity as is required when the photo-detector such as a microchannel plate (MCP), proximity focus diode (PFD), or CCD is much smaller in size than the object being imaged.

An optical lens system is used to form an image of the downstream face of the scintillating fiber array on the light detection device. The lens also serves the purpose of demagnifying the object to a size such that the image fits onto the detector. A lens does this rather inefficiently, capturing only a very small fraction of the light generated. The fraction of the light emitted in a forward direction (into  $2\pi$ ) that is captured by a lens which accepts a cone of half opening angle  $\theta$  is simply

$$\text{fraction} = 1 - \cos(\theta). \quad (1)$$

Using various relationships for optics, the half cone acceptance angle for a lens system can be rewritten as

$$\theta = \text{atan}\{1/[2F(1 + 1/M)]\} \quad (2)$$

where  $F$  is the f-number ( $F\#$ ) of the lens ( $=$  focal length / effective diameter) and  $M$  is the magnification (typically less than unity in our application). Thus the fraction of forward light ( $0^\circ$  to  $\pm 90^\circ$ ) accepted by a lens system from a point source is

$$\text{fraction} = 1 - \cos\{\text{atan}[M/(2F(1 + M))]\} \quad (3)$$

The angle  $\theta$  is still not the half cone angle into which light is emitted by the scintillator, as the light is refracted to larger angles on leaving the high index scintillator into the air. The emission angle in the scintillator  $\theta'$ , which the lens accepts is thus considerably smaller than the already small acceptance half cone angle of the lens by an amount

$$\theta' = \text{asin}\{\sin(\theta)/n\}, \text{ where } n \text{ is the index of refraction of the fiber core (we take } n = 1 \text{ for air).} \quad (4)$$

Putting this all together, one finds:

$$\text{fraction} = 1 - \cos\{\text{asin}[\sin(\text{atan}\{1/[2F(1 + 1/M)]\})/n]\} \approx (M^2) / [8n^2F^2(1 + M)^2], \quad (5)$$



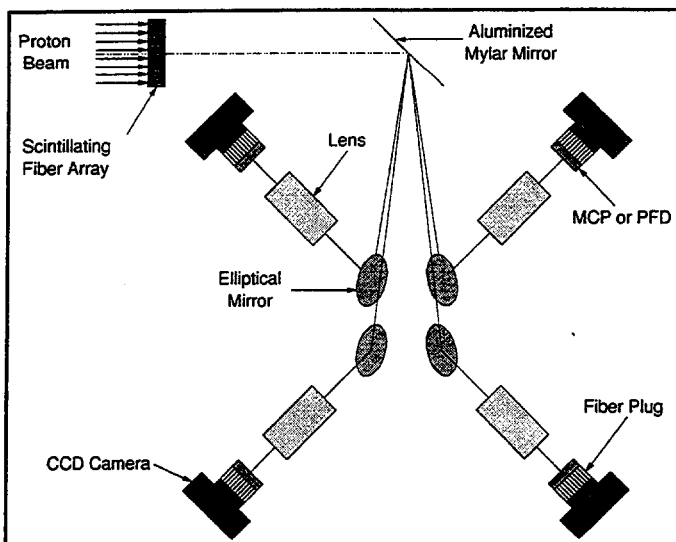


Fig. 2. Schematic of the 4-frame detector system. The cameras and lenses were in a common horizontal plane which was below the proton beam.

where the last result makes use of the small angle approximation for the trigonometric functions. Putting in values representative of those we used ( $M = 1/5$ ,  $F = 1.8$ ,  $n = 1.6$ ) gives  $fract = 4 \times 10^{-4}$ . This value is then further reduced by a number of other factors. These include a packing fraction associated with the active part of the scintillating fiber array (typically  $< 70\%$ ) and the light transmission of the optical system which is  $< 90\%$ , especially for the blue light emitted by the scintillator. The largest factor is however the quantum efficiency of the light detector which is on the order of 20% for a photocathode and 35% for a CCD. When all the inefficiency factors are taken together, they reduce the overall efficiency of the system another factor of about 10. Taking the total number of forward photons, which in the case of a 2 cm scintillator for MIPs is 30,000 and multiplying by the lens acceptance and other inefficiencies results in about one detected photoelectron per proton and thus very poor counting statistics.

### SHORT-TERM SOLUTION

In order to allow us to address a number of issues concerning multi-frame dynamic radiography we developed a limited frame camera system capable of recording images separated by  $1 \mu s$  or less. Due to the limited development time available, we used off-the-shelf hardware. Our initial attempt involved the use of an IMCO ULTRANAC<sup>4</sup> framing camera. A framing camera consists of a photocathode from which the emitted electrons are accelerated and electrostatically focused to form an image on a downstream, long decay time phosphor screen. Horizontal and vertical electrostatic deflection plates between the photocathode and phosphor screen are used to move subsequent images to fresh locations on the phosphor screen. After some initial tests, this approach was discarded. We found the photocathodes in all our in-hand framing cameras (which were originally bought to be used in experiments dealing with the longer wavelength part of the visible spectrum) were nearly blind to the very blue light emitted by the standard plastic scintillators. Also the small diameter of the photocathode (18 mm diameter) required a reduced lens magnification resulting in even less light. We also had concerns about the potential for distortion in the image caused by space charge effects at the cross-over point of the electromagnetic lens in the framing camera. Stray magnetic fields from the proton imaging lens also distorted the framing camera image.

Our next attempt was based on a set of cooled slow scan CCD cameras, each coupled to a gated image intensifier for shuttering. The shuttering of the different cameras was time phased so that each camera recorded a different time ( $\sim 40$  ns burst of protons). The schematic of the camera system adopted is shown in Fig. 2. It should be noted that in this configuration each camera looks at an independent part of the solid angle, thereby avoiding any beam-splitter induced loss of light. The electronic shuttering is based upon our earlier work<sup>3, 6</sup> in electro-optic shuttering of microchannel plate image intensifiers (MCPs) by gating their photocathode emission. For some of the cameras we opted for proximity focus diodes<sup>7</sup> (PFDs), which we gated by switching their bias voltage on and off<sup>8</sup>. The intensifiers also provided gain for these weak photon flux experiments and provided wavelength shifting between input and output images for optimal spectral matching to the CCD. Because of the broad requirements for imaging camera system performance, such as wide dynamic range, variable gain, signal-to-noise, and tradeoffs between gain and resolution requirements, we decided to use both DEP<sup>9</sup> MCPs and Proxitronic PFD intensifiers, to exploit and evaluate the features of each type. The MCPs have higher gain and faster shuttering with lower high voltage and gate pulse amplitude requirements. The PFDs have higher QE, higher resolution and lower noise, but require much higher bias and gate potentials. Both have adequate dynamic range to

effectively use the CCD pixel well capacity. We are still evaluating tradeoffs between the two intensifier types<sup>10</sup>. Results of a dynamic shot using this camera system are shown in Fig. 3, which shows the propagation of a detonation wave in a 28.5 mm radius piece of high explosive (HE).

### LONG-TERM SOLUTION

For an AHF class detector system we took an approach which was modular in design and allowed for an evolving set of performance requirements. To demonstrate the basic concept we built a pair of  $8 \times 8$  pixel detector systems designed to meet or exceed all the performance requirements given in Table 1, with the exception of pixel size. Our pixel sizes were  $(1 \text{ mm})^2$  and  $(0.5 \text{ mm})^2$ . There is no problem with building

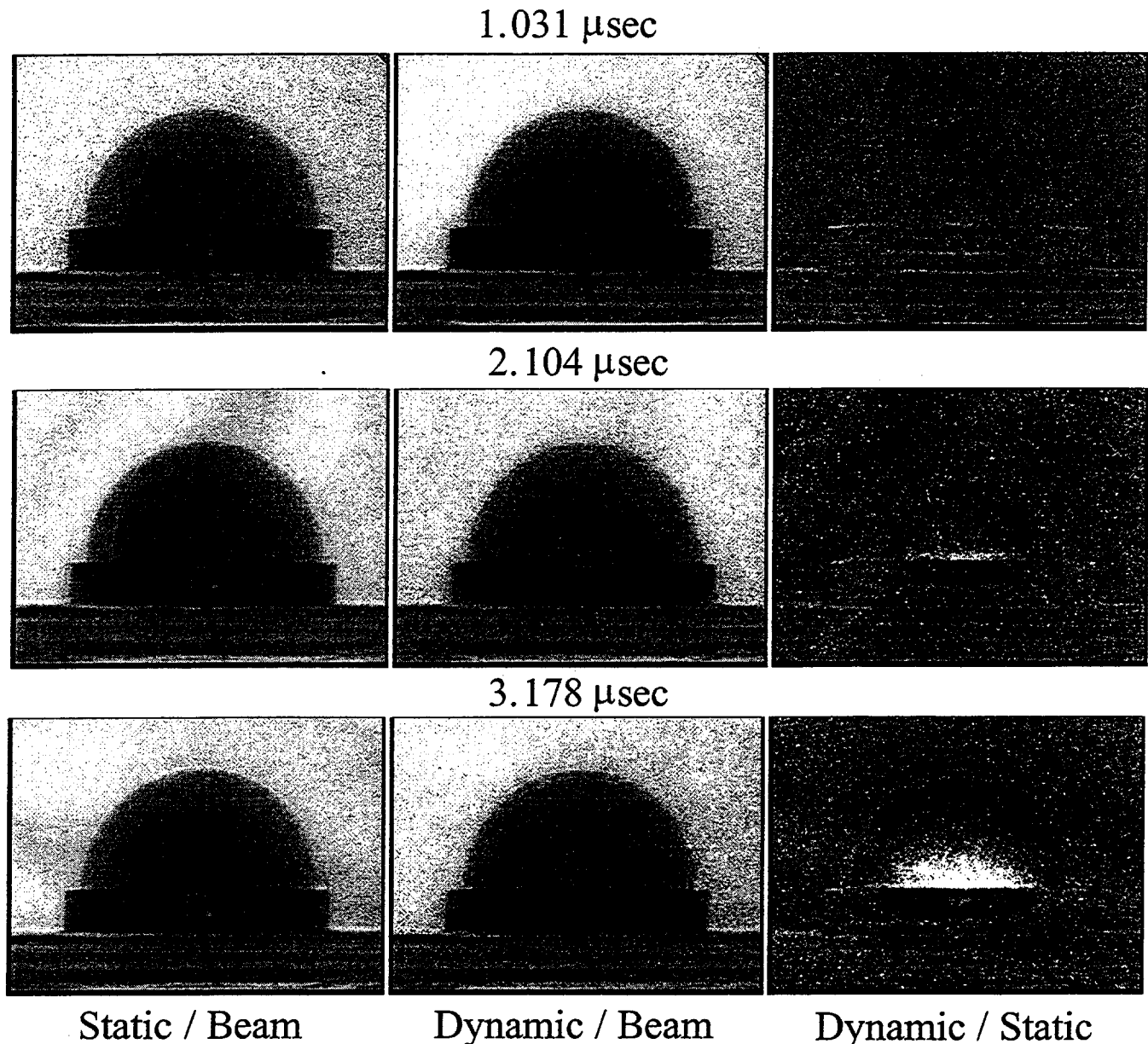


Fig. 3. Ratio images of proton radiographs taken by the detector system. Each row corresponds to a different camera. The fourth camera was unfortunately disabled by a lightning strike shortly before these radiographs were taken. The three different columns correspond to beam normalized radiographs of the static object (left column), beam normalized radiographs of the object as it was exploding (center column), and ratios of the dynamic to static images (right column), which emphasize differences between the static and dynamic radiographs. The given times are relative to detonator breakout.

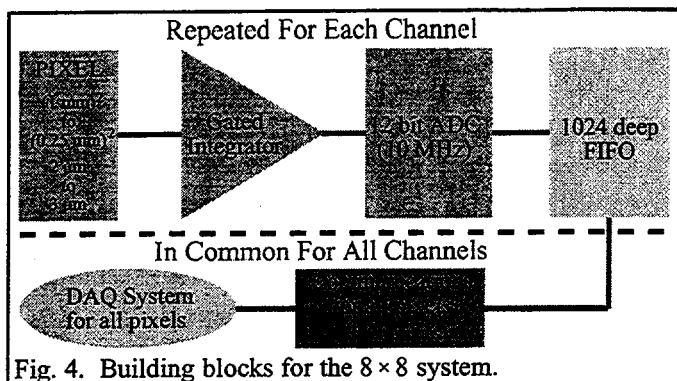


Fig. 4. Building blocks for the  $8 \times 8$  system.

smaller pixel sizes. The problem is instead in the high density interconnections which we were not prepared to address at this stage of the effort. The resulting small prototype was largely designed and constructed by LBNL.

The building blocks of the  $8 \times 8$  system are shown in Fig. 4. For every pixel we had an individual low gain gated integrator, followed by a 10 MHz 12-bit pipelined ADC ( Analog Devices AD9220), followed by a 1024 deep first in first out (FIFO) memory unit. In common to these 64 channels of electronics was a control card. This provided the proper phasing of the clock signal which was derived from the accelerator RF system, the trigger signal that started the data storage in the FIFO's and the readout circuitry that read back the 1024 readings from each of the 64 FIFO's. Each reading was then sent via a fiber optic link to the data acquisition computer on command via a CAMAC card once the exposure set was complete. The entire system was built using discrete off-the-shelf components. The hardware configuration is shown in more detail in Fig. 5 and was centered around a Motherboard into which we could plug different samples of the  $8 \times 8$  detector. Into the Motherboard we also plugged 8 pairs of cards, each card pair servicing 8 pixels. The card pairs consisted of the gated integrator / driver card which in turn fed the ADC-FIFO card. The 9th card that plugged into the Motherboard was the control card mention above. A schematic of the gated integrator is shown in Fig. 6.

The silicon *pin* detectors themselves were of a very special design which made use of epitaxial processing by Lawrence Semiconductors<sup>11</sup>. The detectors were made effectively very thin because we were concerned about the potential for collapse of the detector bias field and the very large current spikes that might have otherwise occurred when on the order of 100,000 protons hit each and every pixel every proton burst. The detectors consisted of a 500  $\mu\text{m}$  thick very heavily *n*-doped silicon substrate (few  $\times 10^{19}$  dopant atoms/cc), on top of which a 2 or 3  $\mu\text{m}$  thick epitaxial layer of more lightly doped *n*-type material ( $\sim 10^{15}$  dopant atoms/cc) was grown, and which during operation formed the active (*i*-type) part of the detector. Doping profiles of two of the wafers are shown in Fig. 7. Ion implanted *p*-type regions were

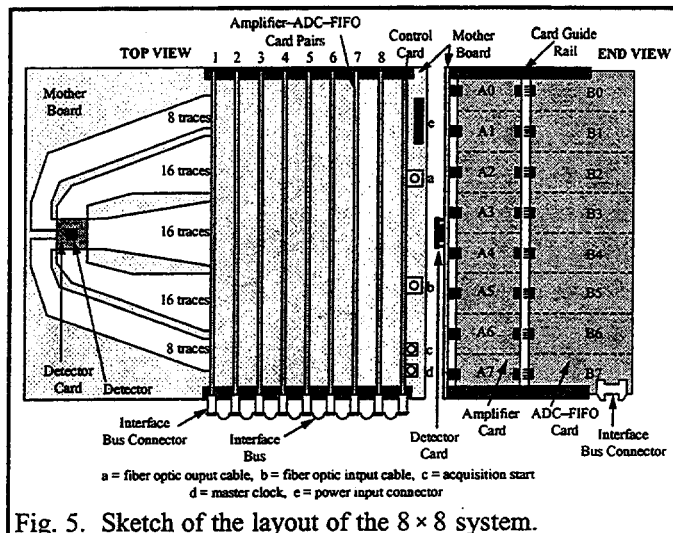


Fig. 5. Sketch of the layout of the  $8 \times 8$  system.

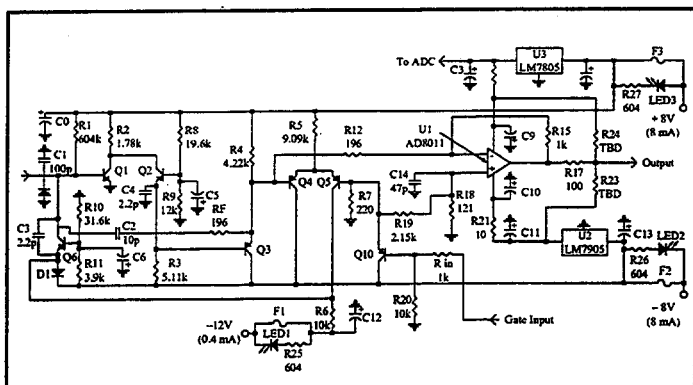


Fig. 6. Schematic of the gated integrator. The charge gain for the amplifier is about a factor of 5.

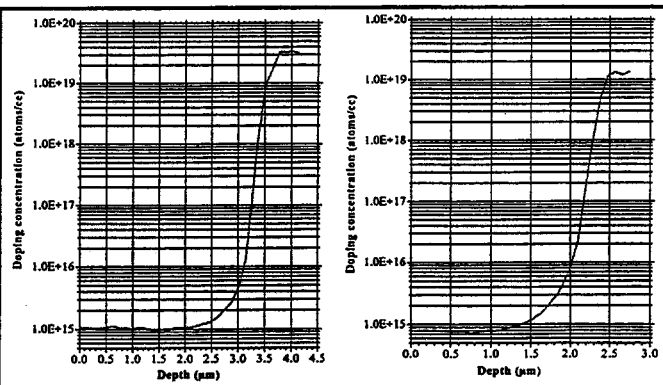


Fig. 7. Doping profiles for one of the 3  $\mu\text{m}$  and one of the 2  $\mu\text{m}$  epitaxial detector wafers.

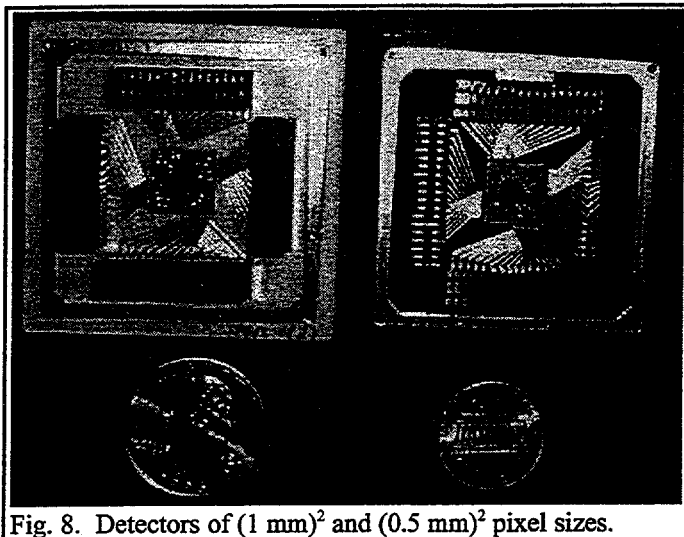


Fig. 8. Detectors of  $(1\text{ mm})^2$  and  $(0.5\text{ mm})^2$  pixel sizes.

then used to make the individual pixels. These were in turn sputtered with aluminum contacts to which the wire bonds were made. The detectors were glued to small ceramic cards (Fig. 8) which had connectors along their periphery to allow them to be plugged into the Motherboard. Despite the thinness of the active detector layer, substantial signals (160 to 240 eh pair on average) were generated for each proton, which is to be compared to the single photoelectron per proton from the scintillator based system discussed earlier. The detectors were biased at a few volts, with the bias being applied to the substrate side. The pixels side was connected to the electronics, which was designed to offer a very low input impedance up to very high frequencies. (Subsequent measurements showed that the epitaxial (active) layer of the detectors was fully depleted by the internal junction voltage.)

Leakage currents across the detector wafers varied. Occasional pixels showed leakage currents in the  $10\text{ }\mu\text{A}$  range. However, sub-nanoamp values were far more common and a number of  $8 \times 8$  pixel regions were found on the wafers in which all the pixels had sub-nanoamp leakage current values. For comparison, the proton beam induced signal currents in the pixels were in the 10 to  $100\text{ }\mu\text{A}$  range.

The performance of the detectors and readout electronics is shown in Figs. 9 to 14. Fig. 9 shows the performance during a bench test of the electronics chain when it was clocked at 5 MHz with a DC voltage level through a resistor providing the injected input charge. The rms deviation is  $\sim 2$  ADC counts, ( $4095 =$  full scale). A similar noise level was seen with the system in the experimental area and reading out a detector just before or after beam bursts arrived. Fig. 10 shows the linearity of the system response averaged over all 64 pixels as a function of proton beam intensity. The horizontal axis gives the proton beam intensity as measured by a toroidal pickup coil (arbitrary scale units with an obvious zero offset) and the vertical axis gives the 64 pixel average ADC value. The spread in the points is largely due to noise in the pickup coil circuit. Fig. 11 shows the time response of the system. The 800 MeV proton beam at the Los Alamos Neutron Scattering Center (LANSCE) for our tests was run in a chopped mode with a frequency of  $1/72$  of the fundamental accelerator frequency of 201.25 MHz resulting in a chopped beam burst once every  $\sim 358\text{ ns}$ . The 358 ns mode could be further gated to give a proton burst once every  $N \times 358\text{ ns}$  ( $N = \text{integer}$ ). For Fig. 11, two detector response curves are shown, one with  $N=2$  and the other with  $N=10$ . The detector system itself took readings once every 358 nsec. As can be seen, the detector responded fully to the beam time structure. Fig. 12 shows a picture of a vertical resolution pattern taken with a  $(0.5\text{ mm})^2$  pixel detector. The object imaged consisted of  $1/2\text{ mm}$  wide slots with a pitch of  $1\text{ mm}$  cut into a heavy metal plate. The resolution pattern was placed in the object plane of the magnetic lens system of our radiography setup<sup>1</sup>. The detector plane coincided with the image plane of the magnetic lens and immediately downstream of it we placed a phosphor image plate. The relative alignment of the detector and resolution pattern can be seen in the image plate picture (the left half of Fig. 12). The central

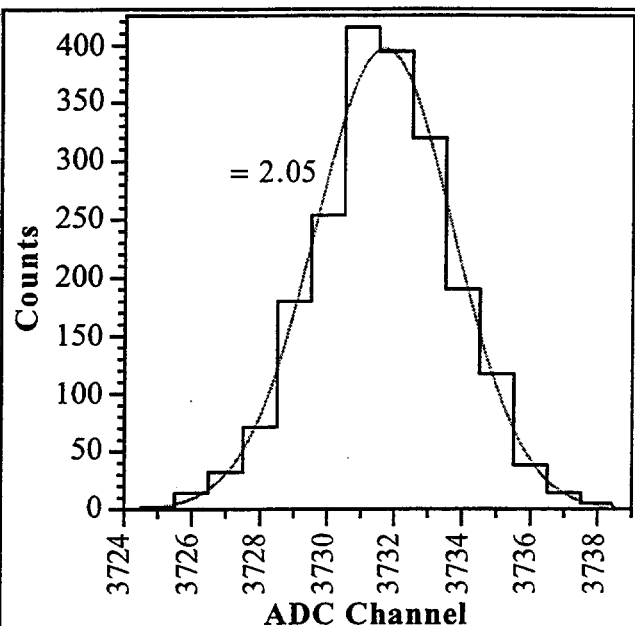


Fig. 9. System performance at 5 MHz with DC input.

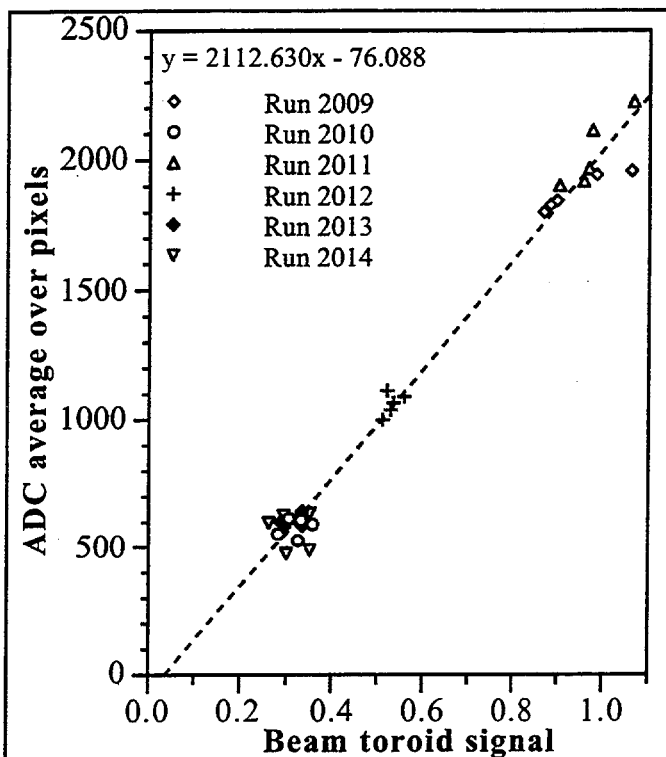


Fig. 10. Detector response as a function of beam intensity.

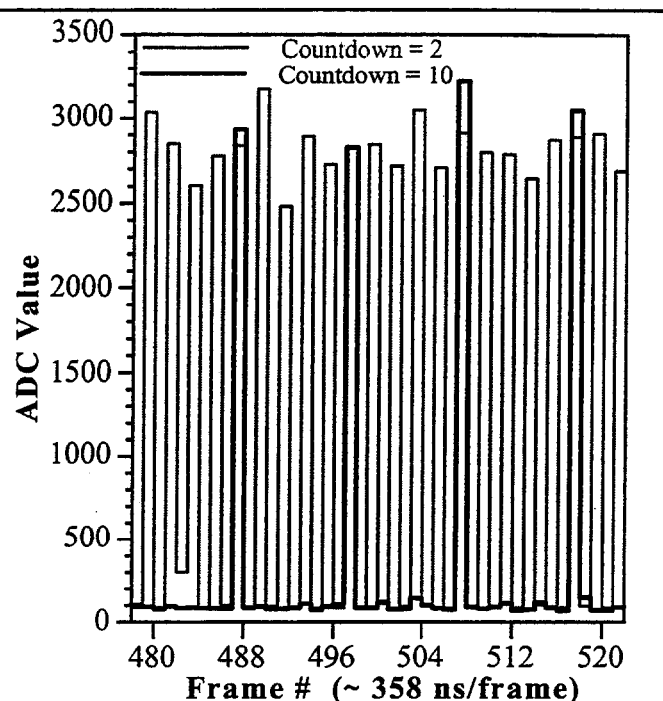


Fig. 11 Time response of the detector system for a beam burst every  $2 \times 358$  ns and for a burst every  $10 \times 358$  ns. The inter-frame time was 358 ns.

square subsequently superimposed on the image is the location of the detector proper as determined from the pin locations of the connectors of the detector card. The pins can be seen along all 4 edges of the image plate picture. The right hand image is a plot of the ADC values from the 64 pixels of the silicon detector and very clearly shows the resolution pattern.

Finally, Figs. 13 and 14 show the results of a dynamic experiment. The image plate inset in Fig. 13 shows a picture of a short cylindrical piece of HE seen from its side. A steel plate (the dark area) was glued to the top of the HE. At the bottom of the HE, the detonator is visible. The location of the silicon detector can be ascertained from the pins of the chip carrier. The silicon detector systems overlapped the HE with 6 or 7 rows of pixels, and overlapped the steel with two or one rows of pixels respectively. For this test both of our  $8 \times 8$  detector systems were used, with about a 1 cm gap between them. Fig. 14 shows the output of the two systems (S1-S8 = system 1, S10-S18 = system 2). The two systems were misaligned by about one row as is evident when comparing the low numbered row regions (1-3).

Both systems had  $(1 \text{ mm})^2$  pixel detectors. For system 1, all 64 pixels were operating, whereas system 2, had four bad pixels. Fig. 13 shows the response of both of the two systems averaged over all good pixels and plotted on an arbitrarily normalized scale. The beam toroid signal is shown as the gray step function shaped curve. Also shown is the response of detector system 1 but with the individual frames normalized by the beam toroid values. The beam toroid signal shows that the beam was turned on at frame 37. A proton burst arrived once every 358 ns, the same as the frame spacing for the pixel systems. The HE was initiated at the time indicated by the vertical line at frame 146. Several  $\mu\text{s}$  after initiation, the detonation wave reached the region of the steel plate and began pushing it out of the field of view of the detector system. This is indicated by the steep rise in the transmitted proton beam intensity seen by the detectors. At the about same time the detonation wave broke out of the HE surfaces and the reaction products (gases) began to dissipate boosting the detector signal even more. The proton beam attenuation change due to the gas expansion is rapid at first but slows with time as the gas becomes more dilute. Nonetheless, even many hundreds of frames after the detonation, the expansion of the gas is still evident. The sudden dip starting at frame 447 is due to a 3 frame programmed interruption of the beam used to demonstrate proper operation of the system.

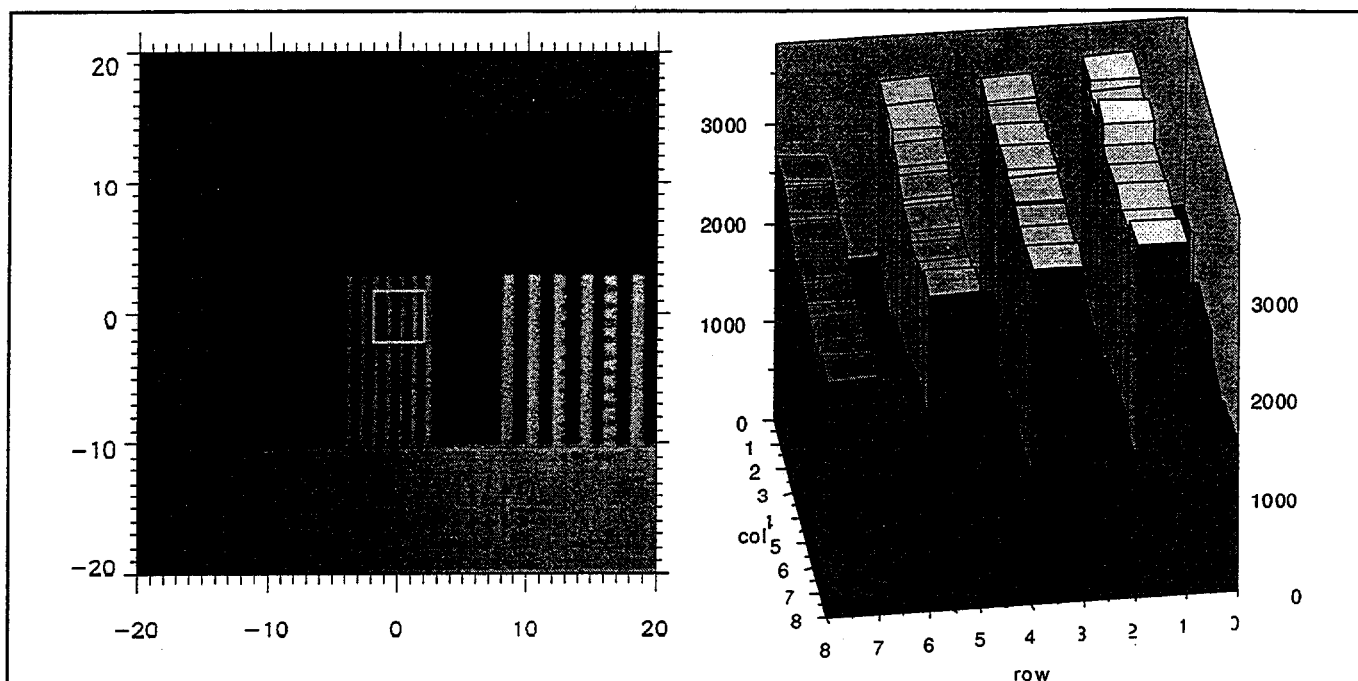


Fig. 12. The left image shows an image plate picture of a vertical resolution pattern. The scale is in mm. The two parallel rows of slightly darker small spots near all 4 edges of the image are the connector pins of the card holding the silicon detector. These were used to determine the detector location which is indicated by the small square near the center of the image. The right image shows the output of the  $8 \times 8$  pixels in units of ADC counts.

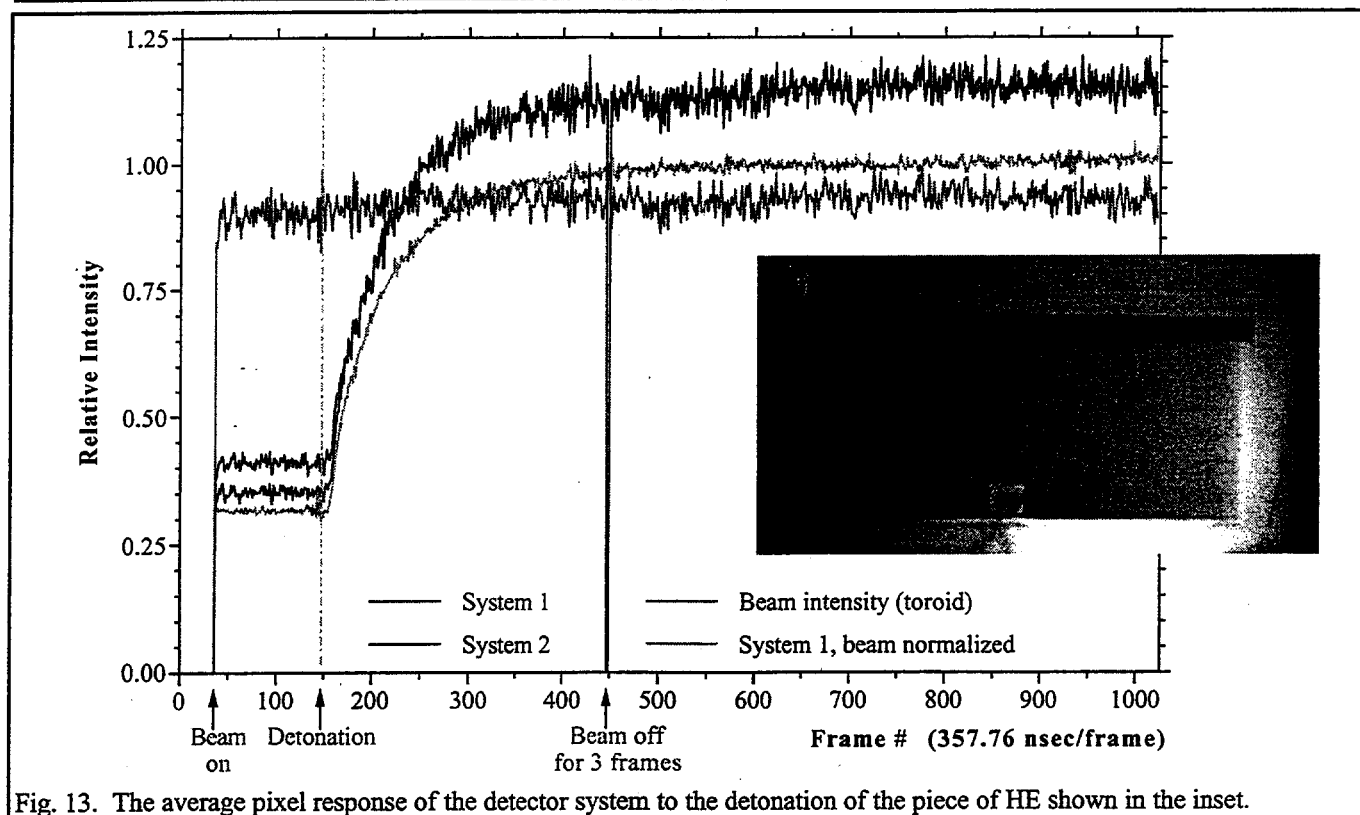


Fig. 13. The average pixel response of the detector system to the detonation of the piece of HE shown in the inset.

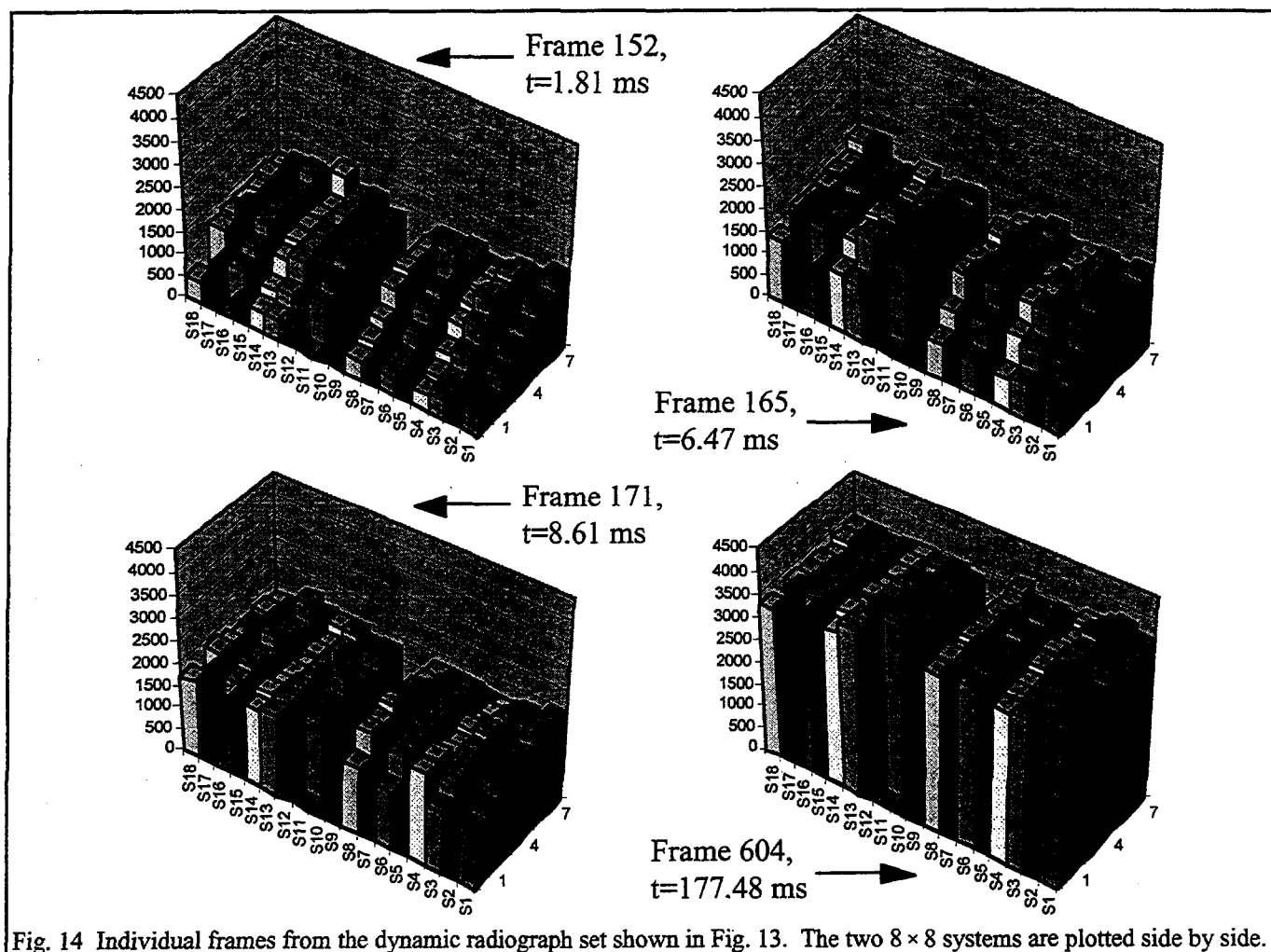


Fig. 14 Individual frames from the dynamic radiograph set shown in Fig. 13. The two  $8 \times 8$  systems are plotted side by side.

## PROBLEMS

Fig. 15 shows several sequential frames of pixel detector output of what should be a very uniform beam spot. Although this is what is seen on the average, also apparent are a number of relatively large and random fluctuations in pixel response. A systematic characterization of these fluctuations is shown in Fig. 16 in which is plotted a distribution of ratios of pixel values from a large number of frames and a large number of pixel pairs. (Frame to frame beam intensity changes, and different pixel gains were corrected for before the ratios were taken.) The rms width of the distribution is seen to be over 9%. Although there are relatively large fluctuations in energy deposition in thin detectors as given by the Landau distribution<sup>12</sup> or variants thereof<sup>13</sup> for single protons, when averaging over a large number,  $N$ , of protons per pixel, the pixel fluctuations should be a factor of  $N^{1/2}$  smaller than the individual proton fluctuations. As such even a 100% fluctuation level for single proton measurements should result in only a 0.58% fluctuation in pixel response and therefore cannot be the cause of the problem. Another explanation is in order as we had  $N \approx 30,000$  for the results shown in Fig. 15 & 16.

An alternative explanation lies in nuclear interactions of protons in the silicon pixels themselves. Starting with the inverse of the nuclear collision length in silicon of  $(70.6 \text{ g/cm}^2)^{-1}$ , multiplying by the density of silicon and an active detector thickness of  $2.0 \text{ } \mu\text{m}$ , and assuming 30,000 protons incident on a pixel in a single frame, gives a probability of 0.20 that a nuclear interaction will occur per pixel per frame. When this is folded with Poisson counting statistics, the probability of no nuclear interactions in a given pixel in a given frame is 82%, whereas 18% of the time one or more nuclear interactions take place. This is significant. One additional criterion must be satisfied for this to explain the observed effect, namely the



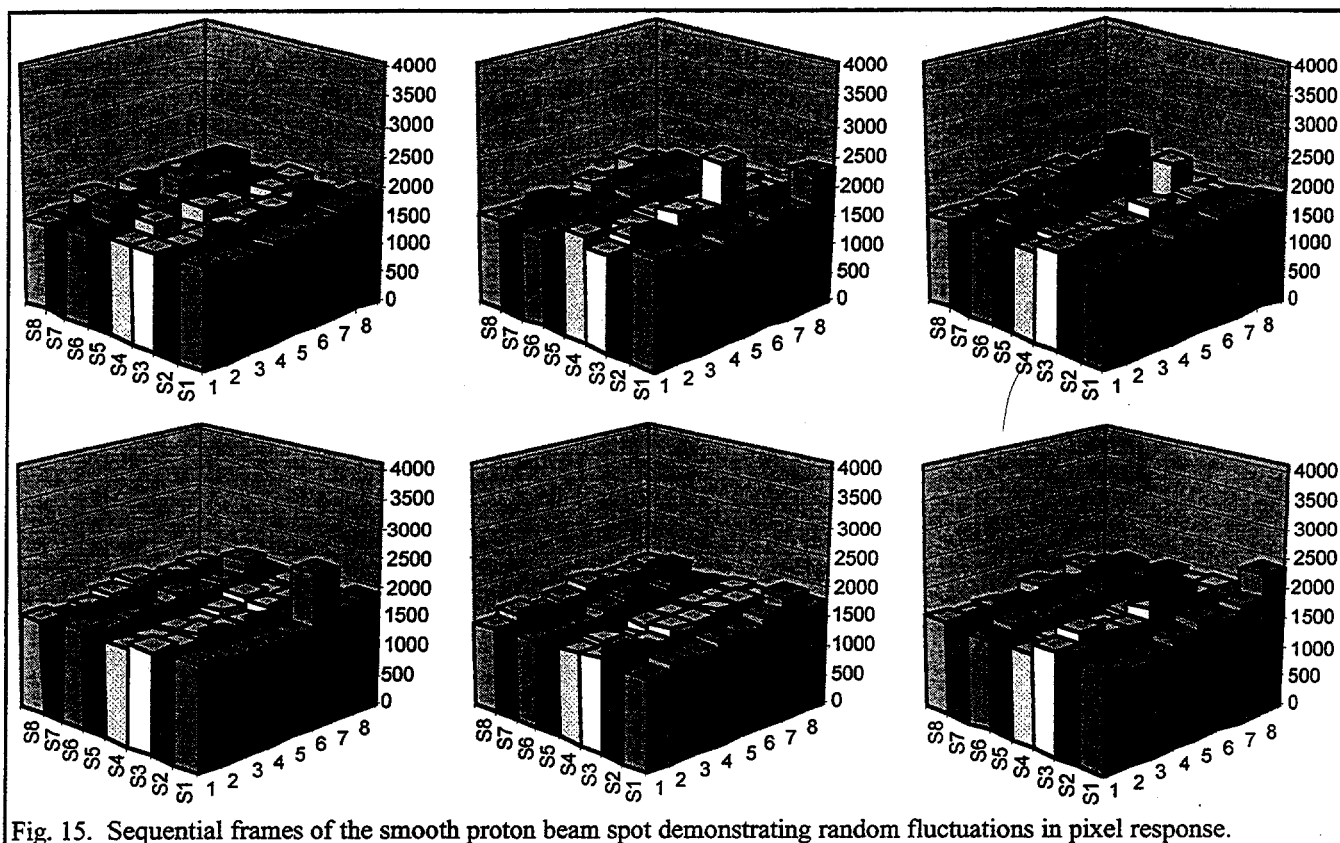


Fig. 15. Sequential frames of the smooth proton beam spot demonstrating random fluctuations in pixel response.

nuclear collision must result in a very large energy deposition in the active part of the detector. If instead the nuclear collision solely produced a single high energy secondary particle, that particle would look like any of the 30,000 incident protons and as such would result in a 1 in 30,000 part fluctuation in the signal, clearly not what is required. What is needed instead is a slow heavy recoiling particle which is capable of depositing a significant amount of its energy even in a very thin active layer. This could easily be done by a recoiling residual nuclear fragment. If we assume a knockout of a single nucleon from a silicon nucleus in which the Fermi level had a typical value (300 MeV/c), the recoiling nucleus would have an average momentum of 300 MeV/c. Translating that momentum into the kinetic energy of a mass 27 amu fragment, we find a value of 1.8 MeV, which would be easily be stopped by 2.0  $\mu\text{m}$  of silicon. Comparing this energy deposit with that of the 30,000 protons, which on average each deposit about 500 eV, or 15 MeV in total, we find that a single nuclear interaction can easily cause a 12 % fluctuation. This number is of the order of magnitude required to explain the phenomenon.

Several options are available to deal with this problem. A number of these are based on trying to reduce the detector thickness thereby decreasing the probability of a nuclear interaction. The limiting detector thickness value is probably around 1  $\mu\text{m}$ , which would decrease the effect

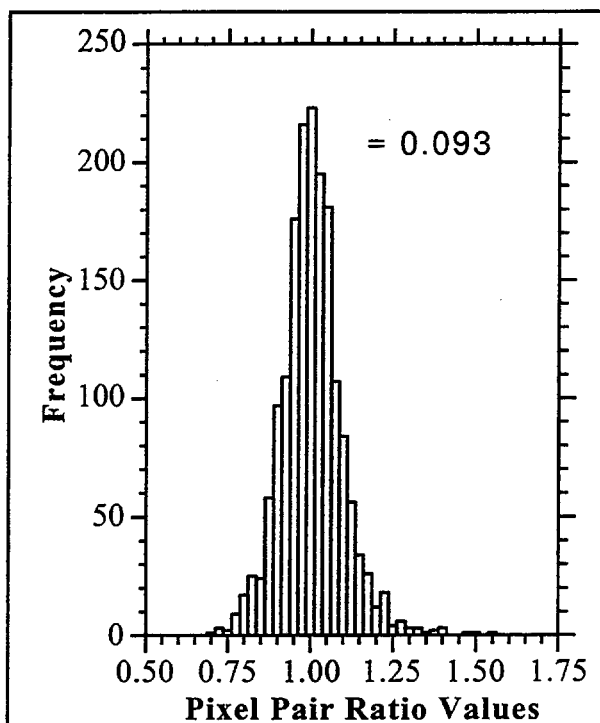


Fig. 16. Ratios of pairs of pixel values from a large number of frames and pixel pairs. Mean differences in pixel response and beam intensity were corrected for.



by a factor of two from that calculated above. Another approach is to subdivide each resolution element in the image to a large number of pixels. One then keeps the proton beam intensity per resolution element about the same. This decreases the number of protons per pixel by the number of pixels per resolution element. The probability of a nuclear interaction per pixel changes by the same amount. While this is occurring the fractional change in signal caused by a nuclear interaction in a pixel goes up by the number of pixels/resolution element, making those "bad" pixels even more readily apparent. Those pixels are then rejected, and only the "good" pixels in a resolution element are used. If desired, the loss in the counting statistics due to the few bad pixels in a resolution element can always be compensated for by increasing the beam intensity slightly. A variant of this scheme<sup>14</sup> subdivides things in time as opposed to space, for instance sending 10 bursts of protons separated by 20 ns, each of 1/10th the nominal intensity and each one being read out, as opposed to 1 nominal burst every 200 ns.

An alternative to the above approach of trying to decrease the probability of a nuclear interaction is to go in the opposite direction and thereby effectively averaging out the effect of the fluctuations. For instance, in plastic scintillator, the inverse of a nuclear collision length is  $1/(58.4 \text{ gm/cm}^2)$ . Multiplying this by the density of the material, a thickness of 2 cm, and assuming 30,000 protons incident per pixel, one finds on the average 1000 protons have nuclear interactions. Thus the statistical effect of the interactions are reduced by a factor of  $1000^{1/2}$  or about 32 over that of a single interaction. At the same time, the relative effect of a single nuclear interaction collision is greatly reduced. The normal energy deposition of a high energy proton in 2 cm of plastic scintillator is 4 MeV, about equal to the kinetic energy of a recoiling 11 amu fragment with a momentum of 300 MeV/c. The fact that this approach works can be seen by doing a pixel ratio analysis for some of the scintillator based images taken with CCD cameras discussed earlier. Such an analysis shows an rms width of just over 2%, and the majority (~80%) of that is due to the poor photon counting statistic per proton and lower number of protons per pixel.

### FUTURE PLANS

Planned upgrades for the short-term CCD based system include expanding it to an 8 frame capability, and using larger diameter PFD's (40 mm vs. 25 mm) in order to increase the magnification and thereby the amount of light available and hence improving the counting statistics of photoelectrons per proton. The larger diameter PFD's will also be operated at higher voltages and therefore increased gain to make up for the loss of light that will occur in the tapered fiber optic bundle which connects the PFD to the  $\sim (25 \text{ mm})^2$  CCD. For the long-term system several paths are being pursued. We have designed an application specific integrated circuit (ASIC) which is based on the CMOS process and has been implemented in a

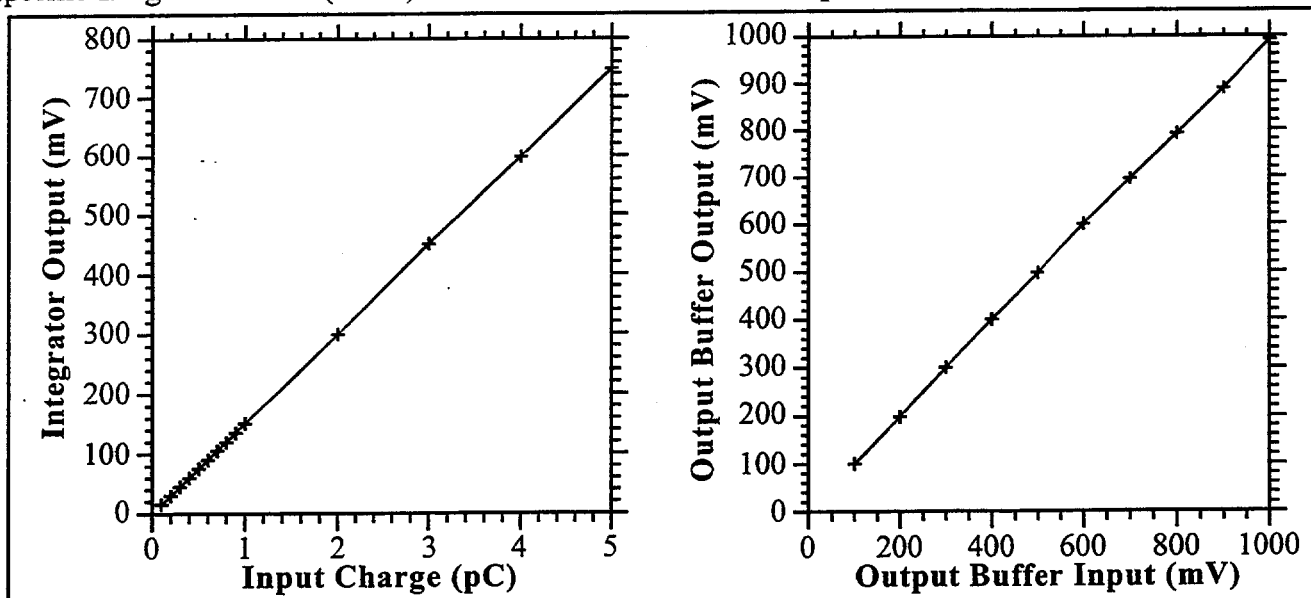


Fig. 17. Measured linearity of the response of the new ASIC chip components. The left plot is for the gated integrator and the right plot is for the output buffer circuit.

0.5  $\mu\text{m}$  HP MOSIS run. The chip has 4 gated integrators which multiplex their output to an included analog memory unit. The chip then sequentially feeds the 4 analog values via a driver circuit into a separate 12 bit 40 MHz pipelined ADC. Initial performance evaluations of the ASIC chip as shown in Fig. 17 look promising. The new ADC / ASIC chip combination are planned to form the basis of a new 10,000 pixel prototype system which will be used to look at system issues. In the longer term we still need to solve the interconnect problem for  $(1/4 \text{ mm})^2$  or smaller pixels.

We will evaluate several solutions to the apparent nuclear interaction problem. We have built some small photodiode arrays compatible with the LBNL electronics, which are presently being coupled to a fiber optic array. It should be pointed out that the electronics built by LBNL were designed to be fully compatible with the use of a photodiode detector as opposed to the solid state ionization detectors. Since silicon photodiode arrays can be built much larger and more cheaply than CCD detectors, it is possible to use a lens system with unit magnification as opposed to the magnification of 1/5 that was required for the CCDs. Referring back to eq. (5), this results in about a factor 9 more light. At the same time blue sensitive photodiodes have quantum efficiencies of at least 80%<sup>15</sup> buying us about a factor of 4 over the photo-cathodes on our MCPs or PFDs. Using the value of 1 photoelectron per proton derived earlier for our scintillator based system, we would now be about a factor of 36 better, or at just under 1/2 the signal that would be gotten from a 1  $\mu\text{m}$  thick silicon ionization detector.

Along the line of reducing the probability of nuclear collisions in a pixel in the time domain, we are considering building a version of the electronics which would use a single 40 MHz ADC to look at individual pixels once every 30 to 40 ns. We will also look at reducing the detector thickness to 1  $\mu\text{m}$ .

## CONCLUSIONS

We have constructed a 4 frame electro-optically gated CCD based camera system capable of operating at speeds of better than 1 frame/ $\mu\text{s}$ , and producing high resolution images. This system is already being used to evaluate the proton radiography concept. We have also designed, built, and beam tested a 64 pixel silicon detector based system that meets all the current performance requirements for the final AHF system with the exception of pixel size and some aspects of noise performance. The noise performance issue is apparently not in the electronics, but instead is linked to nuclear interactions of the probing proton beam in the detector and the very high proton beam intensity we have. Several solutions to this problem seem to exist and will be evaluated in detail in the near future.

<sup>1</sup> H.-J. Ziock et al., "The Proton Radiography Concept", these proceedings.

<sup>2</sup> H. Bichsel, Nucl. Instr. and Meth. **B52** (1990) 136.

<sup>3</sup> C. T. Mottershead and J. D. Zumbro, "Magnetic Optics For Proton Radiography", Proceedings of the Particle Accelerator Conference, Vancouver, Canada, May 1997.

<sup>4</sup> IMCO ELECTRO-OPTICS, LTD., 14/16 Safron Ct., Southfield Industrial Park, Basildon, Essex SS15 6SS, UK.

<sup>5</sup> "Measured Responsivities of Generation II and Hybrid Image Intensifiers", G. J. Yates and Nicholas S. P. King, SPIE Vol. 2551, Photoelectronic Detectors, Cameras, and Systems, pp. 145-158, July 13-14, 1995, San Diego, California.

<sup>6</sup> N. S. P. King, G. J. Yates, S. A. Jaramillo, J. W. Ogle, and J. L. Detch Jr., "Nanosecond Gating Properties of Proximity-Focused Microchannel-Plate Image Intensifiers", Los Alamos Conference on Optics, SPIE Vol. 288, pp. 426-433, April 7-10, 1981, Santa Fe, New Mexico.

<sup>7</sup> See for instance H. W. Funk, "Introduction to Image Intensifier Tubes", PROXITRONIC, Robert-Bosch Str. 34, D-64625 Bensheim, Germany.

<sup>8</sup> Directed Energy Inc., 2401 Research Blvd, Suite 108, Fort Collins, CO 80526, USA.

<sup>9</sup> Delft Electronic Products BV, P.O. Box 60, NL 9300AB Roden, The Netherlands.

<sup>10</sup> G. J. Yates et al., "An Intensified/Shuttered Cooled CCD Camera for Dynamic Proton Radiography", Proceedings of Electronic Imaging '98 Conference, 24-30 January 1998, San Jose, CA.

<sup>11</sup> Lawrence Semiconductor Research Laboratory, Inc., 2300 West Huntington Drive, Tempe, Arizona 85282, USA.

<sup>12</sup> L. Landau, J. Phys. USSR **8** (1994) 201.

<sup>13</sup> H. Bichsel and R. P. Saxon, Phys. Rev., **A11** (1975) 1286.

<sup>14</sup> E. Moore, U. of New Mexico, USA, private communication.

<sup>15</sup> Hamamatsu Corporation S4753-02 photodiode, typical QE @425 nm is 82% (0.28 A/W).

## THE PROTON RADIOGRAPHY CONCEPT

H.-J. Ziock, K. J. Adams, K. R. Alrick, J. F. Amann, J. G. Boissevain, M. L. Crow, S. B. Cushing, J. C. Eddleman, C. J. Espinoza, T. T. Fife, R. A. Gallegos, J. Gomez, T. J. Gorman, N. T. Gray, G. E. Hogan, V. H. Holmes, S. A. Jaramillo, N. S. P. King, J. N. Knudson, R. K. London, R. P. Lopez, J. B. McClelland, F. E. Merrill, K. B. Morley, C. L. Morris, C. T. Mottershead, K. L. Mueller, Jr., F. A. Neri, D. M. Numkena, P. D. Pazuchanics, C. Pillai, R. E. Prael, C. M. Riedel, J. S. Sarracino, H. L. Stacy, B. E. Takala, H. A. Thiessen, H. E. Tucker, P. L. Walstrom, G. J. Yates, J. D. Zumbro  
(Los Alamos National Laboratory, Los Alamos, NM 87545)

E. Ables, M. E. Aufderheide, P. D. Barnes Jr., R. M. Bionta, D. H. Fujino, E. P. Hartouni, H.-S. Park, R. Soltz, D. M. Wright  
(Lawrence Livermore National Laboratory, Livermore, CA 94550)

S. Balzer, P. A. Flores, R. T. Thompson  
(Bechtel, Nevada, Los Alamos Operations, Los Alamos, NM 87545)

R. Prigl, J. Scaduto, E. T. Schwaner  
(Brookhaven National Laboratory, Upton, NY 11973)

A. Saunders  
(University of Colorado, Boulder, CO 80309)

J. M. O'Donnell  
(University of Minnesota, Minneapolis, MN 55455; current address: Los Alamos National Lab)

### ABSTRACT

Proton radiography is a new tool for advanced hydrotesting. It is ideally suited for providing multiple detailed radiographs in rapid succession ( $\sim 200$  ns between frames), and for work on thick systems ( $100$ 's of  $g/cm^2$  thick) due to the long nuclear interaction lengths of protons. Since protons interact both via the Coulomb and nuclear forces, protons can simultaneously measure material amounts and provide material identification. By placing cuts on the scattering angle using a magnetic lens system, image contrast can be enhanced to give optimal images for thick or thin objects. Finally the design of a possible proton radiography facility is discussed.

### INTRODUCTION

We have developed a versatile new technique for obtaining a large number of flash radiographs in rapid succession. Our work is in support of the US Department of Energy's Science Based Stockpile Stewardship (SBSS) program and, in particular, is aimed at developing a concept for the Advanced Hydrotest Facility (AHF). The cessation of all underground nuclear weapons tests by the United States in accord with a proposed Comprehensive Test Ban Treaty has presented a significant challenge for the Department of Energy (DOE) nuclear weapons program with respect to certifying the performance, reliability, and safety of US nuclear weapons. The AHF is to be the ultimate above ground experimental tool for addressing physics questions relating to the safety and performance of nuclear weapon primaries.<sup>1</sup> In particular, the goal of the AHF is to follow the hydrodynamic evolution of dense, thick objects driven by high explosives.

The radiographic technique we developed uses high energy protons as the probing particles. The technique depends on the use of magnetic lenses to compensate for the small angle multiple Coulomb scattering (MCS) that occurs as the charged protons pass through the object under study. The use of a magnetic lens turns the otherwise troubling complications of MCS into an asset. Protons undergo the combined processes of nuclear scattering, small angle Coulomb scattering, and energy loss, each with its own unique dependence on material properties {atomic weight, atomic number ( $Z$ ), electron configuration, and density}. These effects make possible the simultaneous determination of both material amounts and material identification. This multi-phase interaction suite also provides the flexibility to tune the sensitivity of the technique to make it useful for a wide range of material thicknesses.

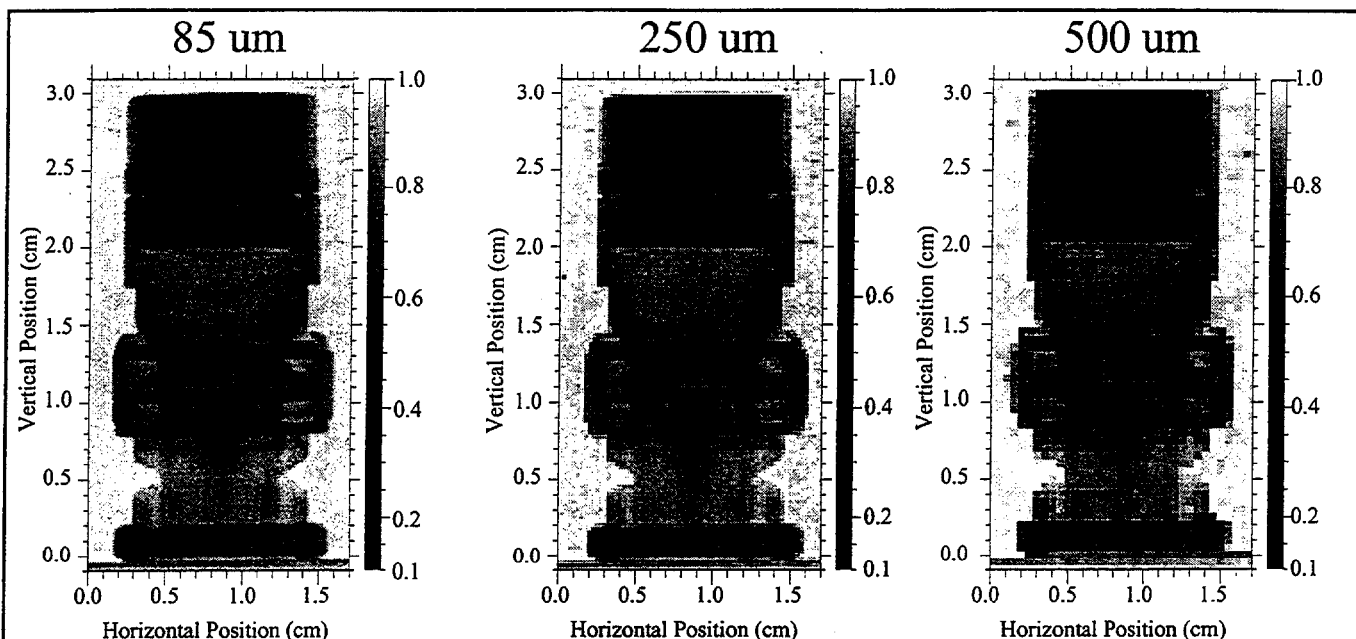


Fig. 1. A digitized phosphor image plate<sup>3</sup> proton radiograph of a 50Ω BNC terminator. The initial image (left) was digitized with  $(85 \mu\text{m})^2$  pixels. For the central and right images, pixels in 3-by-3 and 6-by-6 areas from the left image were summed.

The magnetic optics provides a means of maintaining unit magnification between the object and the image and the ability to move the image and hence detector planes far from the explosive object under test. This greatly improves the signal to background value and reduces the complexity of the blast protection scheme for the detectors. The magnetic lens system also provides the capability to change the angular acceptance, which is crucial for the ability to perform material identification and to tune the sensitivity for objects of very different thicknesses.

Protons offer a number of other advantages as probing particles in radiography as they can be detected with 100% efficiency and the same proton can be detected multiple times by multiple detector layers. For applications, such as those foreseen at the AHF, where thick dense dynamic objects need to be radiographed multiple times in very rapid succession, protons are nearly ideal solutions as they are highly penetrating, and the proton sources (accelerators) naturally provide the extended trains of short duration, high intensity beam bursts that are required. A single accelerator can easily provide enough intensity to allow the beam to be split many times to provide the multiple beams needed for simultaneous views of the object allowing 3-D tomographic "movies" to be made, the ultimate goal of the AHF.

The following sections of this paper will present an overview of the principles of high energy proton radiography (PRAD), their implementation, and how these mesh with the currently perceived performance requirements for the AHF. In addition, some of our initial PRAD results using both the 800 MeV beam available at the Los Alamos Neutron Scattering Center (LANSCE) and a secondary 10 GeV proton beam at the Alternating Gradient Synchrotron (AGS) at the Brookhaven National Laboratory (BNL) will be given. Finally, a possible design for an AHF is examined. In a separate paper<sup>2</sup> in these proceedings, we discuss the detector development effort associated with our work on PRAD.

## GOALS

Performance requirements for the AHF are given in Table 1. In addition to the high frame rate requirements, high resolution images are needed. A feeling for resolution can be gathered from Fig. 1, in which pixels from a proton radiograph image have been averaged to ever coarser bins. The high resolution, high contrast capabilities must be achieved even for radiographs of "thick"

Table 1: Desired AHF Performance Parameters

Spatial Resolution	better than 1 mm (FWHM)
Object thickness	up to 100's of $\text{g/cm}^2$
Thickness accuracy	$\sim 1\%$ pixel by pixel
Interframe spacing	from $\sim 100$ ns to many $\mu\text{s}$
# of frames	at least 10
Velocities to freeze	speeds of km/s
Views for 3D imaging	4 to 16

objects, where "thick objects" are measured in units of 100's of g/cm<sup>2</sup>. Thick objects strongly attenuate the beam of probing particles in their region of maximum thickness, and potentially produce large amounts of background by scattering particles from thinner regions of the object into the area of the image corresponding to the thickest part of the object where few direct particles penetrate. Background issues are further complicated by the need to view the object simultaneously from several directions, leading to the potential for scattering particles from one source into the detectors corresponding to another source. Tied to the requirement for high precision measurements is the desire to obtain maximum precision with a limited budget of probing particles. This is further constrained by the dynamic range of the detector system, which must count the number of transmitted particles in both the thin and thick regions of the object. In the following section, the properties of the ideal probing particle will be derived, and we will show that protons come very close to being such particles.

### DESIRED PARTICLE ATTENUATION LENGTH

With a fixed budget of incident particles, one can calculate the ideal attenuation length ( $\lambda$ ) for the probing particles when radiographing an object of a given thickness ( $L$ ). The ideal attenuation length will be the one that minimizes the fractional error in the difference between the number of particles transmitted by two regions of the object that differ in thickness by an amount  $T$ . We start by assuming simple exponential attenuation of the beam by the object

$$N(L) = N_o \exp(-L/\lambda), \quad (1)$$

where  $N_o$  is the number of incident particles per pixel, which is assumed to be known. The difference in the number of particles transmitted through the two regions is given by

$$N(L) - N(L+T) = N_o \exp(-L/\lambda) - N_o \exp(-(L+T)/\lambda) = N_o \exp(-L/\lambda) [1 - \exp(-T/\lambda)]. \quad (2)$$

The error in the result given by eq. (2) is simply the square root of the sum of the squares of the errors in each of the terms in the difference. Since, from counting statistics, the square of the error in  $N(L)$  is simply  $N(L)$ , we have

$$\text{error in difference} = [N(L) + N(L+T)]^{1/2} = [N_o \exp(-L/\lambda)]^{1/2} [1 + \exp(-T/\lambda)]^{1/2}. \quad (3)$$

In the limit of  $T \rightarrow 0$ ,  $\exp(-T/\lambda) \rightarrow 1 - T/\lambda$ , and eqs. (2) and (3) become respectively

$$N(L) - N(L+T) = N_o \exp(-L/\lambda) [T/\lambda] \quad (4)$$

$$\text{error in difference} = [N(L) + N(L+T)]^{1/2} = [N_o \exp(-L/\lambda)]^{1/2} [2]^{1/2}. \quad (5)$$

Taking the ratio of eq. (5) to eq. (4) in order to get the fractional error gives

$$\text{fractional error in difference} = [2N_o \exp(-L/\lambda)]^{1/2} / \{N_o \exp(-L/\lambda) [T/\lambda]\} = 2^{1/2} T^{-1} \lambda N_o^{-1/2} \exp(L/2\lambda). \quad (6)$$

Taking the derivative of that with respect to  $\lambda$  and setting the result to zero in order to find the value of  $\lambda$  that minimizes the fractional error gives

$$(d/d\lambda) [\text{fractional error in difference}] = (2N_o)^{-1/2} T^{-1} \exp(L/2\lambda) [1 - L/2\lambda] = 0. \quad (7)$$

Solving for  $\lambda$ , we find

$$\lambda = L/2, \quad (8)$$

namely the optimal attenuation length is one half the object thickness. Thus for thick objects measured in units of 100's of g/cm<sup>2</sup>, one wants attenuation lengths measured in the same units, not in 10's of g/cm<sup>2</sup>. Table 2 gives nuclear interaction lengths for high energy protons (above kinetic energies of ~800 MeV nuclear interaction length values are largely energy independent) and attenuation lengths for 5 MeV x-rays (which have approximately the maximum penetrating depths in high  $Z$  materials). Also presented are the resulting *fractional error in difference* values as calculated using eq. (6) and assuming  $N_o = 100,000$  and  $T = 0.01 * L$  (i.e. a 1% thickness difference effect). Since this fractional error must be less than one for there to be any chance of seeing the thickness difference, the table clearly demonstrates the advantage of protons for thick, high  $Z$  objects.

### MULTIPLE COULOMB SCATTERING

Unlike x-rays, protons undergo a random walk as they pass through an object due to the myriad of small angle charged particle collisions they have with the atoms in the object. This multiple Coulomb scattering (MCS), at first glance appears to be a great disadvantage for proton radiography since the protons no

Table 2: Nuclear interaction lengths for protons and x-ray attenuation lengths<sup>4</sup> and the *fractional error in difference values* for a 1% thickness difference and 100,000 incident particles per pixel.

	High Energy Protons ( $\sim \geq 1$ GeV)				5 MeV x-rays			
material	hydrogen	graphite	iron	lead	hydrogen	graphite	iron	lead
$\lambda$ (g/cm <sup>2</sup> )	50.8	86.3	131.9	194.0	21	38	34	23
$X_o$ (g/cm <sup>2</sup> )	63.05	42.70	13.84	6.37				
$L$ (g/cm <sup>2</sup> )								
10	2.51	4.09	6.13	8.90	1.19	1.94	1.76	1.28
20	1.38	2.17	3.18	4.57	0.76	1.11	1.02	0.79
50	0.74	1.03	1.43	1.97	0.62	0.66	0.63	0.61
100	0.61	0.69	0.86	1.12	1.02	0.63	0.66	0.90
200	0.81	0.61	0.63	0.73	5.49	1.18	1.44	3.98
500	6.23	1.40	0.79	0.63	2779.31	24.46	47.46	1081.10

longer travel in a straight line, and an image, unless taken immediately downstream of the object, will be blurred because of the angular dispersion. (Even immediately downstream of the object, some blurring due to the random walk will be evident.) To first order, the plane projected MCS angular distribution of the protons leaving the object is a Gaussian characterized by a root mean square (*rms*) plane projection deflection angle  $\theta_o$  which is given by the expression<sup>4</sup>

$$\theta_o(z) = 0.0136 \text{ GeV } (\beta c p)^{-1} (z/X_o)^{1/2} [1 + 0.038 \ln(z/X_o)] \quad (9)$$

where  $c$  is the velocity of light,  $\beta c$  is the velocity of the proton,  $p$  is its momentum, and  $z/X_o$  is the thickness of the object,  $z$ , measured in units of radiation length,  $X_o$ . It should be noted that as the  $\beta$  of the proton approaches one,  $\theta_o$  depends inversely on the momentum of the proton, and only grows as the square root of the object thickness. (The logarithmic term is on the order of 10% and has been ignored here.) The MCS has two effects. The first is the random walk itself, which leads to the limited blurring previously mentioned and is characterized by plane projection *rms* deviation,  $y$ , of the proton from its unscattered location by the time it reaches the end of the object. That is given by

$$y(z) = 3^{-1/2} z \theta_o(z). \quad (10)$$

The second is the additional blurring due to the random direction of the protons from MCS as they leave the object and travel to the detector, which will be located a non-zero distance from the object. The first effect can be dealt with by simply raising the proton beam momentum. To set the scale, for proton beams of 2, 5, 20, and 50 GeV/c beam, for a 20 radiation length object which is 10 cm thick,  $y = 2.16, 0.80, 0.20$ , and 0.08 mm respectively. As seen from eqs. (9) and (10), the results improves linearly as the beam momentum is increased, but grow worse as the product of the linear thickness of the object and the square root of the thickness of the object in radiation lengths. Since the object one wants to radiograph has a known thickness, by choosing a sufficiently high momentum, the blur can be reduced to any desired value. The *rms* angles  $\theta_o$  for the same geometry and beam momenta are 37.4, 13.8, 3.4, and 1.4 milliradians respectively. Since we intend to look at explosively driven dynamic objects, the detectors need to be quite distant from the object. Thus the second effect must be dealt with by a different means. The solution here relies on the fact that protons are charged and therefore their trajectories can be bent by a magnetic field. More specifically, one builds a magnetic lens. The center of the object is then placed at the object plane of the long focal length magnetic lens. Similar to an optical lens, the magnetic lens collects all the protons within its solid angle acceptance, and, regardless of their angle of emission from a point in the object plane, puts them all back at the corresponding point in the image plane.

## MAGNETIC LENS AND MATERIAL IDENTIFICATION

The overall magnetic lens system we have designed<sup>5</sup> is shown schematically in Fig. 2. The two imaging lens cells thereof are inverting identity (−I) lenses. These cells are each comprised of four identical quadrupole magnets operated at identical field strengths, but alternating polarities (+ − + −). They have the feature that at the center of the gap between the two middle magnets of a cell, the protons are sorted radially solely by their scattering angle in the object, regardless of which point in the object plane they originated from. This allows one to place a collimator at that location and use it to make cuts on the MCS

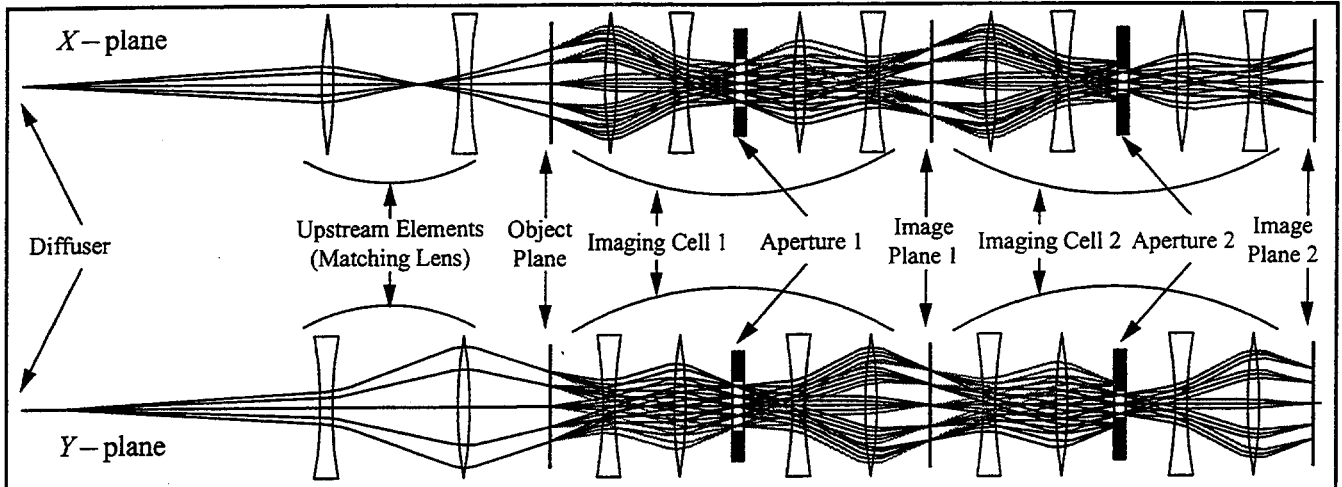


Fig. 2 Schematic of the PRAD magnetic lens system showing both the  $X$  and  $Y$  views. The beam is first prepared with a diffuser and matching lens to meet optics requirements. It then passes through the object being radiographed. The transmitted beam passes through an iris, or aperture located in the middle of the 4-quadrupole -I magnetic lens cell and is focused on the first detector. It then enters the second identical -I lens cell, which this time has a smaller diameter iris, and is focused on a second detector. Together, the two detectors provide the information needed to reconstruct both the density profile and material composition of the object.

angle in the object. As noted previously, the scattering angle distribution is approximately a Gaussian with a width, which, by eq. (9), depends on the number of radiation lengths of material the protons passed through. With the collimator, one can limit the transmitted particles to only those with an MCS angle less than the cut angle ( $\theta_c$ ). The number of transmitted particles  $N_c$  after such a cut is given by

$$N_c \approx N \int_0^{\theta_c} \frac{1}{2\pi\theta_o} \exp\left(-\frac{\theta^2}{2\theta_o^2}\right) d\Omega \approx N \left[1 - \exp\left(-\frac{\theta_c^2}{2\theta_o^2}\right)\right], \text{ or } \frac{N_c}{N} \approx \left[1 - \exp\left(-\frac{\theta_c^2}{2\theta_o^2}\right)\right] \quad (11)$$

where  $N$  is the number of incident particles. Note that when  $\theta_c \gg \theta_o$ ,  $N_c = N$ , as expected. Using eq. (9) for  $\theta_o$ , ignoring the small logarithmic term, and solving for  $z/X_o$  gives

$$\frac{z}{X_o} \approx \frac{-\theta_c^2}{2\left(\frac{13.6 \text{ MeV}}{\beta c p}\right)^2 \ln\left(1 - \frac{N_c}{N}\right)} \quad (12)$$

If we now build a lens system which consists of two of the -I lenses set back to back, the first with an aperture sufficient to pass essentially all the particles scattered by MCS (but not those scattered by inelastic nuclear interactions), the second with its aperture set so that it cuts into the MCS distribution, and then place detectors at the image planes of the two lenses, we get two independent measurements. The first depends on the number of nuclear interaction lengths of material in the object, while the second depends on the number of radiation lengths of material in the object. Since the values of nuclear interaction length and radiation length have different dependencies on material type as shown in Table 2, we are in a position to determine both the amount of material in the object and what that material is. If the object has transitions from one material type to two material types and then from two to three material types, ..., we can unfold the object in terms of material types and thickness for each material. (Note that a 1 to 2 material step followed by a 2 to 3 material step can be unfolded, but a sudden 1 to 3 material step cannot be unfolded.)

It should also be noted that by using a single magnetic lens with just a MCS angle cut, one can achieve high contrast proton radiography even when the object is too thin to provide good contrast using nuclear attenuation. Just as was the case for nuclear exponential beam attenuation, for pure MCS based radiography of a given thickness object, there is an ideal cut angle that maximizes sensitivity to changes in object thickness. The value of that optimal cut angle can be determined by the same process as lead to eq. (8), but for an attenuation that is given by eq. (11). Thus by changing the aperture to provide that optimal

MCS angle cut, one can tune the system to provide optimum sensitivity, regardless of the object thickness. This was done for the image shown in Fig. 1.

As can be seen in Fig. 2, the magnetic lens system has some additional elements upstream of the object. The proton beam passes through a thin diffuser, which gives a small angular divergence to the beam and then passes through a set of magnets, which introduces a correlation between the radial position of a proton in the object plane and its angle. This is done to reduce magnetic lens induced aberrations in the identity lens cells. These aberrations are both geometric and chromatic in nature. For the particular momentum to which the lens is tuned, the relation between the location of a particle in the object plane,  $x_{object}$ , and its location in the image plane,  $x_{image}$ , for a magnetic lens is given by

$$x_{image} = R_{11}x_{object} + R_{12}\phi_x \quad (13)$$

where  $\phi_x$  is the angle of the particle in the  $x$ -plane relative to the axis of the lens, and the  $R$ 's are constants, which characterize the magnetic lens. A similar equation holds for the  $y$ -coordinate. If instead of having beam particles with a single momentum ( $p$ ), the particles have a spread in momentum,  $\delta p$ , eq. (13) becomes

$$x_{image} = (R_{11} + \Delta R_{11}' + \text{higher order terms})x_{object} + (R_{12} + R_{12}'\Delta + \text{higher order terms})\phi_x \quad (14)$$

where  $\Delta = \delta p/p$  and the  $R'$  coefficients are distortion constants for the lens. When an object is placed in the object plane, several things happen to the transmitted proton beam. First, the protons lose energy and thus momentum; their final average momentum  $p$ , being less than their incident momentum  $p_o$ . The momentum loss in the object is not single valued, but instead covers a range  $\pm \delta p$  due to random nature of the energy loss process and variations in the thickness of the object. Also, through MCS, an angular divergence is introduced to the beam, which is characterized by  $\theta_o$ , as given by eq. (9).

We are free to arrange the incident proton beam so that all the particles incident on the object plane have a relation between their angle and location in that plane given by  $\phi_x = wx$ . Combining this with the effect of the MCS, we have  $\phi_x = wx + \theta_o$  for the outgoing beam. Assuming the magnetic lens is tuned to the average momentum of the transmitted protons, eq. (14) becomes

$$x_{image} = R_{11}x_{object} + R_{12}\phi_x + (R_{11}' + wR_{12}')x_{object}\Delta + R_{12}'\theta_o\Delta + \text{higher order terms} \quad (15)$$

Making use of the fact that we have a  $-1$  lens, which implies  $R_{11} = -1$  and  $R_{12} = 0$ , and ignoring the *higher order terms*, eq. (15) becomes

$$x_{image} = -x_{object} + (R_{11}' + wR_{12}')x_{object}\Delta + R_{12}'\theta_o\Delta \quad (16)$$

We note that if we choose  $w$  such that  $w = -R_{11}'/R_{12}'$ , the  $x_{object}\Delta$  term in eq. (16) becomes identically equal to zero, and thus all position dependent chromatic aberration terms vanish. The matching magnets upstream of the object are used to establish that correlation,  $w$ , between  $x$  and  $\phi_x$ . Thus eq. (16) becomes

$$x_{image} = -x_{object} + R_{12}'\theta_o\Delta, \quad \text{provided:} \quad w = -R_{11}'/R_{12}' \quad (17)$$

In addition to the matching lens establishing the desired correlation between incident particle angle and location at the object plane, the lens provides some other useful functions. It further expands the incident beam allowing one to illuminate a large object, without making the upstream diffuser very thick. It also helps maintain a very uniform acceptance across the full field of view of the imaging lenses.

## MOMENTUM SCALING

The remaining distortion term in eq. (17) is given by

$$\Delta x = x_{object} + x_{image} = R_{12}'\theta_o\Delta, \quad (18)$$

which is characterized by the chromatic aberration coefficient of the lens,  $R_{12}'$ , and the product  $\theta_o\Delta$ . For high momentum protons ( $> 1$  GeV/c), the momentum loss is essentially independent of beam momentum. Therefore the fractional momentum bite of the beam,  $\Delta$ , scales inversely proportional to the beam momentum. Likewise from eq. (9), the angle  $\theta_o$  is also inversely proportional to the beam momentum. Thus the spatial resolution of the magnetic lens system improves as the square of the beam momentum.

Other factors also effect the overall spatial resolution that can be attained in proton radiography. There is the spatial resolution of the detector system, which is essentially independent of momentum. There is also the effect of the non-zero thickness of the object, which by eq. (10) degrades the resolution. As discussed earlier, this effect scales as  $1/p$ . If there is a vessel to contain the explosive blast in an AHF application,



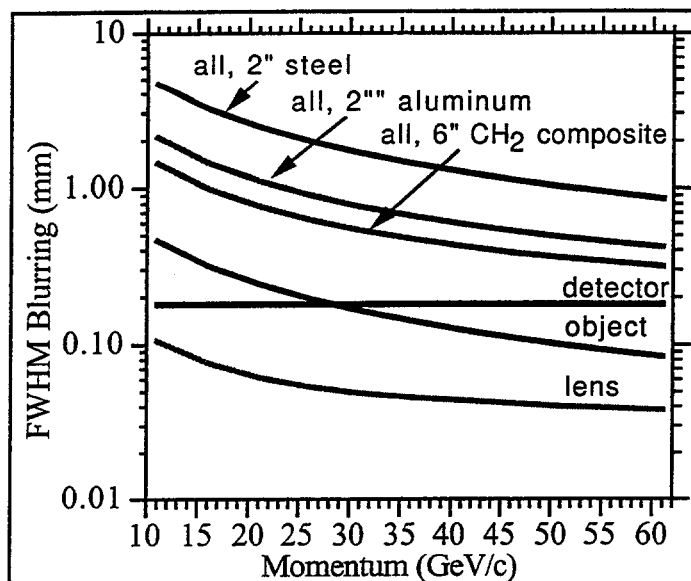


Fig. 3. The momentum scaling for the various terms effecting spatial resolution. Shown are possible individual contributions from the detector, object, and lens, and the overall contribution when these are combined with different containment vessels values.

chromatic spatial aberrations from the lens, which were already a higher order effect. In Fig. 3 we plot the expected overall spatial image blurring as a function of beam momentum for the various terms and various containment vessel walls.

## PROTON DETECTION

Protons, being charged particles, directly excite the detector medium, predominantly through Coulomb interactions with electrons in the medium. They thus generate a signal even for an extremely thin detector. Because of the mass difference between protons and electrons, there is very little deflection of the protons by the detector, and therefore very little in the way of a detector produced background problem. In contrast, x-rays, being uncharged, do not directly ionize the detector material as they pass through it. As a matter of fact, it takes one x-ray attenuation length for 63% of the x-rays to interact and generate a charged particle, which then leaves the excitation trail that a detector sees. X-rays predominantly interact through large angle scattering, and due to the large required detector thickness are likely to have secondary interactions that produce backgrounds in the detector. Since protons can be detected by very thin detectors, no similar problem exists for them. Also in a thin detector, the proton is virtually undeflected and therefore can be used for a second (or third) time, such as in a second magnetic lens system for MCS material identification. Furthermore, multiple planes of detectors can detect the same proton, thereby achieving redundancy. The thinness of the proton detectors also makes them essentially blind to neutral secondary particles generated in the object (neutrons and  $\gamma$ -rays), thereby reducing the potential for other background problems.

## BACKGROUNDS

Backgrounds in the case of proton radiography are very small, as we have verified both in Monte Carlo studies and in experiments. This results from the relatively long values of interaction (attenuation) lengths for protons and the large standoff distance for the detectors from the object, which is due to the magnetic lens system. The magnetic lens also provides filtering of off-momentum background particles. At the same time, the thin detectors are essentially blind to neutral secondary particles, which would otherwise dominate the relatively small background. In neither proton nor x-ray radiography are the "attenuated" particles cleanly removed from the beam. Some fraction of the "attenuated beam" will undergo one or several hard interactions in the object and/or surrounding material and still hit the detector in a location that

the MCS of the incoming and outgoing beams in the vessel walls will produce a similar effect, but this time linearly dependent on the separation between the object and the containment vessel wall. Due to the relatively large value of this distance, this will likely be the dominant term effecting spatial resolution. The MCS in the vessel wall will change the value of the outgoing proton angle, which cannot be corrected for by the magnetic lens. This characteristic angle change multiplied by the distance from the object to the vessel wall will be the amount of blur introduced. (If the vessel wall is closer to the image plane than the object plane, the relevant distance is the vessel wall to image plane separation.) The characteristic angle involved is again given by eq. (9) and thus scales as  $1/p$ . As eq. (9) also shows, it depends on the thickness of the vessel wall in units of radiation length, and therefore it is important to use thin, low-Z materials. The vessel wall thickness is less important for the incident beam, since there it affects the desired correlation between the incident particle location at the object and the particle angle there. This correlation was to remove the

is uncorrelated to their ideal path through the object. Thus they contribute a background signal in the detector, which is indistinguishable from the real signal, thereby masking or greatly diminishing one's sensitivity to the small effects one is looking for in the object. This is clearly a signal to background issue. The signal depends on the ability to get a substantial number of particles directly through the thickest part of the object, and thus requires a very large number of incident particles for a thick object. The background level depends on a combination of factors, the most important of which are the variation in thickness across the object in terms of scattering or attenuation length, the probability of scattering in a given amount of material, and the number of incident particles.

The background will clearly be worst when the object is thick and there is a considerable variation in thickness across the object. At the thickest part of the object there will be very little signal as the beam is strongly attenuated. In the thinner parts of the object, scattering of the beam will occur with some of the scattered particles deflected into the detector region corresponding to the thickest part of the object and potentially causing a large fractional background there. Thus ideally one would like to tailor the beam intensity to be highest at the thickest part of the object, and to have the thickness of the object roughly comparable to the attenuation length of the material of which the object is made. This is exactly what one has in proton radiography. The upstream diffuser used to impart the small angular divergence to the incident beam produces an approximately Gaussian shaped beam profile which is peaked at the center of the beam where one can locate the thickest part of the object. The width of the Gaussian can also be adjusted by changing the diffuser thickness, depending on whether a more uniform or more peaked beam is desired. Furthermore, the interaction length of the protons is, or can be, well matched to the thickness of the object. In contrast, for x-rays, there is typically a poor match of attenuation length to object thickness, especially for thick objects. Also, since the x-ray source is essentially a point source, the beam intensity is nearly uniform across the object. In practice, for x-ray images, a graded collimator of varying thickness can be built that is matched to the object so the collimator – object combination present a uniform thickness to the x-ray beam. However, in the case of dynamic radiography, that becomes problematic at best. An added complication occurs when one has multiple beam lines and detectors needed to perform 3-D reconstructions of the object. Crosstalk between the different beam lines and detectors can then occur. Furthermore, additional beam is incident on the object due to the multiple beam lines. For protons the magnetic lens maintains the signal intensity between the object and the detector plane, while particles failing to pass the angular acceptance cut of the lens are either stopped internally in the lens, or fall off in intensity as the distance from the object to the detector squared. With the long length of the magnetic lens, there is virtually no background from other beam lines.

A numerical example of the background issue dramatically demonstrates the difference between protons and x-rays. We will use a very simplistic model that demonstrates the gross features of the issue. We take an object which has a maximum thickness  $L$ , and a minimum thickness of  $fL$ , where  $f < 1$ . The signal at the thickest part of the object is given by eq. (1)

$$\text{signal} \equiv S = N_0 \exp(-L/\lambda). \quad (19)$$

For a calculation of the background we again start with eq. (1), and substitute the distance the proton has penetrated into the object ( $x$ ) in place of  $L$ . We then calculate the differential of that in order to calculate, as a function of  $x$ , the number of protons which undergo a scattering in a length  $dx$ . Ignoring the leading minus sign, which indicates a loss of particles from the incident beam, this gives

$$dN(x) = N_0 \lambda^{-1} dx \exp(-x/\lambda). \quad (20)$$

Next we calculate the number of those  $dN(x)$  scattered particles that make it out of the object. We do this at the thinnest part of the object where the distance the particles still have to travel to get out of the object is  $fL - x$ . (We ignore the fact that the particles are now traveling at an angle to their original direction and therefore have a somewhat greater distance to travel.) This calculation is again done using eq. (1) and we find the number of *surviving scattered* =  $SS$  particles to be

$$SS = dN(x) \exp[-(fL-x)/\lambda] = N_0 \lambda^{-1} dx \exp(-x/\lambda) \exp[-(fL-x)/\lambda] = \{N_0 \lambda^{-1} \exp(-fL/\lambda)\} dx. \quad (21)$$

Integrating eq. (21) over the thickness of the object at its thinnest location (i.e.  $x: 0 \rightarrow fL$ ) gives

$$\text{total } SS = N_0 \lambda^{-1} fL \exp(-fL/\lambda). \quad (22)$$

To find the *background* we just need to multiply the *total surviving scattered* value by the detector fractional acceptance at the region of thickest part of the object for those scattered particles. We take this to

Table 3: Signal to background values assuming  $H = 0.001$ .

material	$\lambda_{\text{nuclear}}$ (g/cm <sup>2</sup> )	$\lambda_{5 \text{ MeV x-ray}}$ (g/cm <sup>2</sup> )	$L$ (g/cm <sup>2</sup> )	$f$	$(S/N_o)_{\text{nuclear}}$	$(S/N_o)_{\text{x-ray}}$	$S/B_{\text{nuclear}}$	$S/B_{\text{x-ray}}$	$R_{\text{nuclear}}$	$R_{\text{x-ray}}$
iron	131.9	34	304	0.2	0.1	1.32E-04	344	0.4	6.3	1269.2
iron	131.9	34	212	0.2	0.2	1.94E-03	857	5.4	3.6	147.7
iron	131.9	34	91	0.2	0.5	6.79E-02	4143	216.3	1.7	8.6
iron	131.9	34	304	0.5	0.1	1.32E-04	275	2.6	3.2	87.0
iron	131.9	34	212	0.5	0.2	1.94E-03	556	14.1	2.2	22.7
iron	131.9	34	91	0.5	0.5	6.79E-02	2040	193.9	1.4	3.8
lead	194.0	23	447	0.2	0.1	3.67E-09	344	4.60E-05	6.3	5595334.9
lead	194.0	23	312	0.2	0.2	1.27E-06	857	7.07E-03	3.6	52062.9
lead	194.0	23	135	0.2	0.5	2.89E-03	4143	8.0	1.7	107.5
lead	194.0	23	447	0.5	0.1	3.67E-09	275	6.24E-03	3.2	16496.5
lead	194.0	23	312	0.5	0.2	1.27E-06	556	1.66E-01	2.2	886.8
lead	194.0	23	135	0.5	0.5	2.89E-03	2040	18.4	1.4	18.6

be  $H$ . Thus we find the *signal to background* value  $= S/B$  is given by

$$S/B = N_o \exp(-L/\lambda) / [H N_o \lambda^{-1} f L \exp(-fL/\lambda)] = \lambda(HfL)^{-1} \exp[-(1-f)L/\lambda]. \quad (23)$$

In Table 3 are given some values of the  $S/B$  for different materials, values of  $L$ , and values of  $f$ , both for 5 MeV x-rays and high energy protons. Also given are the beam transmission probabilities  $(S/N_o)$  at the thickest part of the object. We take  $H = 0.001$ . It should be noted that due to the limited momentum transmission of the magnetic lens in proton radiography, the value of  $H$  for protons should be less than that for x-rays, improving the  $S/B$  value for protons relative to that for x-rays beyond the values shown.

A related issue addressed in Table 3 is the dynamic range required for the detector. If a uniform intensity beam is incident on the object, the ratio,  $R$ , of the signal intensity at the thinnest part of the object to that at the thickest part of the object (ignoring background) is given by

$$R = N_o \exp(-fL/\lambda) / [N_o \exp(-L/\lambda)] = \exp((1-f)L/\lambda). \quad (24)$$

As Table 3 shows,  $R$  can be quite large for x-rays, especially when  $\lambda$  is small compared to  $L$ . In looking at these values and considering the detector dynamic range and sensitivity, it is important to keep in mind that the detector must, in addition, be able to see on the order of a 1% change in object thickness at the thickest part of the object.

The preceding calculations do not deal with the production of secondary particles in the object due to nuclear interactions. We examined this issue in a Monte Carlo study which used the latest version of the LAHET<sup>6</sup> code, which in turn uses FLUKA<sup>7</sup> to simulate the nuclear scattering and particle secondary production. In the study, a zero diameter beam of 50 GeV protons was incident normal to a slabs of <sup>238</sup>U of different thicknesses. At the downstream face of the slab we recorded all outgoing particles. For those particles, their particle type, location, and 3-momentum were recorded. Neutrons were tracked down to kinetic energies of 20 MeV. Due to the inability of LAHET to directly deal with  $\gamma$ -rays, and electrons and positrons, these were ignored. The predominant source of  $\gamma$ -rays will be  $\pi^0$  decays, whose number will be about the same as those for  $\pi^+$  or  $\pi^-$ , the dominant secondary charged particles. As the  $\pi^0$  decays essentially instantaneously, into two  $\gamma$ -rays, by the above arguments, their number will initially be about equal to the number of secondary charged particles. However, the  $\gamma$ -rays will be strongly attenuated in the object, and the few surviving  $\gamma$ -rays will be spread over a large angular region and thus outside the angular acceptance of the magnetic lens system. Since they are also nearly invisible to the detectors, their omission should have a negligible effect on the results. Fig. 4 gives the angular distribution of all the particles making it out of the back of the slab sorted by particle type. Fig. 5 shows a similar plot, but for outgoing particle momentum. Both figures are for 500 g/cm<sup>2</sup> of uranium, a very thick object, where the background problem will be most severe. In Table 4, we record the signal and background values for cuts on the outgoing particle angle and momentum for different slab thicknesses. We consider signal particles to be protons which have angles inside the outgoing angle cut, and a momentum which is greater than the expected average momentum of protons exiting the slab minus 5%. As can be seen, secondary particles contribute very little, and the dominant secondary particles are neutral and thus essentially invisible to the detector.

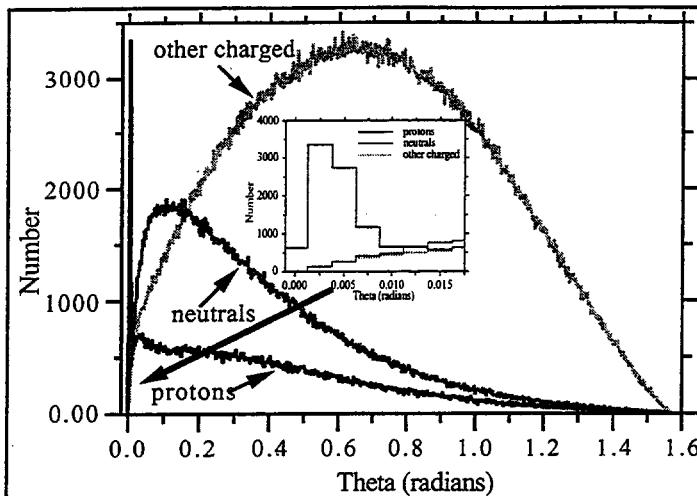


Fig. 4. Histograms of the number of outgoing particles of a particular type as a function of scattering angle for 100,000 incident 50 GeV protons on a 500 g/cm<sup>2</sup> slab of <sup>238</sup>U.

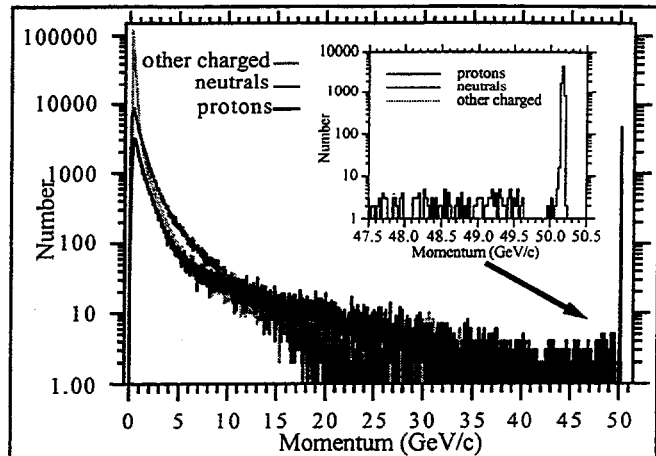


Fig. 5. Histograms of the number of outgoing particles of a particular type as a function of momentum for 100,000 incident 50 GeV protons on a 500 g/cm<sup>2</sup> slab of <sup>238</sup>U.

## EXPERIMENTAL WORK

We have carried out a number of experimental tests of the PRAD concept using magnetic imaging lenses. Some of these tests were carried out at the LANSCE facility, making use of its 800 MeV chopped proton beam. The 800 MeV beam energy is too low to allow for the study of thick objects in which nuclear attenuation is important. This is due to the large dispersion in momentum loss by the protons at 800 MeV, both directly and as a result of variations in object thickness. As discussed earlier, this results in poor lens performance and hence a blurred, poor quality image. However, by looking at thinner objects, we could still study the MCS part of the PRAD concept, the actual performance of the magnetic lens system, and by making use of the pulsed nature of the proton beam (one pulse every  $N \times 358$  ns,  $N$  = integer), take a sequence of radiographs of explosively driven events.

The ability to take high contrast, high resolution images using a MCS angle cut for a thin object is demonstrated by the image shown in Fig. 1, which is a static radiograph taken using a phosphor image plate as a detector. The object is a 50  $\Omega$  BNC terminator that is only 1.4 cm in diameter. The resistor and its leads inside the metal case of the terminator are clearly visible, as are the internal screw threads. Even submillimeter features are sharp. Radiographic images of a dynamic event are shown in Fig. 6. The object is a 58 mm diameter half-sphere of high explosive (HE) which is in the process of detonating. These images were again made with phosphor image plates. Four different explosive shots were fired to produce the four radiographs, with the proton beam timed to arrive at different times relative to the detonation initiation time. The different times are (top to bottom) 0.99  $\mu$ s, 1.90  $\mu$ s, 2.50  $\mu$ s, and 3.25  $\mu$ s after detonation initiation. Also shown are the results of a reconstruction of the object from those radiographs. The position of the shock front (the glitch in Fig. 6) associated with the detonation is seen to progress between the different radiographs. The shock front is seen to correspond to about a 30% increase in local

Table 4: Particle generation & survival in the given amount of <sup>238</sup> U				
	no cut	10 mrad $\theta$ cut	47.9 GeV/c momentum cut	momentum and $\theta$ cut
<b>50 g/cm<sup>2</sup></b>				
protons	151840	77756	77015	76761
neutrals	211620	633	21	11
other charged	196658	837	0	0
<b>100 g/cm<sup>2</sup></b>				
protons	182034	60733	59584	59184
neutrals	448298	1017	36	14
other charged	331171	1364	0	0
<b>200 g/cm<sup>2</sup></b>				
protons	212593	36998	35597	35134
neutrals	883247	1318	45	23
other charged	473650	1691	0	0
<b>500 g/cm<sup>2</sup></b>				
protons	168694	8209	7473	7160
neutrals	1319912	935	11	5
other charged	397354	1044	0	0

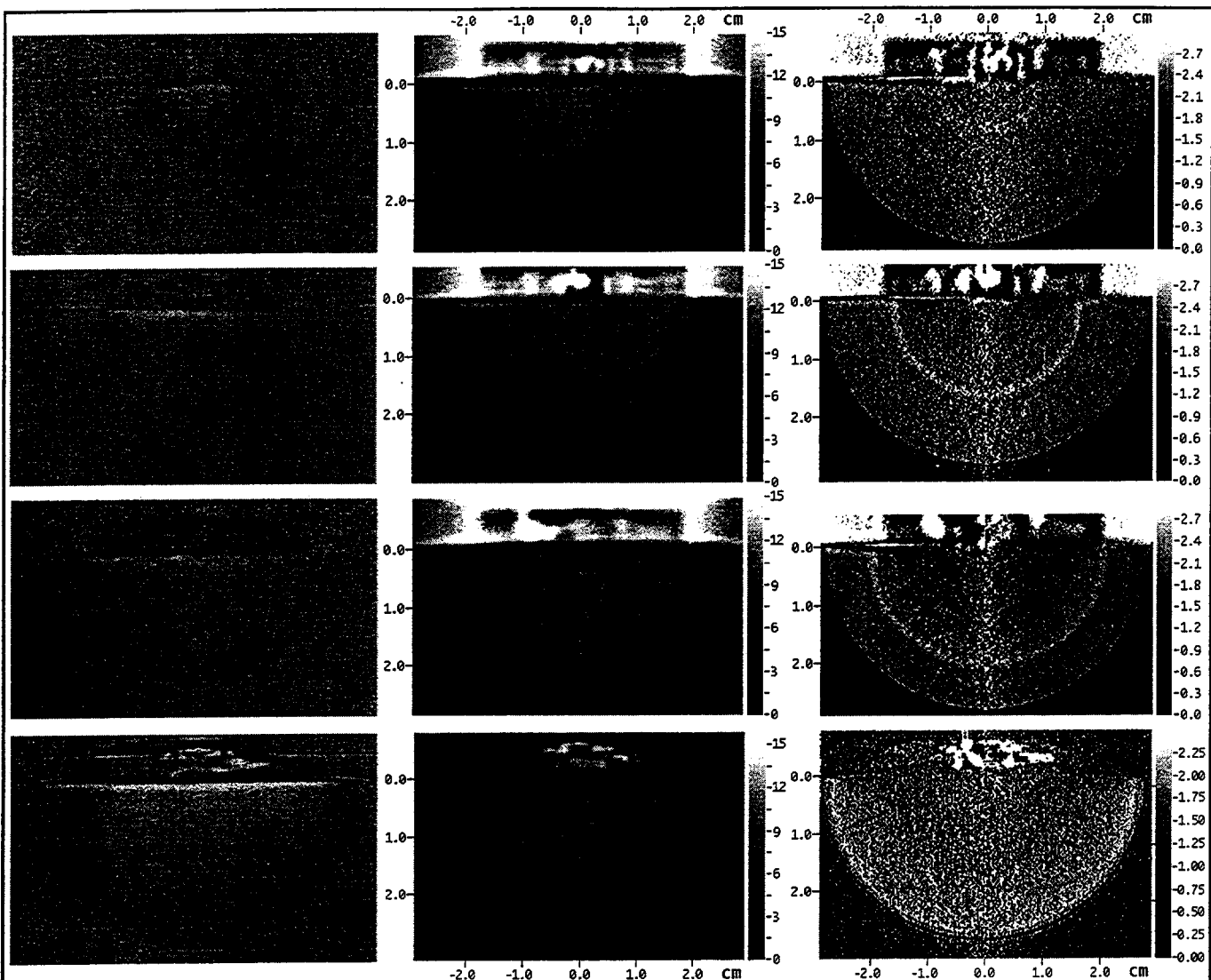


Fig. 6. Original data and reconstructions from phosphor image plate proton radiographs of a hemispherical piece of HE at different times following detonation (top to bottom: 0.99  $\mu$ s, 1.90  $\mu$ s, 2.50 $\mu$ s, and 3.25 $\mu$ s after detonation initiation). The left column is the ratio of a radiograph at the given time after detonation initiation to an identical radiograph taken prior to detonation. The central column gives the unfolded amount of material in units of g/cm<sup>2</sup> using the measured beam attenuation, the known radiation length for the HE material, and the known MCS angle cut. The right column is a reconstruction of the density of the material obtained using the preceding results and a hemispherical object shape. The reconstruction starts at the left and right edges of the object and works towards the vertical centerline of the object, resulting in the increased error seen towards the centerline.

density. Behind the shock front a rarefaction can also be seen. For the above images, the collimator inside the magnetic lens was set to provide a MCS angle cut of 10 milliradians.

To test the PRAD concept at higher energies, we made use of a 10 GeV secondary proton beam at the AGS at BNL. The various components of the experimental setup are shown in Fig. 7. As a secondary beam line was being used, the instantaneous proton beam flux was low, allowing us to use wire chambers to track the protons individually from upstream of the object location to the image plane of the magnetic lens. Images were made with both the wire chambers and phosphor image plates using long exposure times. One of the objects we imaged, also shown in Fig. 7, is known as the French Test Object (FTO) and consists of concentric spherical shells. The outer shell is a density 1/2 g/cc plastic foam and covers the radial region between 6.5 and 22.5 cm. The next inner shell is copper and is in the region between 4.5 and 6.5 cm. The third shell is a tungsten alloy and covers the region between 1 and 4.5 cm leaving an air

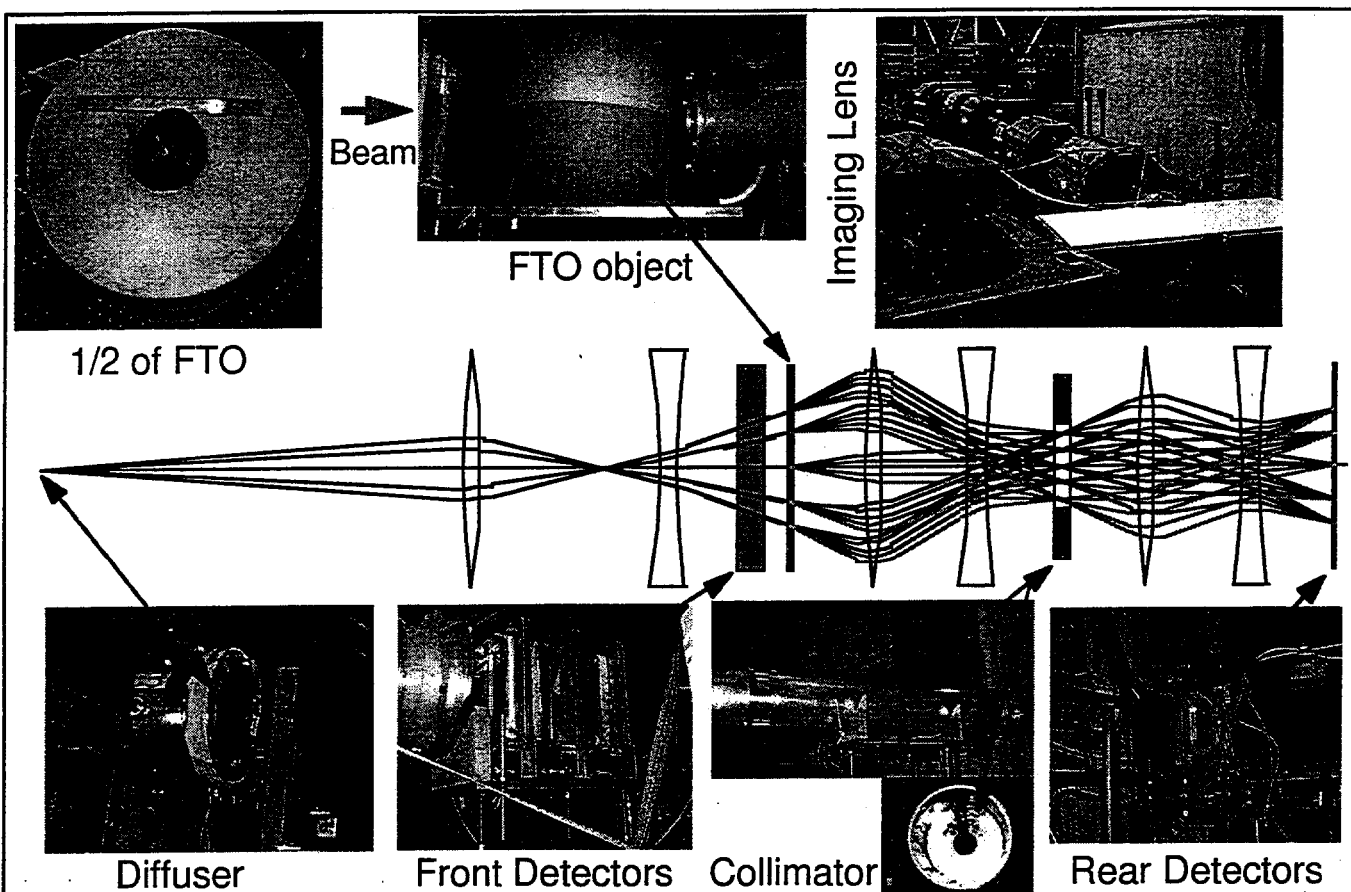


Fig. 7 Schematic of the PRAD magnetic lens system and actual components for EXP. 910 at the BNL AGS. The beam is first prepared with a diffuser and matching lens to meet optics requirements. Next the beam is measured just upstream of the object by the front detectors after which it passes through the object being radiographed. The transmitted beam passes through an iris, or aperture, located in the middle of the 4-quadrupole -I magnetic lens system and is focused on the rear detectors. The runs with different angle cuts were done separately using different collimators. The data from these runs provide the information needed to reconstruct both the density profile and material composition of the object.

cavity in the center. The maximum object thickness is  $213 \text{ g/cm}^2$ , just tangent to the central cavity. The magnetic lens system had an effective horizontal and vertical aperture of about  $\pm 7 \text{ cm}$ . Two sets of images were taken of the FTO, one with a collimator corresponding to  $\theta_c \sim 9 \text{ mrad}$ , and the second with a collimator corresponding to  $\theta_c \sim 4.5 \text{ mrad}$ . The first collimator passes nearly all of the MCS distribution but not the nuclear inelastically scattered particles, whereas the second cuts substantially into the MCS distribution. The resulting image plate radiographs are shown in Fig. 8. Fig. 9 shows the radial distributions resulting from those radiographs and the "radiographs" of the beam intensity incident on the object. The results of a reconstruction of the object are shown in Fig. 10 and are given in Table 5, which also gives the actual locations of the changes in the material type and the Particle Data Book<sup>4</sup> values for the nuclear interaction lengths and radiation lengths of the relevant materials. The results clearly demonstrate the ability to unfold material type and thickness.

We also used the wire chamber data to study background issues. The beam energy, although still a factor of about 5 less than that being discussed for the AHF, is sufficient to address most of the background problems, as one is well above the particle production threshold energies that will be most relevant at 50 GeV. The wire chambers consisted of multiple planes providing both X and Y information, which could in turn be used to provide particle direction information. As the magnetic lens used was a -I lens, summing the proton position at the object plane and the image plane should ideally give a value of zero regardless of the proton position in the object plane. This is shown in Fig. 11, where scatterplots of  $Y_{\text{SUM}} = Y_{\text{object}} + Y_{\text{image}}$  versus  $X_{\text{SUM}} = X_{\text{object}} + X_{\text{image}}$  are given. Also shown are scatterplots of the particle scattering angle vs.  $X_{\text{SUM}}$ . The upper left plot has a linear intensity scale showing that the vast

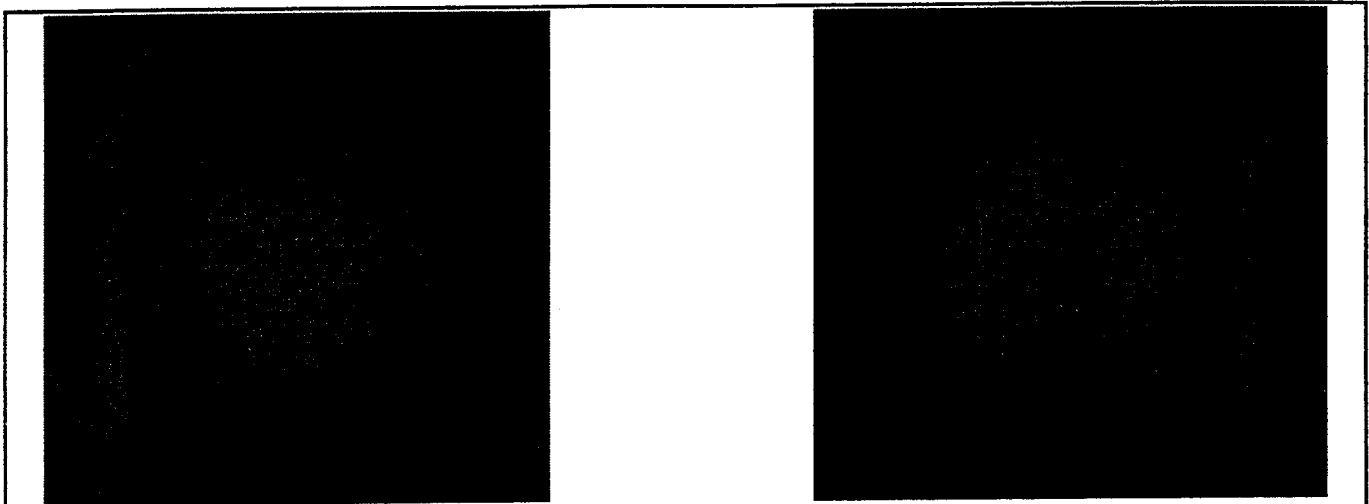


Fig. 8 Results from proton radiograph image plate pictures of the FTO. Shown are “negatives” of the beam distribution normalized images. The left (right) image corresponds to the ~9 (~4.5) mrad collimator. The slightly trapezoidal shaped region is the field of view of the magnetic lens. The outer edge of the copper shell nearly fills the field of view.

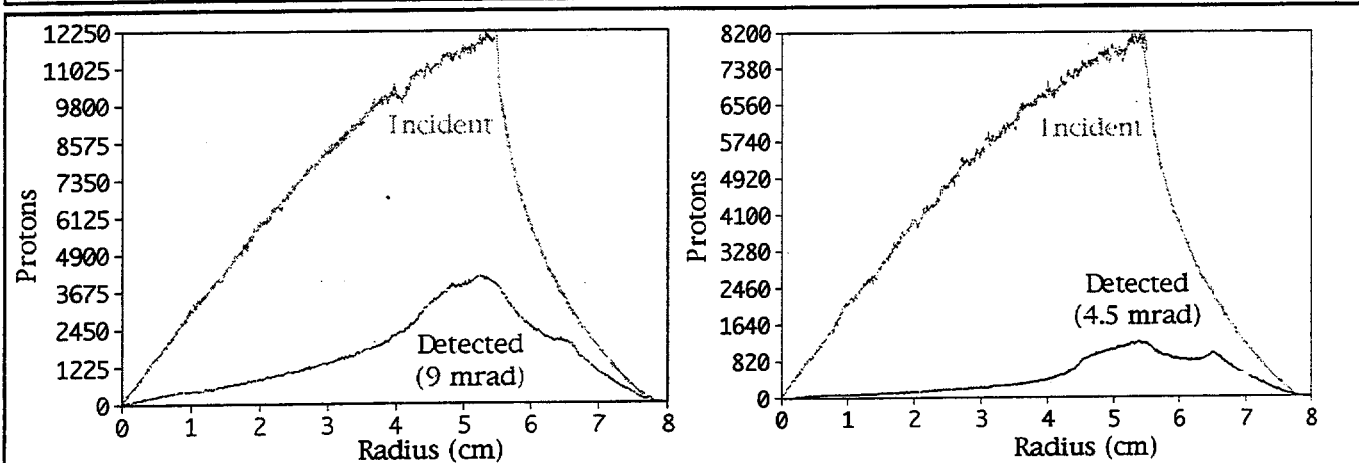


Fig. 9. Radial distributions for the radiographs of FTO similar to those given in Fig. 8, but using the wire chamber data. The left (right) plot is for the 9 (4.5) mrad collimator. The upper (lower) curve is the number of incident (transmitted) particles. The drop to zero in the radial distributions as zero radius is approached is simply a solid angle effect.

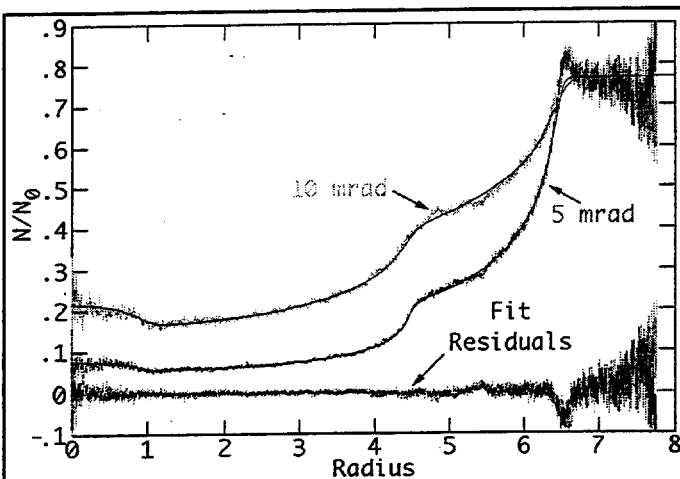


Fig. 10. Fits to the transmission data for the FTO. The upper two curves are the measured transmission vs. radius. The bottom overlaid curves are the residuals of the two fits.

Table 5: Fitting results.				
Material	Radius (cm)	$\lambda$ (cm)	$X_0$ (cm)	
Void	0.98	—	—	Fit
	1.00	0.0	0.00	Real
Tungsten alloy	4.48	10.5	0.38	Fit
	4.50	10.1	0.37	Real
Copper	6.47	14.2	1.10	Fit
	6.50	15.1	1.42	Real
Foam	—	—	—	Fit
	22.50	160.0	84.00	Real

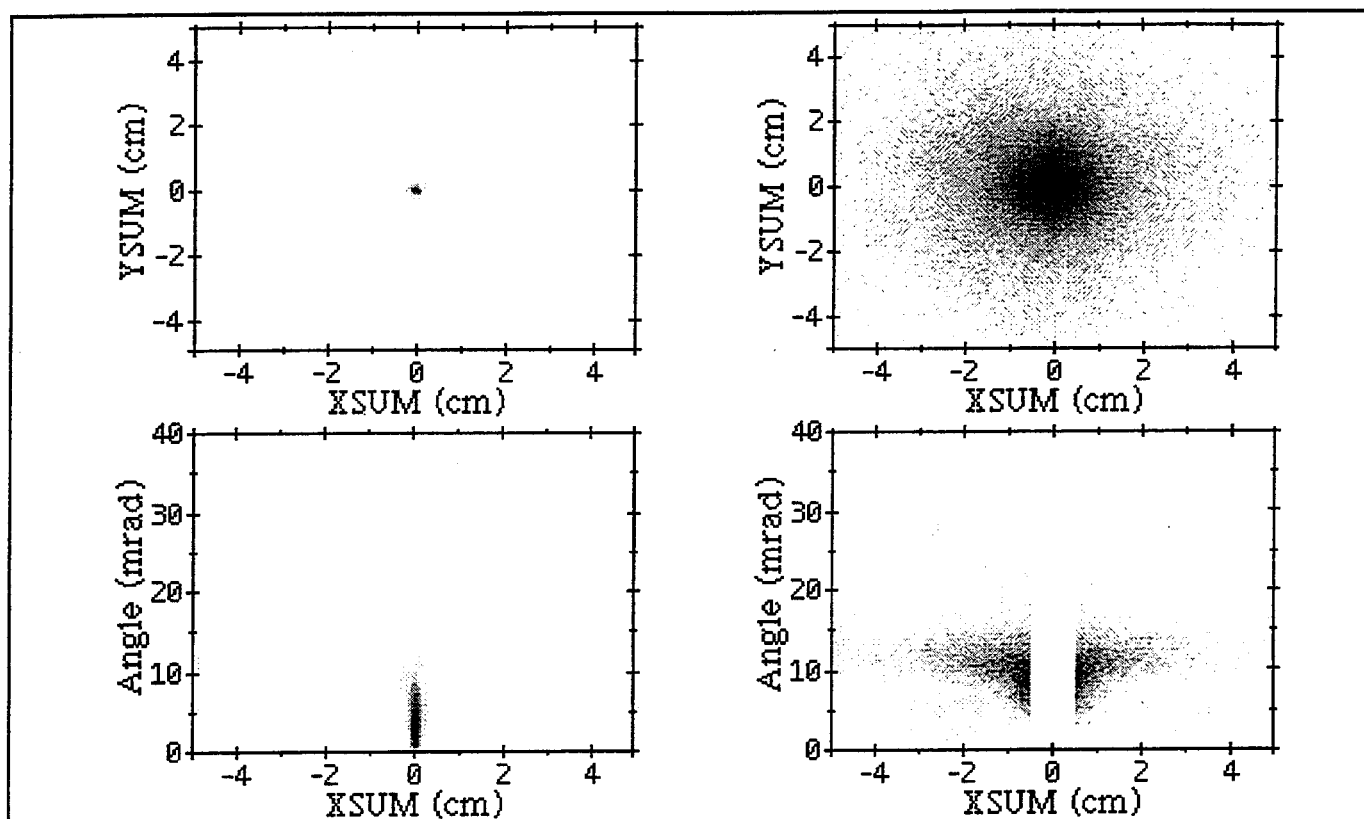


Fig. 11. Top left: two-dimensional histogram of XSUM vs. YSUM on a linear scale; top right on a logarithmic scale; bottom left: XSUM vs. scattering angle on a linear scale; bottom right: on a logarithmic scale with the additional restriction that both  $|XSUM|$  and  $|YSUM|$  be larger than 5 mm.

majority of events are not "problem" events. The upper right plot is the same data, but plotted on a logarithmic intensity scale to highlight the "problem" events. The bottom left plot shows on a linear intensity scale the proton scattering angle in the object as a function of XSUM and demonstrates that the lens also performs well over the relevant range of scattering angles. The bottom right plot shows the same distribution but on a logarithmic intensity scale and only for "problem" events. The "problem" or background events are defined as those that have both  $|XSUM| > 5$  mm and  $|YSUM| > 5$  mm. (This explains the missing events in the  $|XSUM| \leq 5$  mm region of the plot.) The information on background is more qualitatively given in the histograms shown in Fig. 12. The events shown are from a radiograph of the FTO, where only those events that at the object plane were within a horizontal band of  $\pm 5$  mm height centered on the FTO were used. It should be noted that the events considered passed all the way through to the imaging lens and to a trigger counter located behind the wire chambers at the image plane. (This explains the shape of the object plane distributions in Fig. 12, where the central air cavity and copper to tungsten transitions are evident.) The left column gives the X-distribution of those particles measured at the object plane, whereas the right column is for the same particles, but measured at the image plane. Each plot has two curves. The upper curve (darker) curve is for all events, whereas the lower (lighter) curve is for the background events as defined previously. There were several problems with the experimental setup which caused larger than expected backgrounds. One problem was inadequate shielding upstream of the object which allowed particles outside the "field of view" of the upstream lens to reach the object and image plane. Another problem was that the incident beam was by mistake not centered on the object; the majority of the beam actually missing the object and hitting the upstream magnets. The third problem was inadequate thickness for the collimator, which allowed some of the protons that hit the collimator to still reach the image plane. With the use of the wire chamber data, these types of events could be removed. This is shown in the lower two rows of histograms in Fig. 12. The measured "expected" background to signal values can be read off of the bottom row histograms and are on the order of a few percent. A more careful set-up would no doubt have improved these values.



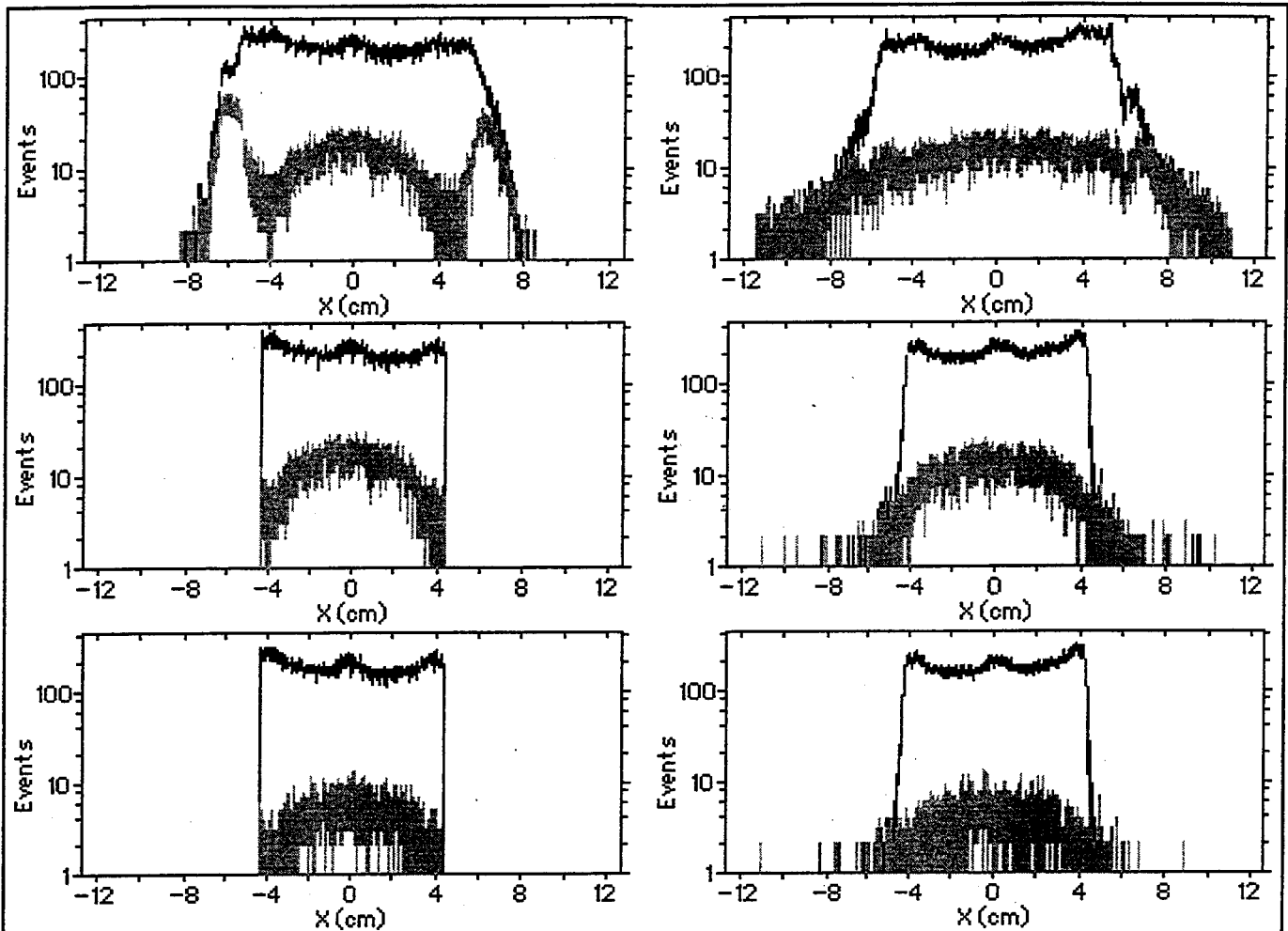


Fig. 12. Left: histograms of X positions at the object plane for events within a 1 cm high band in Y centered on the FTO at the object plane. Right: histograms of positions at the image plane. Top: all events. Middle: events required to be in the lens field of view at the object. Bottom: events also required to be within the collimator acceptance. The upper lines are the signal plus background. The lower lines are the background.

### AHF PROTON ACCELERATOR COMPLEX

The AHF will be required to produce transmission radiographic images with high spatial and temporal resolution. From 4 to 16 simultaneously-illuminated views and 25 or more time-separated exposures per view are desired. The desired beam-pulse structure needs to be flexible, with  $10^{10}$  to  $10^{11}$  protons in a 10-20 nsec-long pulse per view. A programmable time separation between pulses in each view which varies from a minimum of about 100 nsec to a maximum of many microseconds. These requirements lead to the use of a low-duty-factor, slowly cycling proton synchrotron with a flexible multipulse beam-extraction system, feeding into a multistage beam-splitting transport system that transmits proton pulses to the test facility.

The total number of protons in the ring is approximately  $10^{13}$ . This number follows from the following arguments. If we want pixel by pixel measurements that have an accuracy of 1 part in  $A$ , we need  $A^2$  particles per pixels from counting statistics arguments alone. Allowing for other measurement errors such as those associated with the detectors, we need to boost the number of particles by a factor of  $B$ . The beam is attenuated by the object by a factor of  $C$ , thus we need  $A^2BC$  particles per pixel in the incident beam. Taking into account the area of the object we need an additional factor  $D$  given by  $(\text{area of object}) / (\text{area of a pixel})$ . If we now have  $E$  views, assume losses in the beam splitting chain are a factor of  $F$  overall, and record  $G$  frames per view, the machine must deliver  $A^2BCDEFG$  protons in a shot. Going back to Table 1, and taking round number values, we have  $A \sim 100$ ,  $B \sim 2$ ,  $C \sim 5$  (the Gaussian shaped

Table 6. Twelve-View Beamline Summary	
Total splitter sections	4
Total straight cells	120
Total bend cells	232
Quadrupole Length (m)	704
bore radius (cm)	0.5
gradient (T/m)	2.5
Number of Dipoles	928
Dipole Length (m)	2.0
gap (cm)	5.0
field (T)	4.2

beam centered on the thickest part of the object helps here),  $D \sim (10 \text{ cm}/250 \text{ } \mu\text{m})^2 = 160,000$ ,  $E \sim 16$  (beam splitting in our design is in multiples of 2),  $F \sim 2$ , and  $G \sim 25$ , which approximately yields the  $10^{13}$  value.

The nominal beam energy of 50 GeV is set by object thickness and also by the thickness of the vessel (windows) that must contain the blast. The present study is based on an 800-MeV linac, such as available at LANSCE, which injects an  $\text{H}^-$  beam directly into a 50 GeV synchrotron. Numerous proton synchrotrons in the energy and/or intensity range needed for PRAD are presently in operation around the world. Thus the technology required for a PRAD accelerator has already been demonstrated. A conceptual point design for a system that can meet the above requirements has been presented elsewhere<sup>8</sup>. The synchrotron is fairly conventional, except for use of a lattice with an imaginary transition  $\gamma$  and certain features of the achromatic arcs.

There are two design parameters of a PRAD synchrotron that need some particular attention. First, simplicity of operation and low intensity suggests that a booster stage can be avoided. However, a critical parameter is the magnetic field at injection time. For a 50 GeV synchrotron operating at 1.7 Tesla at full energy, the magnetic field at injection time with 800 MeV injection is 0.05 Tesla. This is thought to be about the minimum practical field. Thus 50 GeV is the maximum practical energy for injection by the existing LANSCE linac at Los Alamos. For a higher energy PRAD synchrotron, either a booster synchrotron, or a higher energy injection linac would be required. (If constructed on a greenfield site, a lower energy linac plus a small booster would be a more cost-effective injector solution.)

The second issue concerns beam extraction from the high-energy synchrotron. If single-turn extraction is chosen, then a pulse train of length equal to the circumference of the synchrotron is delivered to the experiment. For a 1.5 km typical circumference of a 50 GeV synchrotron, this amounts to a total pulse train length of 5 microseconds. The bunch frequency in this train is the rf frequency of the synchrotron. We presently favor a 5 MHz rf frequency, thus providing bunch spacing of 200 ns. Loss-less extraction is possible if the kicker rise time is less than 200 ns, which is obtainable with today's technology.

If single-bunch extraction were to be installed, it would be possible to make a quite flexible program of pulse delivery that extends from spacing of 200 ns up to seconds. The total number of pulses available in the reference scheme would be 25 pulses. For this mode of operation, it is likely that a well-terminated single step kicker of 50 Ohm characteristic impedance would be used. For variable proton burst spacing, a modulator capable of providing 25 pulses with variable pulse spacing would have to be developed. Although no such modulator presently exists, it is believed that its development is not likely to present any obstacles to construction of the facility.

Both beam transport and beam splitting are performed in the beam transport system (see Fig. 13). The beamlines are achromatic and isochronous; the latter feature is enforced by symmetry. In the present example, there are 12 beamlines illuminating the target from different angles, both in-plane and out-of-plane. At the end of each beamline, there is a 45-m target-illuminating section that includes a diffuser and magnetic quadrupoles that prepare the beam size and convergence angles for object illumination. On the opposite side of the object containment chamber from each illuminating section, there are magnetic imaging

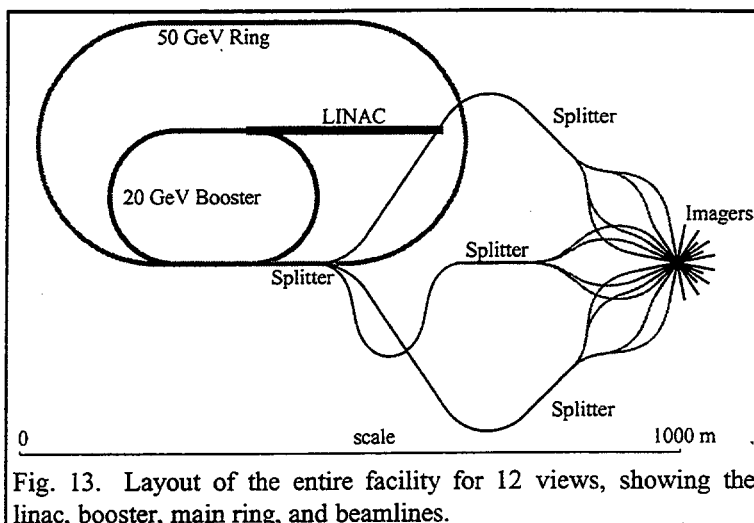


Fig. 13. Layout of the entire facility for 12 views, showing the linac, booster, main ring, and beamlines.

systems and detector arrays. The transport system parameters for the above design are listed in the Table 6 exclusive of the matching and imaging lenses.

## CONCLUSION

We have reviewed the basic concept of proton radiography and found that it should perform extremely well and have substantial advantages of x-ray based radiography in the case of thick ( $100\text{'s g/cm}^2$ ) objects. In the case of thin objects, it still performs very well, with added bonus that it can be tuned to give high contrast images regardless of how thin the object is. An added feature of proton radiography is the ability to measure, not only the amount of material (as in standard radiography), but also the composition of the radiographed object in terms of material identities. These predictions have been confirmed in beam tests. The proton accelerator needed for a future Advanced Hydrotest Facility is not beyond the scope of existing proton accelerators. Furthermore proton accelerators naturally have the strobed pulse nature needed to follow rapidly evolving dynamic events and can do so for an extended period of time.

---

<sup>1</sup> InterScience, Inc., "Technology Review of Advanced Hydrodynamic Radiography", March 6-7, 1996, ISI-TM96050701.93.

<sup>2</sup> H.-J. Ziock et al., "Detector Development for Dynamic Proton Radiography", these proceedings.

<sup>3</sup> J. Miyahara et al., "A New Type Of X-Ray Area Detector Utilizing Laser Stimulated Luminescence", Nucl. Instr. and Meth., **A246** (1986) 572.

<sup>4</sup> Particle Data Group, "Review of Particle Physics", Phys. Rev. **D54**, (1996).

<sup>5</sup> C.T. Mottershead and J. D. Zumbro, "Magnetic Optics for Proton Radiography", Proceedings of the 1997 Particle Accelerator Conference, Vancouver, B. C., Canada (to be published).

<sup>6</sup> R. E. Prael, H. Lichtenstein, et. al., "User Guide to LCS: The LAHET Code System", LA-UR-3014, (1989). For more information see <http://www-xdiv.lanl.gov/XCI/PROJECTS/LCS/> or contact R. Prael (505)667-7283.

<sup>7</sup> A. Fasso, A. Ferrari, J. Ranft, P.R. Sala, G. R. Stevenson, J.M. Zazula, "A Comparison of FLUKA Simulations with Measurements of Fluence and Dose in Calorimeter Structures", Nucl. Instr. and Meth. , **A332** (1993) 459.

<sup>8</sup> F. A. Neri, H. A. Thiessen, and P. L. Walstrom, "Synchrotrons and Beamlines for Proton Radiography", Proceedings of the 1997 Particle Accelerator Conference, Vancouver, B. C., Canada (to be published).



# Overview of Radiation Hardness of Silicon Detectors for HE Physics\*

B. Dezillie and Z. Li

Brookhaven National Laboratory, Upton, NY 11973-5000

\*This investigation was done as a part of work established and supported by the Rose Collaboration (RD48, CERN), and was supported in part by the U.S. Department of Energy: Contract No: DE-AC02-98CH10886.

## Abstract

The status of the on-going work in radiation damage and hardness of silicon detectors for high-energy physics experiments is summarized. Recent progress in defect engineering for rad-hard silicon detectors, including low (FZ and CZ) and medium (FZ) starting resistivity silicon, Epi-Si (medium and high resistivities), and non-standard processing (as compared to standard planar processing), will be presented. The results are reported in terms of reverse current, depletion voltage as a function of fluence and annealing time after irradiation.

## 1. Introduction

Recently tremendous interests have been generated towards the usage of non-standard silicon materials and processing steps for detectors in extreme radiation environment (i.e. LHC). Some of more promising approaches are: 1) usage of medium ( $\sim 1 \text{ k}\Omega\text{cm}$ ) and low ( $\leq 500 \text{ }\Omega\text{cm}$ ) resistivity n-type silicon as starting material; 2) usage of epitaxial silicon materials; 3) incorporation of impurities in silicon materials during growth and/or during detector processing to getter radiation-induced defects that cause detector degradation; and 4) non-standard detectors processing steps as opposed to the usual planar processing technology. In this paper, the effect of starting resistivity, growth parameters, Epi-Si, and processing parameters on the detector electrical properties, in particular on the effective impurity concentration ( $N_{\text{eff}}$ ), will be summarized and systematically presented.

## 2. Experimental conditions

### 2.1 Test structures

The first set of epitaxial (Epi) n-type wafers, with thickness ( $d$ ) of 100 and 150  $\mu\text{m}$ , was made on 300  $\mu\text{m}$  thick CZ substrates by MACOM (USA). Canberra (Belgium) has processed all MACOM epitaxial samples with the planar technology. Samples labelled C50  $\rightarrow$  C83 are single round diode areas varying from 0.08 to 2.19  $\text{cm}^2$  [1, 2]. Samples labelled C142-C-A1/A3/B3-# were processed using the CERN II mask design with various structures (pads, strips, pixels).

The second set of Epi-Si wafers (n- and p-type with different thickness: 100, 150 and 200  $\mu\text{m}$ ) was grown on 600  $\mu\text{m}$  CZ substrates by ITME (Poland) [3]. Most wafers in this set were grown at a growing rate of 1  $\mu\text{m}/\text{min}$ . Some wafers in the set (thickness = 100  $\mu\text{m}$ ) were grown at a growing rate of 0.5  $\mu\text{m}/\text{min}$  to check the effect of growing rate on radiation hardness. Some wafers in this second set have been processed by the MESA technology by DIOTEC (Slovakia Republic) [4] and cut to single diode test

structures of  $0.25 \text{ cm}^2$ . Some other wafers in the second set were processed by Canberra with the traditional planar technology using the CERN II mask set.

Float-Zone (FZ) silicon detectors with different resistivities have been manufactured by Wacker and processed at BNL, using the standard BNL mask set for test diodes.

Czochralski (CZ) silicon wafers with an initial resistivity of  $100 \Omega \text{ cm}$  have been manufactured by Polovodice (Czech Republic) and processed at BNL.

Parameters of Epi-Si samples studied here are listed in Table I and II. Table III gives the parameters, as well as radiation fluences, of Epi, FZ, and CZ silicon samples for the study of the initial resistivity effect on radiation hardness of detectors.

**Table I Initial characteristics and names for n-type epitaxial samples (Conduction: n-type)**

Manufacturer	Producer	Epitaxial thickness ( $\mu\text{m}$ )	Resistivities [ $\Omega\text{cm}$ ]	Substrate thickness ( $\mu\text{m}$ )	Naming convention
MACOM	Canberra	120	960	300	C50
		110	500 - 860	300	C52 $\rightarrow$ C72
		100	600 - 800	300	C73 $\rightarrow$ C83
		100	800	300	C142-C-B3-1 $\rightarrow$ 20
		100	800	200	C143-C-B3-1 $\rightarrow$ 20
		150	2000	300	C144-C-A3/B3-1#
		150	2000	300	C145-C-B3-1 $\rightarrow$ 20
		150	2000	300	C146-C-#
ITME	Canberra	105	$\sim 2200$	600	I3-C-B3-1 $\rightarrow$ 10
		90	$\sim 4000$	600	I14-C-B3-1 $\rightarrow$ 10
		150	$\sim 10.000$	600	I23-C-B3-1 $\rightarrow$ 10
		185	$\sim 12.500$	600	I33-C-B3-1 $\rightarrow$ 10
ITME	DIOTEC	105	1800 - 4200	600	I1 $\rightarrow$ 9-B-1 $\rightarrow$ 30
		90	6000 - 7250	600	I11 $\rightarrow$ 19-B-1 $\rightarrow$ 30
		150	5500 - 7450	600	I21 $\rightarrow$ 29-B-1 $\rightarrow$ 30
		185	2800 - 3600	600	I31 $\rightarrow$ 39-B-1 $\rightarrow$ 30

**Table II Initial characteristics and names for p-type epitaxial samples (Conduction: p-type)**

Manufacturer	Producer	Epitaxial thickness ( $\mu\text{m}$ )	Resistivities [ $\Omega\text{cm}$ ]	Substrate thickness ( $\mu\text{m}$ )	Naming convention
ITME	DIOTEC	105	390 - 520	600	I1P $\rightarrow$ 9P-B-#
		93	1300 - 3250	600	I11P $\rightarrow$ 19P-B-#
		142	1700	600	I21P $\rightarrow$ 29P-B-#
		200	3250 - 4500	600	I31P $\rightarrow$ 39P-B-#

**Table III The characteristics of samples used in the study of the effects of the initial resistivity on the radiation hardness**

Wafer number	Type	Initial resistivity ( $\Omega\text{cm}$ )	Thickness ( $\mu\text{m}$ )	$V_{\text{fd},0}$ (V)	Fluence ( $\text{n/cm}^2$ )
796	CZ	100	325	2700	$7 \times 10^{14}$
795	FZ	500	265	650	$7 \times 10^{14}$
C143	Epi	630	100	50	$4 \times 10^{14}$
C153	Epi	2k	150	36	$4 \times 10^{14}$
799	FZ	5k	400	90	$7 \times 10^{14}$

## 2.2 Irradiation facilities

Proton irradiation has been performed at the Proton Synchrotron (PS) at CERN. The beam energy was 24 GeV (hardness factor =  $0.5 * (1 \text{ MeV neutron})$  [ROSE]). The average flux during an entire irradiation was approximately  $3 \times 10^9 \text{ cm}^{-2} \text{ s}^{-1}$ . Detectors were irradiated in fluence steps up to a maximum fluence of  $4 \times 10^{14} \text{ cm}^{-2}$ . Measurements have been taken after each fluence step. Irradiation with 7 to 10 fluence steps usually took around 3 days. The irradiation temperature was 26 °C and measurement and storage temperature was 20 °C.

1 MeV neutron irradiation has been performed within a 24-hour period at the University of Massachusetts at Lowell (USA) and some additional samples were irradiated by 10 MeV neutrons at PTB (Germany).

## 2.3 Characterisation techniques

Electrical characteristics of samples were obtained from the current-voltage (I-V) and capacitance-voltage (C-V) measurements using a Keithley 487 High Voltage Source Measuring Unit and a Hewlett Packard 4263A Impedance Analyser operating at 10 or 100 kHz. The full depletion voltage ( $V_{\text{fd}}$ ), normalised to a 300  $\mu\text{m}$  diode thickness, is deduced from the C-V curve. The leakage current was obtained from the I-V curve at full depletion. All data presented in this paper have been corrected for self-annealing and normalised to 20°C following [5].

After irradiation, the first annealing measurement has been performed after 10 days of room temperature annealing. Then the detectors were heated in several steps for 1-3 h at 80°C, in order to accelerate the annealing process. The annealing time is then expressed in equivalent room temperature time.

## 2. Results and discussions

### 2.1 The effect of material growing and processing

Growth rates were varied to see if this altered the oxygen and carbon concentrations in the epitaxial layer. Based on some defect kinetic modelling [6], higher oxygen and carbon concentrations were predicted to lead to a more radiation hard material.

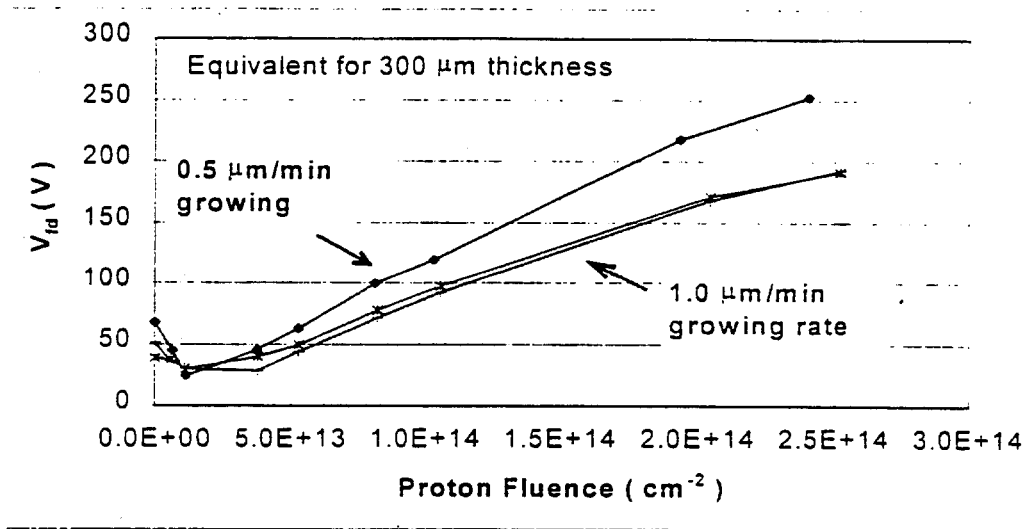


Figure 1: The full depletion voltage ( $V_{fd}$ ) as a function of proton fluence for ITME Epitaxial detectors with different growing rates (0.5 and 1  $\mu\text{m/min}$ )

Figure 1 shows  $V_{fd}$  as a function of proton fluence for two ITME detectors of 100 and 150  $\mu\text{m}$  thick with a growing rate of 1  $\mu\text{m/min}$ , one ITME detector of 100  $\mu\text{m}$  thick with a growing rate of 0.5  $\mu\text{m/min}$ . It is clear that the rate of increase with fluence ( $\Phi$ ) for detectors with higher growing rate is much smaller than that for detectors with lower growing rate. This may be explained by gettering/sinking effect of irradiation-induced defects by thermal defects. During the growth with a higher growing rate, more defects are likely to form in the material. More defects in the starting material lead again to a more radiation hard material due to possible gettering/sinking effect of radiation induced defects by as-grown defects [7, 8]. However, there was now clear correlation between the oxygen and carbon impurities (measured by SIMS (Secondary Ion Mass Technology) by EVANS Europe) and the radiation hardness of the detectors. The diffusion of defects during the growing process is nearly identical for 100 and 150  $\mu\text{m}$  thick epitaxial layers.

Figure 2 illustrates the volume leakage current as a function of proton fluence for ITME diodes with different growing rate and one MACOM detector of 150  $\mu\text{m}$  thick [2]. All these detectors have been processed in identical conditions by ion-implantation by Canberra. Coherent with the result of the full depletion behaviour after the irradiation (Fig. 1), the leakage current is higher for ITME detectors grown with a lower growing rate. The alpha value for the MACOM sample is much lower than the alpha value for the ITME samples. However, no details about the MACOM growing procedure are known. Nevertheless there exists a clear difference the two manufacturers, indicating strong processing dependence.



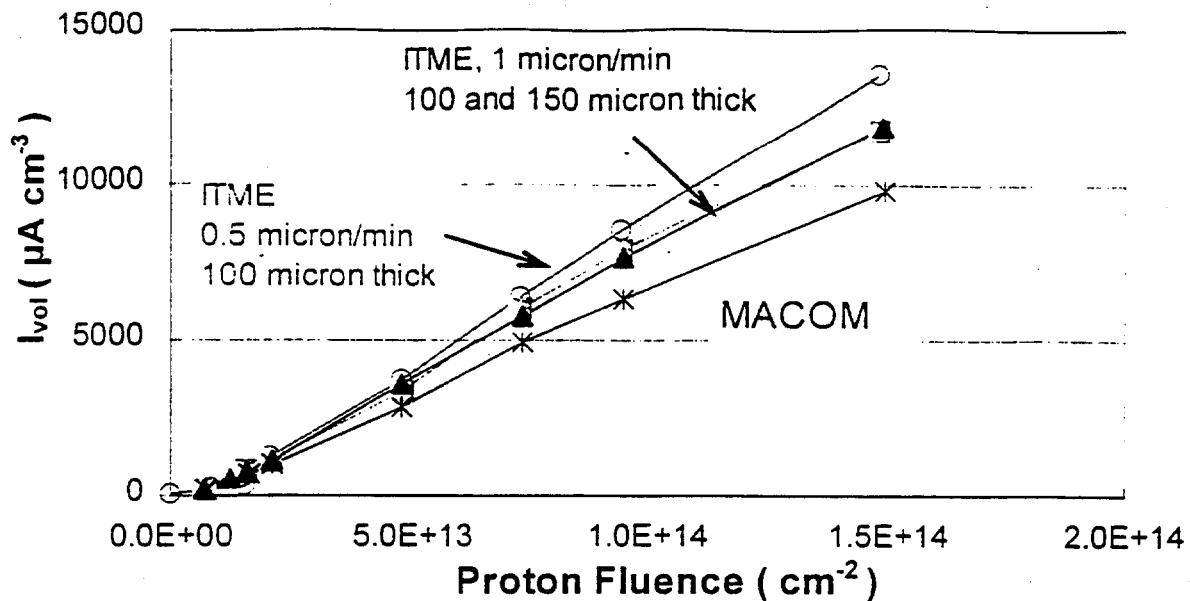


Figure 2: The leakage current as a function of proton fluence for ITME diodes with different growing rates and one MACOM diode, all processed by ion-implantation.

Figure 3 shows the SIMS results (measured by EVANS Europe) for a processed MACOM and an unprocessed ITME detector. The oxygen concentrations are identical for both (in the order of  $5 \times 10^{16}/\text{cm}^3$ ), but the carbon concentration for the more radiation hard MACOM sample is three times lower than the ITME sample. This result indicates that high carbon concentration – in contrast to what the modelling predicts - have a negative influence on the radiation hardness.

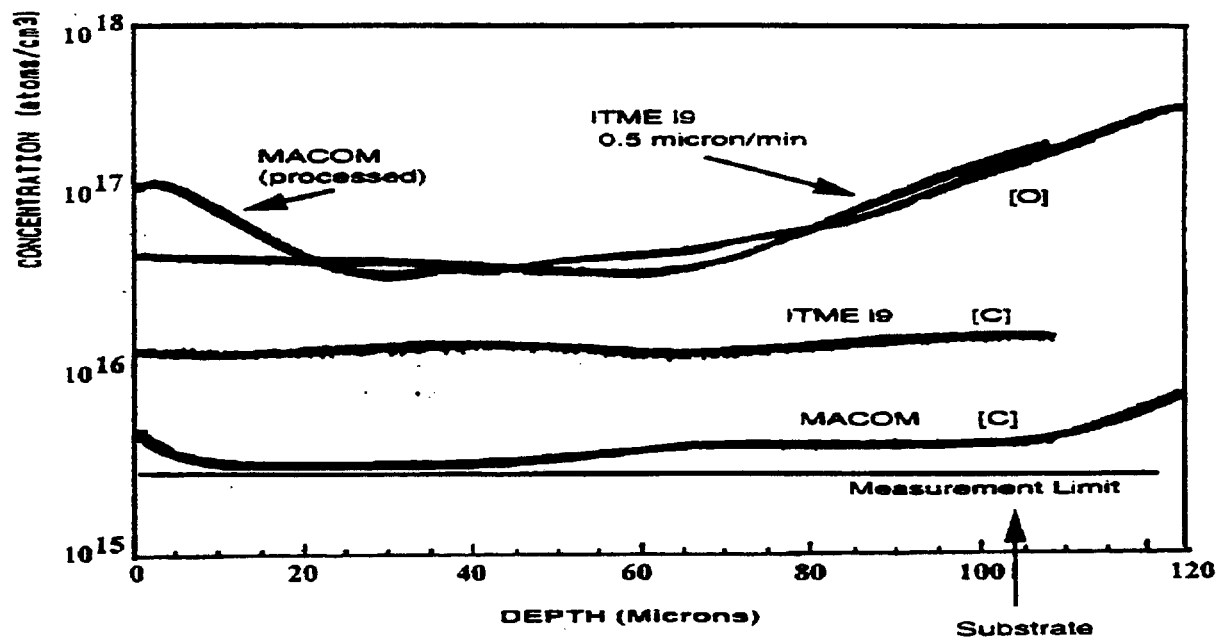


Figure 3: SIMS analysis of a processed MACOM and unprocessed epitaxial wafer.

The structure and orientation of the crystal lattice could also play a role in the defect kinetics and the radiation hardness of the material. It is known that MACOM changed the crystal orientation from  $\langle 111 \rangle$  to  $\langle 100 \rangle$ . Detectors with  $\langle 111 \rangle$  crystal orientation are more radiation hard than those with  $\langle 100 \rangle$  crystal orientation. But the direct influence of crystal orientation on the radiation hardness is not clear since detectors grown with the  $\langle 100 \rangle$  orientation have also higher initial resistivity, which, as we will describe in the following section, would also have strong effects.

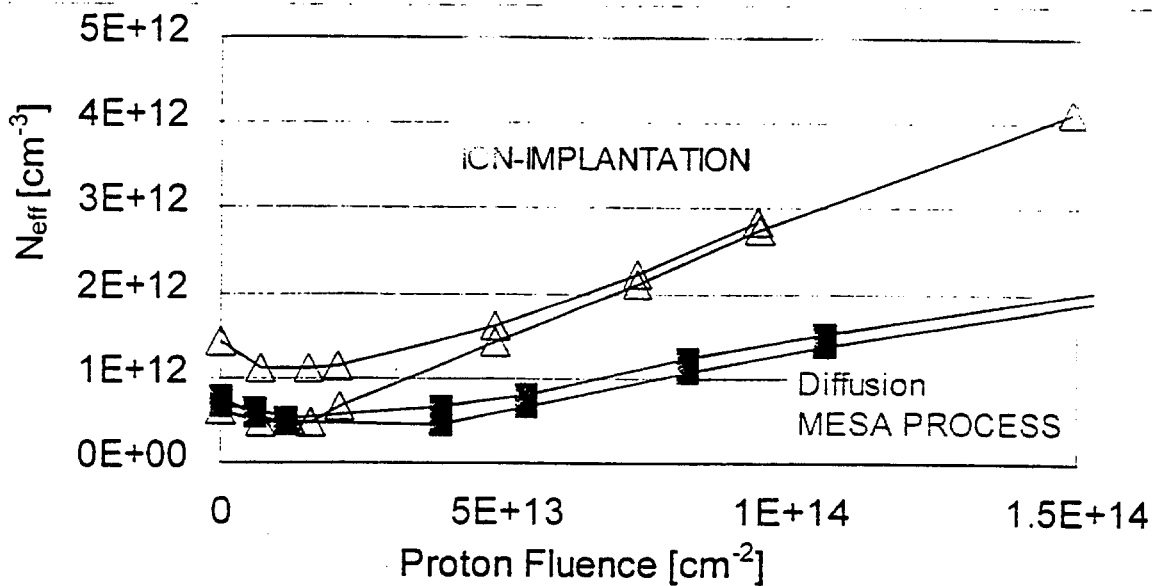


Figure 4: The effective impurity concentration as a function of proton fluence for MESA and Planar processed diodes from the same material.

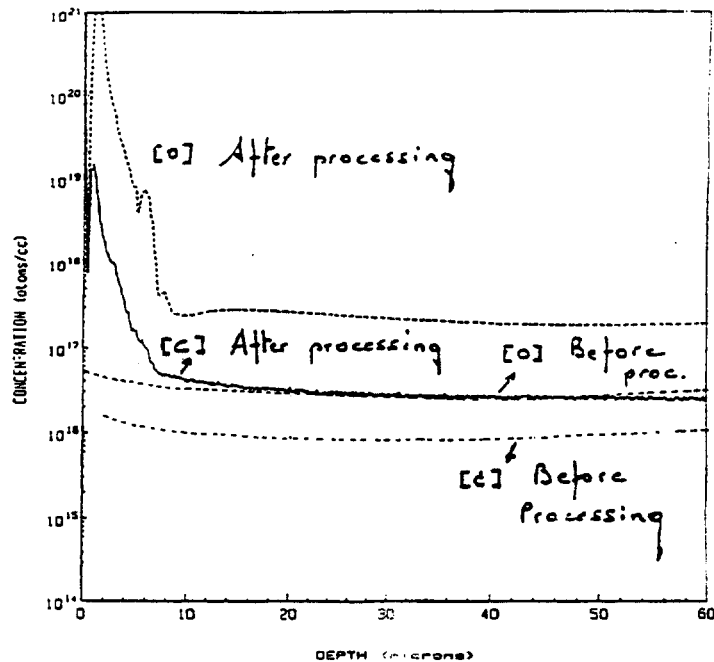


Figure 5: SIMS measurements by EVANS Europe. Depth profiles for an ITME, 100 mm thick (1  $\mu\text{m}/\text{min}$  growing rate), n-type epitaxial material. A large increase of [O] and [C] is observed.

As shown in Fig. 4, epitaxial as well as FZ diodes processed with MESA method are twice as radiation hard as those processed by planar technology. SIMS measurements show a huge increase of oxygen and carbon concentration after the MESA processing, as shown in Fig. 5. We should note here that, MESA method could also introduce other impurities as well as defects in detectors during processing, since it is a highly invasive technology [4]. However, the strong influence of processing-induced impurities/defects on the radiation hardness is once more observed.

Some epitaxial diode have also been irradiated under a constant bias (150 volts) [2], which was set to be larger than  $V_{fd}$  at anytime during irradiation. No difference in alpha and beta ( $\beta$ ) values between biased and non-biased epitaxial detector has been observed (e.g. Fig 6 shows  $V_{fd}$  vs. fluence). During the annealing process after irradiation, the biased detector was held continuously at the same bias voltage (even during the heating period to accelerate the annealing process). Figure 7 gives the alpha evolution as a function of equivalent time at room temperature (RT). Again, no effect of the bias has been observed during the annealing process of both alpha and beta values.

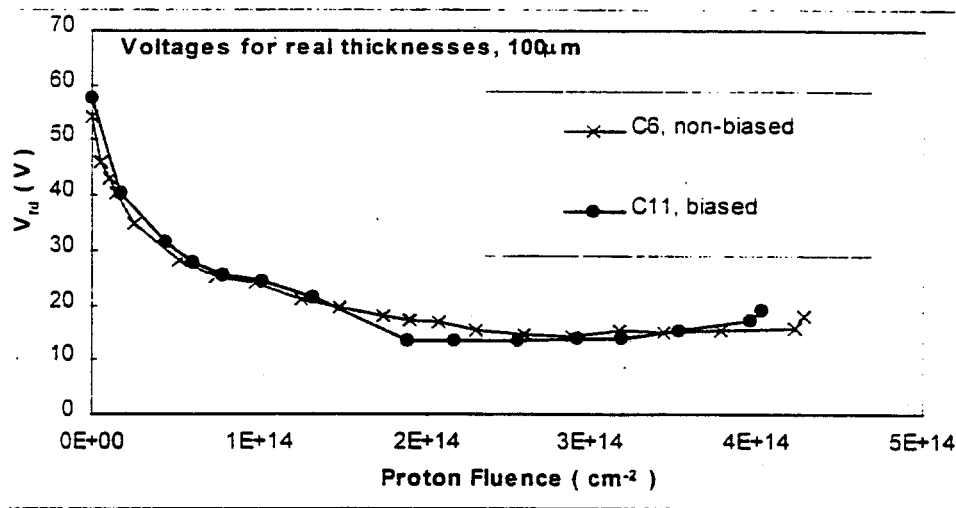


Figure 6: The full depletion voltage for real diode thickness (100  $\mu\text{m}$ ) as a function of proton fluence for MACOM epitaxial detectors.

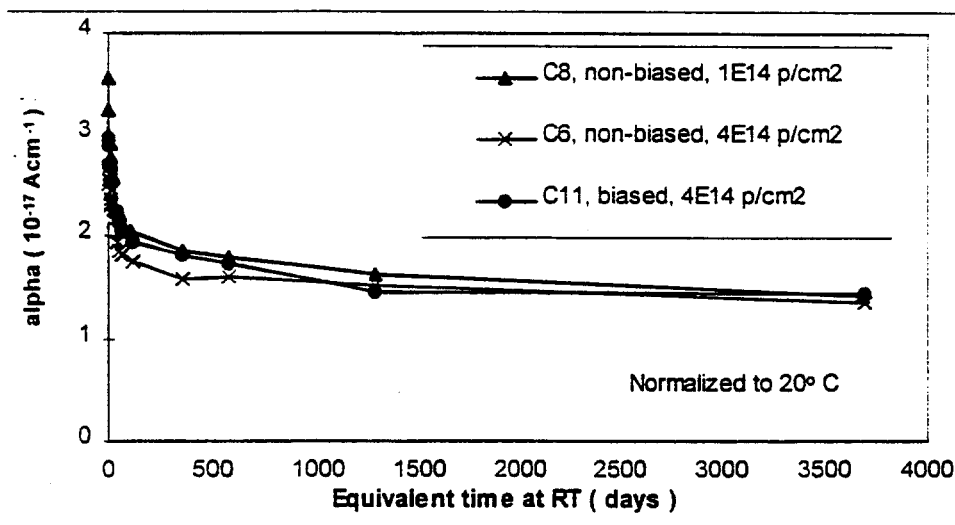


Figure 7: The damage constant alpha versus equivalent time at RT for biased and non-biased MACOM epitaxial detectors.

Table IV gives an overview of alpha and beta values for detectors made with the different epitaxial materials and processes.

The alpha factor is determined as:  $\alpha = \Delta I_{vol} / \Phi$ . The beta factor is calculated from the equation:  $N_{eff}(\Phi) = |N_{D,0} e^{-c\Phi} - N_{A,0} - \beta\Phi|$ , with  $N_{A,0}$  the initial acceptor concentration,  $N_{D,0}$  the initial donor concentration and  $c$  the removal rate of donors.

Table IV: Overview of the alpha and beta values for different Epitaxial detectors.

Manufacturer	Device	$\alpha$ ( $10^{-17} \text{ A cm}^{-1}$ )	$\beta$ ( $10^{-3} \text{ cm}^{-1}$ )	$\phi_{inv}$ ( $\text{p/cm}^2$ )	$N_{eff,0}$ ( $\text{cm}^{-3}$ )	$\rho_o$ ( $\text{Ohm cm}$ )
N-TYPE MACOM Epi	C50	4	-	2.0E+15	4.6E+13	940
	C78	5.7	7.48	2.0E+15	6.8E+13	740
	C142-C-6	4.4	1.1	2.5E+15	7.2E+13	580
	C142-C-8 (Biased)	4.4	1.1	2.5E+15	7.2E+13	580
	C144-C-A3-20	6.87	1.37	~2.1E13	2.0E+13	2100
ITME Epi	I1-B-2 (0.5 $\mu\text{m/min}$ )	5.33	15	1.1E+14	9.9E+12	4200
	I11-B-2	4.16	10.4	1.2E+14	5.7E+12	7250
	I21-B-2	4.24	10.9	1.4E+14	7.5E+12	5500
	I31-B-2	4.88	-	2.7E+14	1.5E+13	2800
	I2-C-20 (0.5 $\mu\text{m/min}$ )	9.68	> 40	~2.0E+13	1.1E+13	3800
	I12-C-20	8.39	~ 27	~2.0E+13	1.9E+13	2230
	I22-C-20	8.36	27	~2.0E+13	5.8E+12	7150
	I32-C-20		38.6		3.3E+12	12650
Wacker FZ	M18	7.2	28	2.4E+13	4.0E+12	11500
	M160	5.4	18.9	1.1E+14	6.9E+12	6000
P-TYPE ITME Epi	I1P-B-1 (0.5 $\mu\text{m/min}$ )	-	-		3.2E+14	390
	I11P-B-2	4.7	9.3		9.1E+13	1400
	I21P-B-2	4.9	9.6		7.3E+13	1700
	I31P-B-2	-	10.2		2.4E+15	3450
Wacker FZ	CP	5.8	13.2		2.4E+12	5800

Interesting as well is the behaviour of the p-type ITME epitaxial detectors. Figure 8 shows  $V_{fd}$  vs. proton fluence for 100, 150 and 200  $\mu\text{m}$  thick p-type epitaxial detectors. Surprisingly, in contrast to results from the standard high resistivity FZ p-type detectors [9], we have observed an initial decrease of  $V_{fd}$ , similar to the donor removal/compensation effect observed in n-type detectors. One almost has to assume a radiation-induced "acceptor removal" to explain this effect. However, a new model base on the interaction of two deep levels predicts such behaviour in p-type silicon detectors [10]. We should note that this process is still not totally understood yet. The beta factor for these three p-type epitaxial diodes is nearly identical (see Table IV).

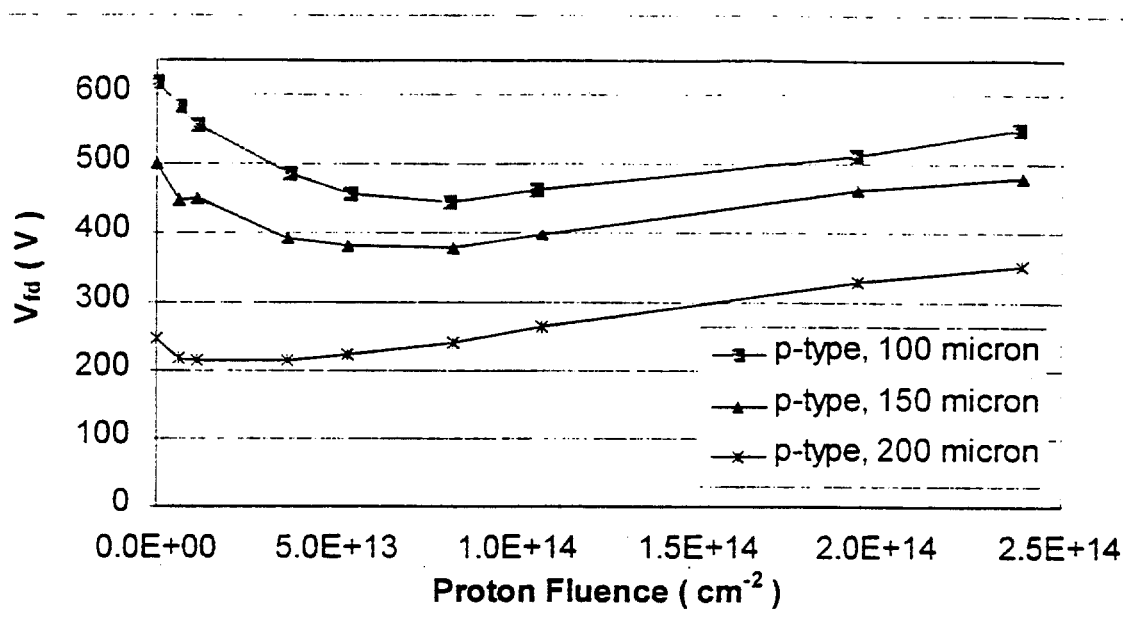


Figure 8: The full depletion as a function of proton fluence for p-type ITME Epitaxial detectors.

### 1.2 The effect of the initial resistivity

Comparing the behaviour of low and high resistivity MACOM epitaxial diodes, it has been observed that the low resistivity detectors are more radiation hard. In general, differences in initial doping concentration as well as differences in crystal orientation and growing conditions could cause these differences in radiation hardness. It is well known now that lower initial resistivity material inverts at a higher fluence, with inversion fluence nearly proportional inversely to the initial resistivity. The donor removal rate is much lower than previously thought if it exists at all. Higher initial donor concentration helps to provide positive space charge to compensate the radiation-induced negative space charge due to deep acceptors.

In order to fully understand the effect of initial resistivity on the detector radiation hardness, some low resistivity CZ and FZ diodes (see Table III) have been irradiated and heated for the study of  $N_{eff}$  (effective impurity or space charge concentration,  $N_{eff} = 2\epsilon\epsilon_0 V_{fd}/ed^2$ ) behaviour as a function of fluence and time [11]. Figure 9 illustrates  $V_{fd}$  as a function of neutron fluence for 630  $\Omega\text{ cm}$  Epi, 2  $\text{k}\Omega\text{ cm}$  Epi, and a 5  $\text{k}\Omega\text{ cm}$  FZ. The inversion fluence is nearly the same for FZ and epitaxial diodes with similar initial resistivities ( $\rho_0$ ). However, at higher fluences ( $> 4 \cdot 10^{14} \text{ n/cm}^2$ ), the increasing rate of  $N_{eff}$  is somewhat lower for epitaxial detectors than that for FZ detectors with similar  $\rho_0$ ,

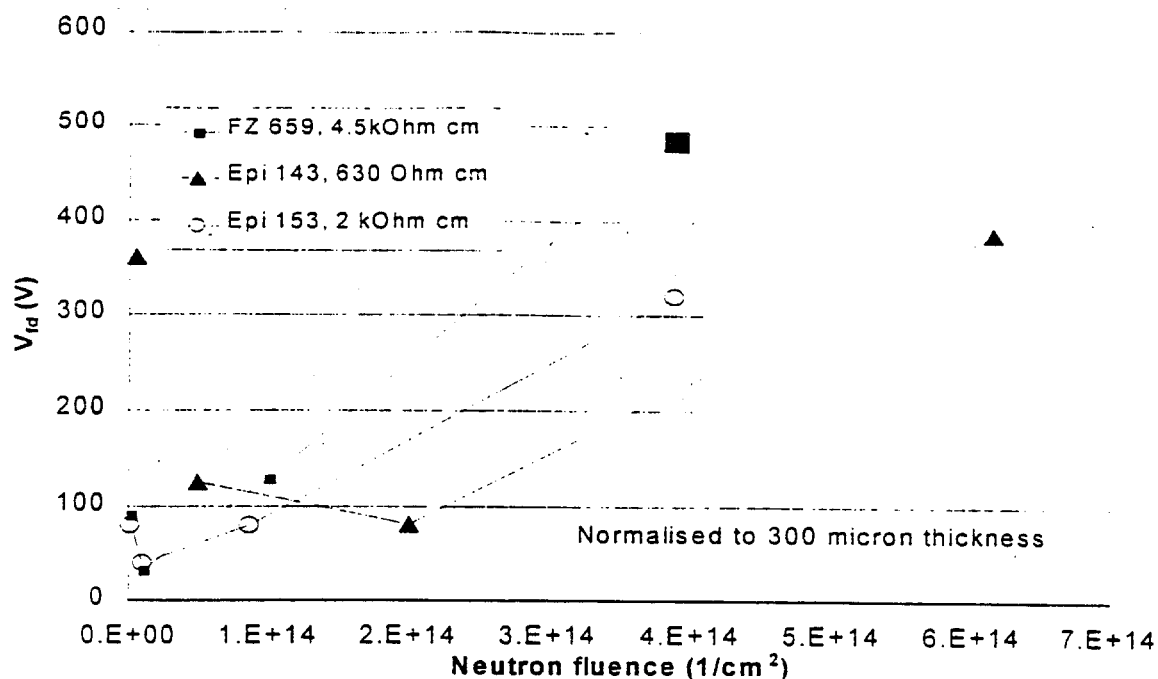


Figure 9: The effective doping concentration as a function of neutron fluence, for CZ, FZ and EPI detectors with different initial resistivities.

indicating that there may be increased radiation hardness for Epi-Si due to its processing. For both FZ and Epi detectors, the overall  $N_{eff}$  after 10 years reverse annealing at equivalent room temperature is higher for detectors made with larger initial resistivities silicon materials [12]. This behaviour is consistent with the compensation model of deep acceptors in which the "donor removal" plays no role [13].

## Acknowledgements

The authors would like to thank Prof. G. Lindström and M. Moll from Hamburg for performing neutron irradiation on some samples used in this study. Some detector data have been taken during the collaboration with the CERN ECP/MIC group. In particular, one of the authors, Dezillie, would like to thank F. Lemeilléur for his supervision. Also the work of the CERN group in preparing the proton irradiation's at the PST7 is greatly appreciated.

## References

- [1] B. Dezillie et al., "Experimental results on radiation-induced bulk damage effects in float-zone and epitaxial silicon detectors", Nucl. Instr. and Meth. A **386** (1997) 162-166.
- [2] B. Dezillie, PhD thesis, "Radiation hardness studies of epitaxial silicon particle detectors for applications at the CERN LHC" Sept. 1997.
- [3] E. Nossarzewska, "ITME epitaxial manufacturing", Presented at the 2<sup>nd</sup> ROSE Workshop on Radiation Hardening, CERN, Feb. 1997.
- [4] B. Sopko, "Silicon Processing at Polovodice", Presented at the 2<sup>nd</sup> ROSE Workshop on Radiation Hardening, CERN, Feb. 1997.
- [5] G. Lindström, "Radiation damage in silicon detectors – Self annealing corrections – Normalisation to  $t = 20^\circ\text{C}$ ", SITP-Internal Note, SITP-002, 1991.

- [6] B.C. MacEvoy. "Defect kinetics in silicon detector material for applications at the Large Hadron Collider", Ph.D. Thesis RAL-TH-003. 1997.
- [7] Z. Li et al.. "Investigation of silicon layers as a material for radiation hardening silicon detectors BNL-64973. Presented at the IEEE NSS. Albuquerque Nov. 9-15 1997, accepted by IEEE Trans. Nucl. Sci., June (1998), in press.
- [8] S.J. Watts. "Irradiation induced defects in silicon detectors". Invited paper presented at the 192 Meeting of the Electrochemical Society, Inc., Paris. Aug. 31 – Sept. 5, 1997.
- [9] F. Lemeilleur et al.. "Electrical properties and charge collection efficiency for neutron-irradiated p-type and n-type silicon detectors", Nucl. Physics B 32 (1993), p. 415-424.
- [10] K. Zankel and H. Kosina. "The role of trap Coupling in irradiated Silicon Detectors", presented at the 3<sup>rd</sup> ROSE Workshop on Radiation Hardening of Silicon Detectors. Hamburg, 12-14 Feb., 1998. Copy of transparencies in DESY-Proceedings-1998-02.
- [11] B. Dezillie et al., "Defect analysis of silicon detectors made of different materials for radiation hardness", proceedings of the 2<sup>nd</sup> International Conference on Radiation Effects on Semiconductor Materials, Detectors and Devices. Florence, Italy, March 4-6, 1998, to be published in Nucl. Instr. and Meth. A.
- [12] B. Dezillie et al.. "Diode and Resistor Studies on Neutron Irradiated Silicon Samples with Different Starting Resistivities", to be present at the IEEE Medical Imaging Conference, Toronto, Canada. Nov 12-14, 1998.
- [13] Z. Li et al.. "Simulation and Design of Various Configurations of Silicon Detectors for High Irradiated Tolerance up to  $6 \times 10^{14}$  n/cm<sup>2</sup> in LHC Application", BNL-64488, Presented at the Pisa Meeting on Advanced Detectors. Elba, Italy, 25-31 May (1997), sub. Nucl. Instrum. and Meth., in press.





# PIXEL SENSORS FOR ATLAS

Sally Seidel  
Department of Physics and Astronomy  
University of New Mexico  
Albuquerque, New Mexico 87131, USA

for the ATLAS Collaboration

8 May 1998

## Abstract

The design and fabrication of the First Prototype Pixel Sensors for ATLAS has been completed. The wafers include two large rectangular structures, called tiles, as well as numerous smaller structures. Each tile accepts 16 readout chips and is compatible with the prototype module design. Most of the smaller structures are compatible with single readout chips. The designs of all of these prototype devices are explained with attention to the goals and constraints that guided design choices.

## 1 OVERVIEW OF THE ATLAS PIXEL SENSOR PROGRAM

The ATLAS Experiment at the CERN LHC will include a silicon pixel detector as its innermost tracking chamber. The detector will consist of three layers of rectangular sensors arranged in a cylindrical ("barrel") pattern

coaxial with the beamline, and  $2 \times 5$  layers of identical sensors assembled into disks. The detector will require 1508 barrel sensors and 720 disk sensors.

The pixel detector must survive for 10 years in the hostile radiation environment of the collider. The sensors closest to the beam will receive more than  $10^{15}$  minimum ionizing particles/cm<sup>2</sup>. The anticipated need to operate the sensors partially depleted after some point in their radiation lifetime is the dominant factor in the choice of  $n$ -type implants in  $n$ -type substrate. As radiation damage to the bulk will require increasingly higher operating voltages during the detector's lifetime, the requirement of operating these sensors at high voltage without electrical breakdown or microdischarge is important to the design. Some features of the design also reflect the desire to provide bias to every pixel without attaching the readout integrated circuit. This is expected to facilitate testing of the sensors prior to bonding and to guarantee a uniform electric field in the sensor active area in cases of failure of a bump bond. To minimize multiple scattering of tracks in this, the innermost of ATLAS's detection systems, the inner layer will be fabricated from sensors of  $200\mu\text{m}$  thickness while the outer two layers and the disks will use  $250\mu\text{m}$  sensors.

The production sensors for the ATLAS barrels will be 2 readout chips wide and 8 readout chips long. The readout chips will have 24 columns and 160 rows; each pixel cell will have dimensions  $50 \times 300\mu\text{m}^2$ . Consequently, the active area for a barrel sensor will be  $16.4 \times 60.4 \text{ mm}^2$ . The overall dimensions of the barrel sensor depend upon the module concept (still in development) but will lie in the range  $16.4 \times 62.4 \text{ mm}^2$  to  $21.4 \times 67.8 \text{ mm}^2$ . Disk sensors will use the same technology as barrel sensors but will have a slightly different shape.[1]

The ATLAS pixel sensor design program includes fabrication of First Prototypes and Second Prototypes prior to production sensors. First Prototypes were designed in 1997, fabricated by CiS Institut für Mikrosensorik e.V. and Seiko Instruments Inc., and are now under study within ATLAS. The Second Prototypes are expected to be designed and ordered prior to January 1, 1999. Pre-production sensors will be designed and ordered in 1999 so that production sensors can be ready for assembly in 2000.

This document primarily concerns the First Prototypes. The First Prototype wafers contain 2 large structures, called Tile 1[1] and Tile 2[1, 2], 17 smaller sensors which examine additional design options and which can

each be read out by a single amplifier chip, and a variety of process test structures. Design details of the two tiles and important features of some of the other structures are described below.

## 2 THE DESIGN OF THE FIRST PROTOTYPE SENSORS

### 2.1 Introduction

Figure 1 shows the layout of the (4-inch diameter,  $280\mu\text{m}$  thick) First Prototype wafer. Figure 2 (including its Details A, B, C, D, E, and F) illustrates the *n*-side of Tile 1 after processing. Figure 3 shows a bond pad region. Figure 4 (including its Details A, B, and C) illustrates features of Tile 2. Figure 5 shows the Tile 2 i/o bus structure. Figure 6 shows the guard rings. Figure 7 illustrates the second metal pattern. Figure 8 shows the structure known as the bias grid.

### 2.2 Cell Geometry

On the accompanying figures, rows are labelled in the horizontal direction, columns in the vertical. The active area of each tile is divided into 16 units, a unit being defined as a group of pixels that use a common amplifier chip. The geometry of each pixel cell in the First Prototypes is characterized as follows:

- Number of pixel cells per readout chip:  $164 \times 18$
- Total number of pixel cells:  $47232 (= 16 \times 164 \times 18)$
- Pixel cell dimensions:  $50 \times 400\mu\text{m}^2$ . (This is larger than the production sensors' pitch in order to match the prototype electronics.)
- Cells that lie in columns which would not be adjacent to a chip's bump pads if they were  $400\mu\text{m}$  long are elongated to  $600\mu\text{m}$ . (See Figure 2, Detail B, and Figure 4, Detail B.)

### 2.3 $n$ -side Isolation and Implant Dimensions

The principal difference between the two tiles is their technology for  $n$ -side isolation. Tile 2 uses p-spray[3], and Tile 1 uses p-stops. On the First Prototype wafers, regions that use the different isolation techniques are separated by a low precision mask.

In Tile 1, the  $n$ -type implants are isolated from one another by p-stops of the individual, or "atoll," design. This choice provides a low inter-pixel capacitance. Pairs of units are additionally surrounded by a common p-stop frame. The dimensions of Tile 1 implants are as follows:

- $n^+$  implant width:  $23\mu\text{m}$
- $p^+$  implant width:  $5\mu\text{m}$
- gap between  $n$ -type and  $p$ -type implants:  $6\mu\text{m}$
- gap between neighboring  $p^+$  implants:  $5\mu\text{m}$ .

Complete dimensions of the structures on Tile 2 are shown in Figure 4, Details A and B. For each pixel cell, the mask width of the central  $n$ -implant is  $13\mu\text{m}$ , while the floating  $n$ -implant that surrounds it is  $6\mu\text{m}$  wide. The spacing between those structures is  $6\mu\text{m}$ . The floating implant serves to keep the distance between implants (and consequently the inter-implant electric field) small without compromising the relatively large distance, and hence low capacitance, between neighboring channels. In both tiles, corners are rounded to reduce electric fields. (See for example Figure 2, Detail D.)

### 2.4 $n$ -side Guard Ring

The design of both tiles'  $n$ -side edge region (see Figure 6) is guided by the concern to minimize the possibility of electrical arcs between the sensor and the electronics which are only a bump's diameter away. There is an inner guard ring which consists in a metallized  $n^+$  implant. On Tile 1 the implant has width  $86.5\mu\text{m}$ ; on Tile 2 the width is  $90\mu\text{m}$ . On Tile 2 this inner ring can be used for biasing the whole array (see Section 2.12). Beyond the inner ring is an outer region covered with  $n^+$  implant. The inner ring and

outer region are separated by a gap. On Tile 1, that gap has total width  $30\mu\text{m}$  and is unimplanted. To provide electrical isolation, a  $10\mu\text{m}$  wide p-stop is placed in the center of the gap. On Tile 2, the gap is  $8\mu\text{m}$  wide, and electrical isolation is provided by the p-spray implant which covers the whole device.

Contact pads to the  $n$ -type implant appear in the four corners of the tile. On each tile, one of these contact pads bears a label so that the orientation of the tile is uniquely specified. The outer  $n$ -implant is grounded externally.

## 2.5 $p$ -side Guard Ring

Both tiles use the same design[4] for their  $p$ -side guard ring. The multi-guardring structure contains 22 rings with a pitch that varies from  $20\mu\text{m}$  near the sensitive area to  $50\mu\text{m}$  near the edge. The  $p$ -implant is  $10\mu\text{m}$  wide in every ring while the gap increases from the center to the edge. The metal overlaps the implant by half of the gap width on the side of the ring facing the sensitive area. The entire guard ring structure is  $525\mu\text{m}$  wide.

## 2.6 Double Metal

A second metal layer is being tested on 30% of the First Prototypes. Devices with and without double metal do not differ in any aspect of their design other than the double metal itself, the insulator, and the addition of vias to allow access through the insulator to first metal pads. In the First Prototype program, double-metal is being tested in some (redundant) busses on Tile 2 and as routing of signals from pixels at the edge of units to preamplifiers above neighboring implants. The busses run parallel to the long side of the sensor and are located between bump bond pads and the active area. Figure 5 shows a detail of the bus structure on Tile 2.

The narrowest line in Metal 2 is  $10\mu\text{m}$  wide and  $1.5\text{--}2.0\mu\text{m}$  thick. The minimum Metal 2 spacing, which is not critical, is greater than  $20\mu\text{m}$ . In the bus structure, Metal 2 has width  $20\text{--}50\mu\text{m}$ . The contact holes are  $3 \times 10\mu\text{m}^2$  in the masks. Metal on the first layer has thickness  $1.2\text{--}1.5\mu\text{m}$ . The insulator material varies with manufacturer: one vendor uses  $\text{SiO}_2$ ; the other, polyimide. To maintain flatness of the bump pads, vias are not

located beneath them. Figure 7 shows the second metal design.

Devices that have Metal 1 but not Metal 2 are completely functional. In the devices with both metal layers, the outermost four rows of pixels are not connected by bumps directly to their preamplifiers (i.e., their bump pads have no vias). Signals from pixels in those rows are instead routed in Metal 2 to neighboring pixels by using the same metal pattern as appears in Metal 1 in the sensor's central region.

## 2.7 As-cut Dimensions

The wafers containing the tiles are provided by their manufacturer without dicing in order that they may be bumped first. To accommodate the busses, Tile 2 is wider than Tile 1. After dicing, the dimensions of the tiles are:

Tile 1 (default):  $18.6 \times 62.6 \text{ mm}^2$ , and

Tile 2 (default):  $24.4 \times 62.6 \text{ mm}^2$ .

It may be necessary to increase the distance between the guard ring and scribeline in order to guarantee sufficient radiation hardness. To provide for this possibility, a second scribeline is included which would give the tiles the following dimensions:

Tile 1 (enlarged):  $19.4 \times 63.4 \text{ mm}^2$ , and

Tile 2 (enlarged):  $24.4 \times 63.4 \text{ mm}^2$ .

## 2.8 Metallization

On Tile 1, the first metal has width  $14\mu\text{m}$  on the pixels. The metal width on the inner guard ring is  $6\mu\text{m}$  narrower than the implant. The masks for the metallization over the implant of Tile 2 show a width of  $12\mu\text{m}$ ,  $1\mu\text{m}$  less than the mask width of the implant.

## 2.9 Pads

The bond pads are twenty-sided polygons (approximating circles). On Tile 1 the implant has mask diameter  $21\mu\text{m}$ , or processed diameter approximately  $23\mu\text{m}$ . On Tile 2 the implant has mask diameter  $18\mu\text{m}$ . On both tiles the first and second metals have diameter  $20\mu\text{m}$ .

Bond pads are placed at the end of each pixel cell. This layout anticipates a mirrored electronics layout. The closely spaced bond pads are  $50\mu\text{m}$  apart. (See Figure 2, Details A and B). A cross section of a bond pad region is included in Figure 3.

Some pixels have no bond pads. Those cells will have no preamplifier directly above them and so must have their signals routed to bond pads on pixels a few rows away in the same column. For both tiles, the routing will use a single metal layer. Figure 2 Details C and E show the routing for Tile 1 while Figure 4 Details B and C show it for Tile 2.

Bias pads are placed in several locations on the inner  $n^+$  guard ring. They form two extra rows with the same  $50\mu\text{m}$  pitch as the pixels have. See Figure 2, Detail F for an example of  $n$ -side bias pad placement. Probing pads are placed on the inner guard ring in the region between adjacent units (see Figure 2, Detail F).

## 2.10 $p$ -side (Back Side) Design

This information concerns both tiles. A  $p^+$  implant is continuous in the area covered by pixels. The aluminization has  $30 \times 100\mu\text{m}^2$  apertures to facilitate stimulating the cells from the  $p$ -side with a laser.

## 2.11 Passivation

The passivation must be compatible with technologies for applying bumps for bonding. A  $1\mu\text{m}$  thick silicon nitride layer is used. The openings in the passivation for bump bonding have  $12\mu\text{m}$  diameter.

## 2.12 Bias Grid

To maximize the yield on assembled modules, it is beneficial to test sensors under bias prior to attaching the amplifier chips. A bias grid is integrated into Tile 2 (see Figure 8) to allow every channel to be biased on a test stand without a chip and without contacting the implants directly. A bus between every pair of columns connects to a small  $n^+$  implant “dot” near each pixel. When bias is applied (through a probe needle) to the grid via the inner guard ring of the  $n$ -side, every pixel is biased by punchthrough from its dot. (The use of p-spray facilitates this technology since the elimination of need for photolithographic registration permits the distance between  $n$ -implants to be small and hence keeps the punchthrough voltage low.) Once a chip has been attached, the grid is no longer used for biasing the cells. It nonetheless maintains any unconnected pixels (i.e., bad bumps) near ground potential. The punchthrough dot sacrifices 0.8% of the pixel’s active area.

## 2.13 Tolerances

The following tolerances are required:

- Uniformity of thickness:  $\pm 10\mu\text{m}$
- Mask alignment:  $\pm 2\mu\text{m}$

## 2.14 Sensor Electrical Properties

The following is a summary of the required electrical properties:

- Initial depletion voltage: 50–150V
- Initial maximum operating voltage:  $\geq 200\text{V}$
- Initial leakage current at  $V_{\text{depletion}} + 10\text{V}$ :  $< 100 \text{ nA/cm}^2$
- Initial oxide breakdown voltage:  $\geq 100\text{V}$ .



## 2.15 Processing

The following processing requirements are made:

1.  $n^+$  implant dose:  $> 10^{14}/\text{cm}^2$ .
2. concerning  $n$ -side isolation:
  - for Tile 1, the  $p^+$  implant dose is  $\geq 10^{13}/\text{cm}^2$ .
  - for Tile 2, the  $p$ -spray effective dose in silicon is  $(3.0 \pm 0.5) \times 10^{12}/\text{cm}^2$ .
3. Back ( $p$ -side) contact dose:  $> 10^{14}/\text{cm}^2$ .
4. Implant depth after processing is  $\geq 1\mu\text{m}$ .

## 2.16 Radiation Hardness

The following specifications will be required of Second Prototype and production sensors. They are not required of First Prototype sensors. The properties of irradiated First Prototype sensors are nonetheless being studied.

The production sensors must have the following performance after an irradiation of  $10^{15} \text{ p/cm}^2$ :

1. Breakdown voltage:  $> 500 \text{ V}$ .
2. Depletion voltage (for  $300\mu\text{m}$  sensors):  $< 800 \text{ V}$ .
3. Leakage current (measured at  $-5^\circ \text{ C}$ ) after one month of annealing at  $20^\circ \text{ C}$  (for  $300\mu\text{m}$  sensors):  $< 125\mu\text{A}/\text{cm}^2$  or  $< 25 \text{ nA}$  per pixel cell.

## 3 DESIGN VARIATIONS STUDIED ON SINGLE-CHIP SENSORS

On each wafer, three of the seventeen single-chip sensors have all of the design features of Tile 1. Three others have the features of Tile 2. Among

the remainder, two evaluate a common p-stop design, one combines the common p-stop with p-spray, one studies a variety of p-stop geometries, and one evaluates three different bricking patterns. In the region of the wafer that uses p-spray, there are an additional 3 devices which explore techniques for minimizing cross talk, implementing bricking, and modifying implant geometries and gap sizes.

“Bricking” is the offsetting of pixel cells in neighboring rows by half a pixel length. Bricking improves the  $z$  resolution for double hits and reduces the cross talk coupling by distributing the capacitance over four neighboring cells rather than two. The challenge to the implementation of bricking comes from the fact that bricked sensor cells are not directly adjacent to the bump pads of the mirrored bump pad geometry of the (nonbricked) readout chip. Several solutions to this problem are being examined on the single-chip sensors. In one option, the bump pad is placed above a neighboring channel’s implant and then routed in single metal to the implant which requires connection. This option produces cross talk between the two implants involved. In a second option, the routing between implants is accomplished in second metal. In the third option, called “partial bricking,” routing is avoided entirely by staggering the implants only at their ends which have no bump pads. This option complicates pattern recognition slightly. The three bricking options are illustrated in Figures 9, 10, and 11.

## 4 TESTING

Acceptance testing is being done by ATLAS only. The wafer has test structures for monitoring flat band voltage, layer thickness, implant resistivity, aluminum sheet resistance, etching uniformity, and alignment.

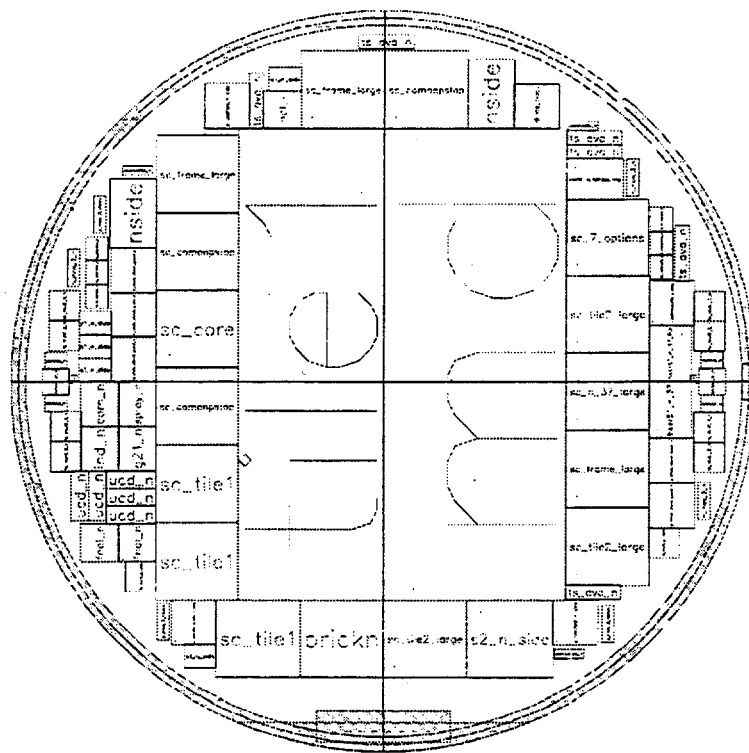


Figure 1: The layout of the 4-inch First Prototype wafer.

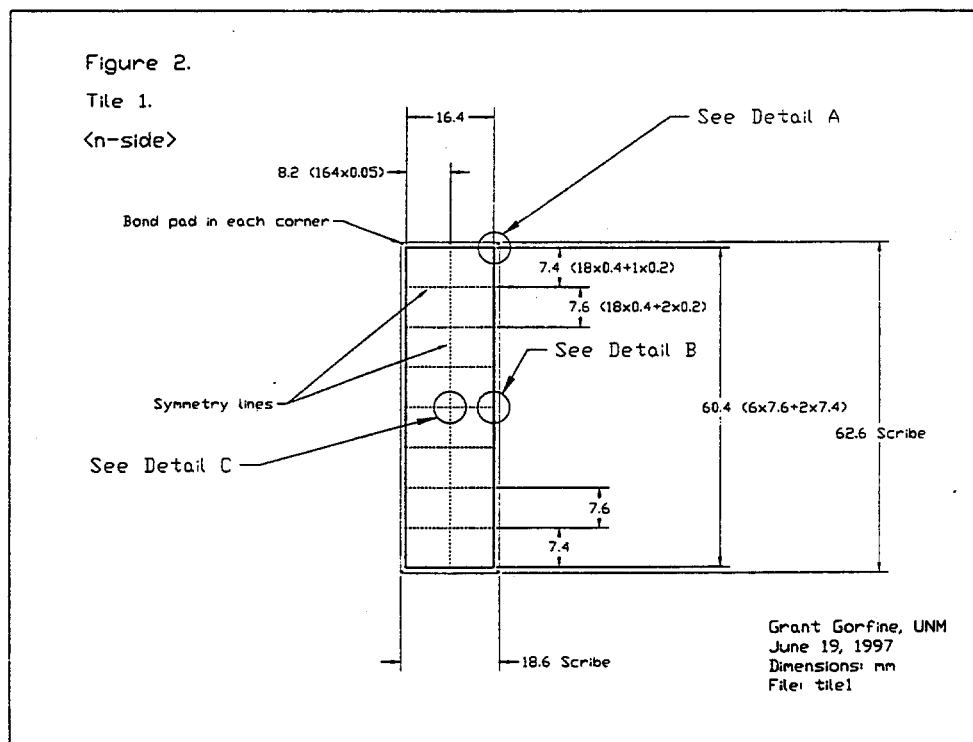


Figure 2: The Tile 1 concept.

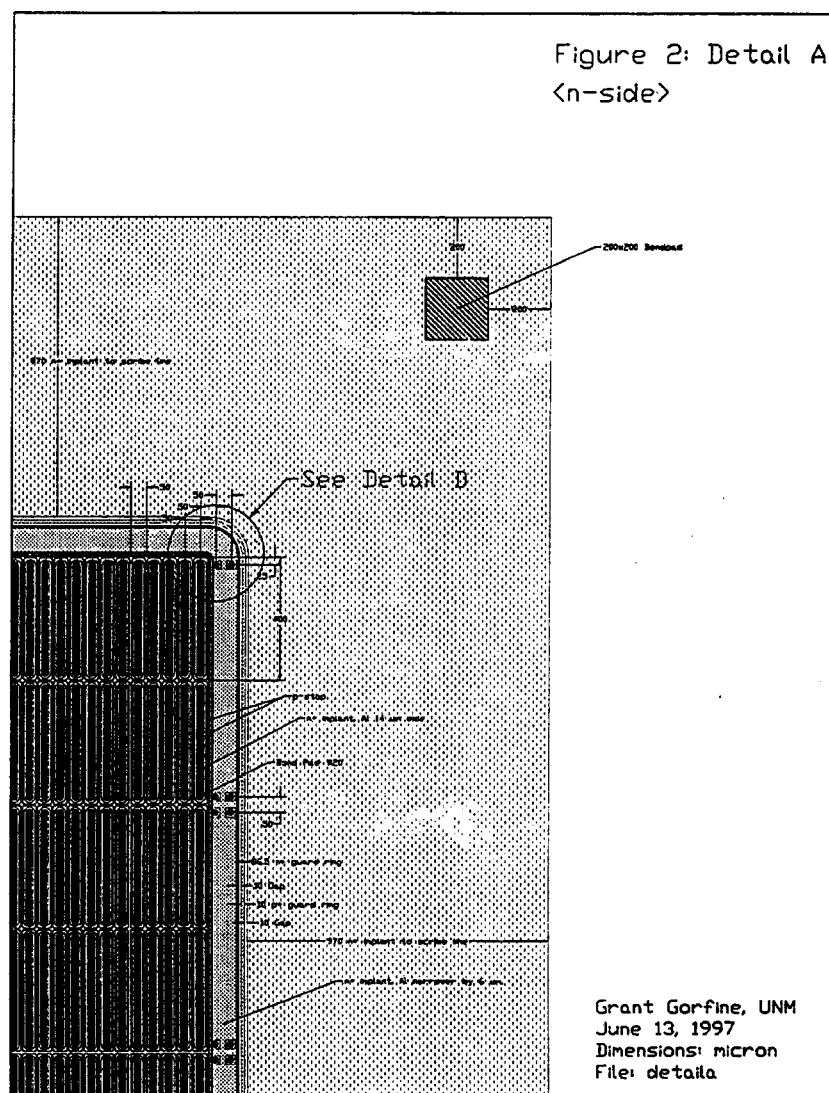


Figure 2a: Corner detail of Tile 1.

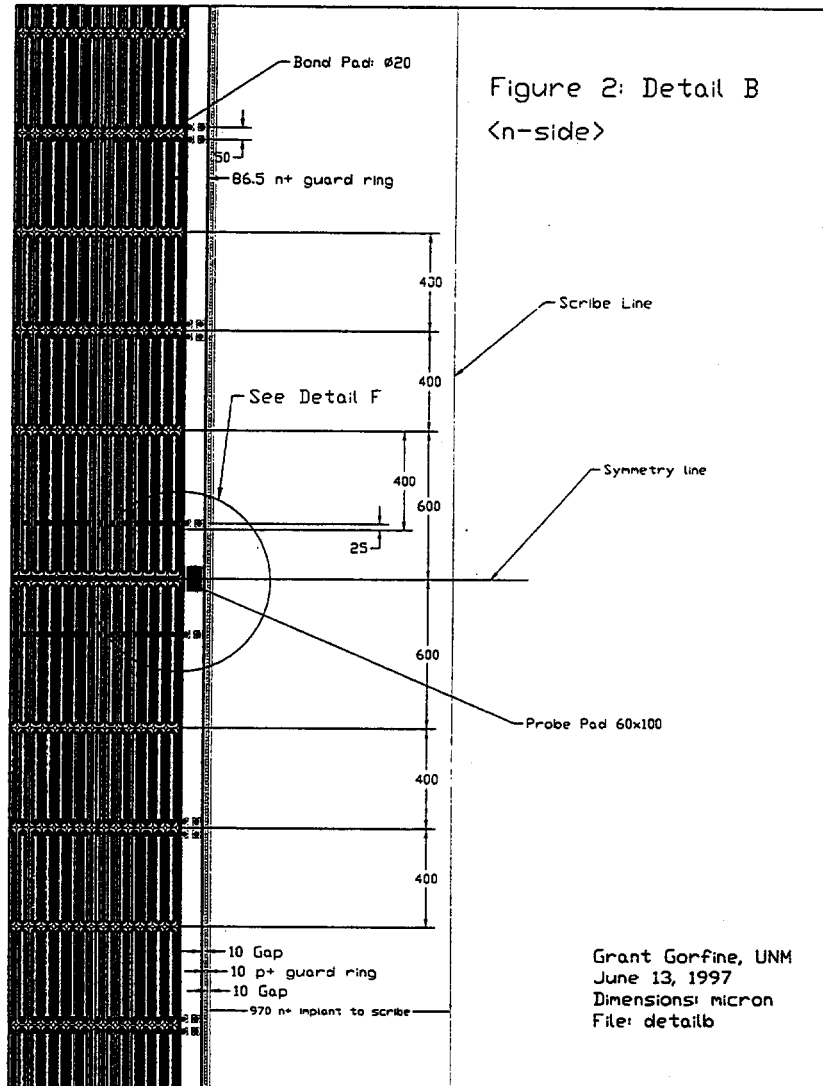


Figure 2b: Detail of Tile 1 showing a region between units in which cells of length 600  $\mu\text{m}$  are used.

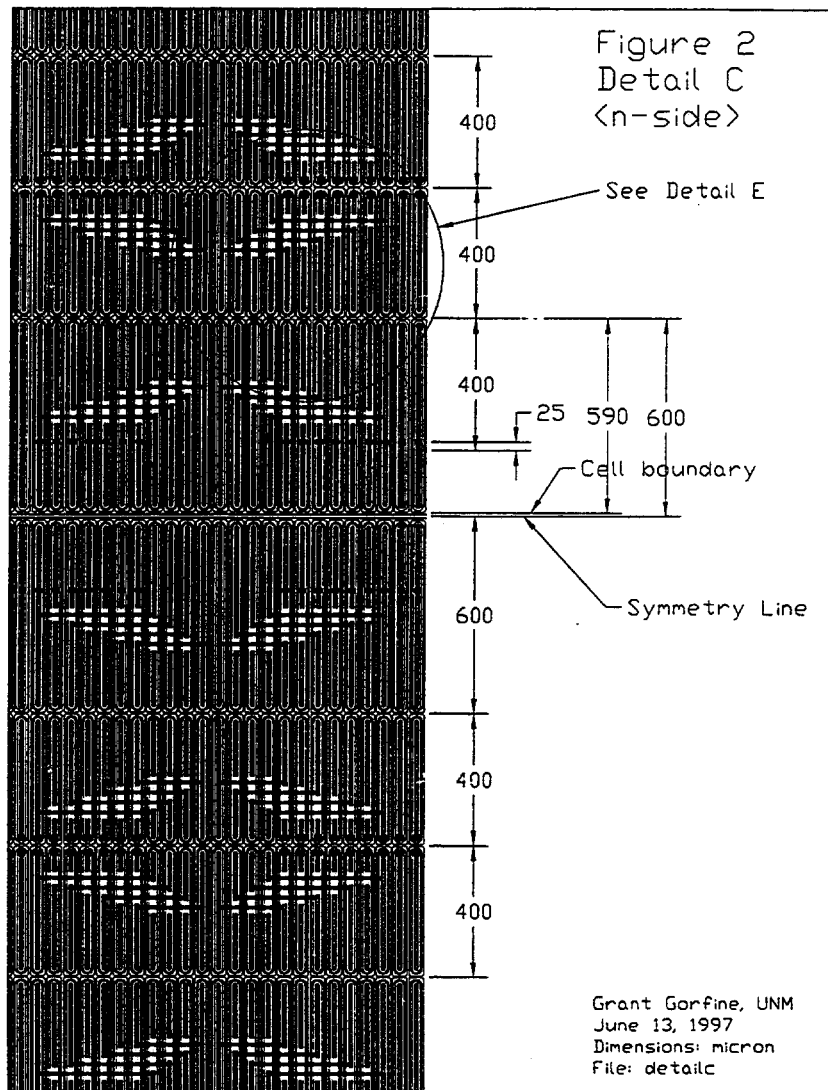


Figure 2c: Detail of Tile 1 showing first metal traces which route signals from implants at the edges of their units to the preamplifiers above neighboring implants.

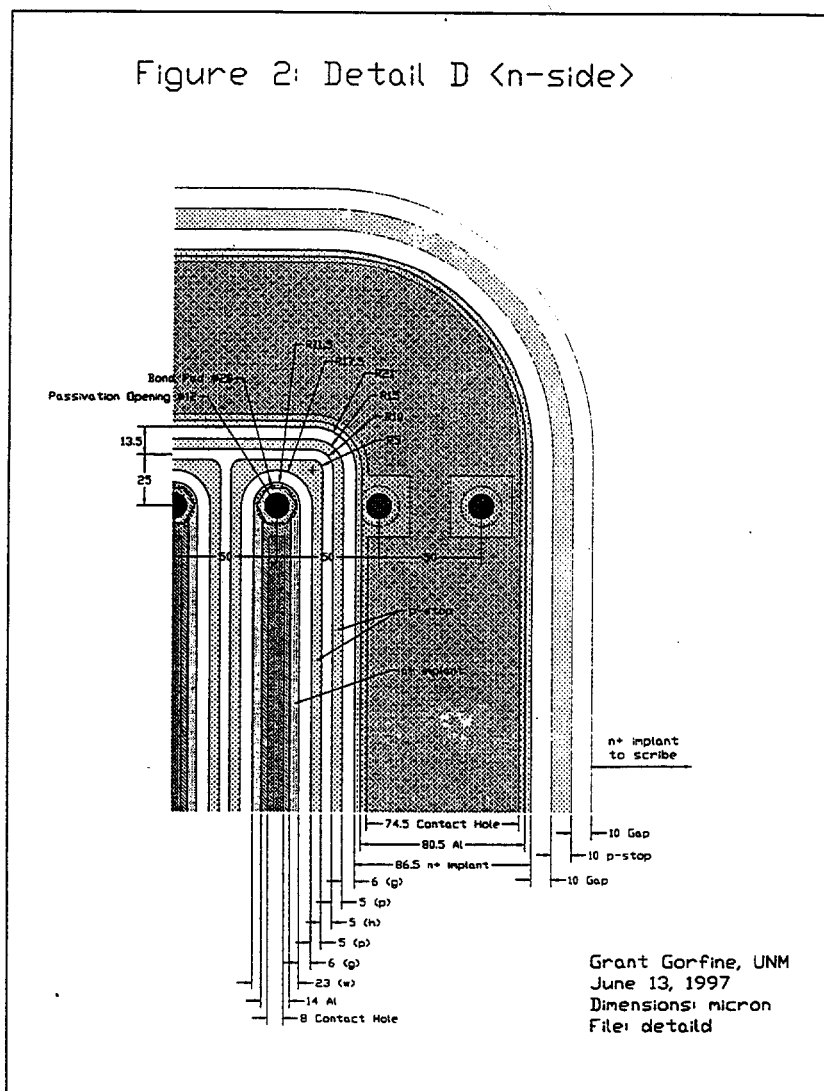


Figure 2d: Detail of Tile 1 showing the corner of the *n*-side guard ring and the isolation implants.



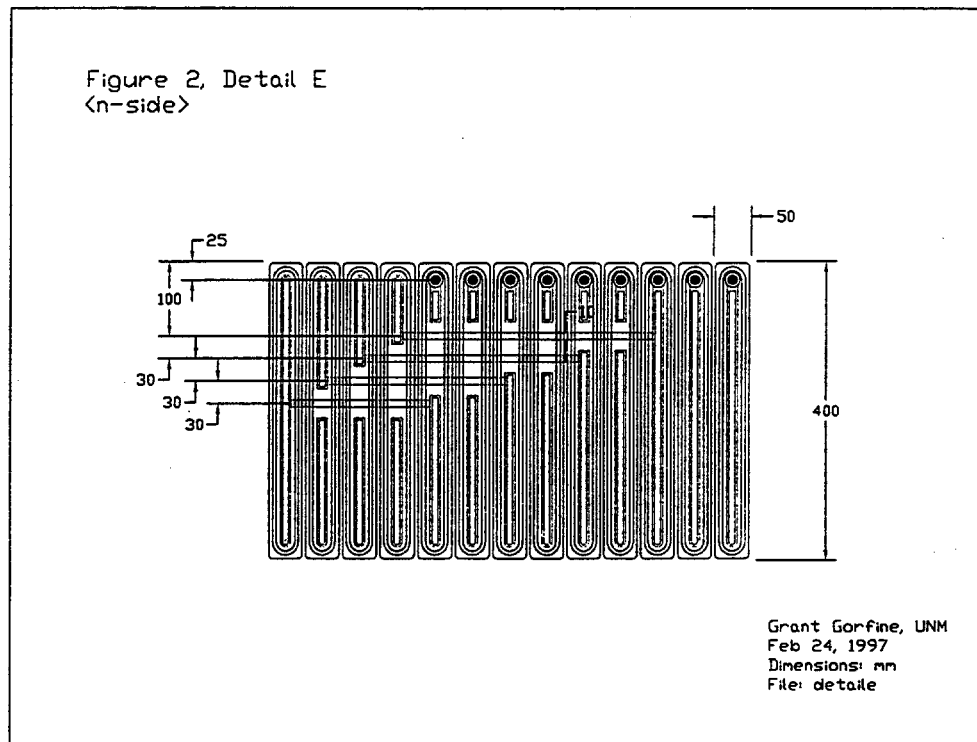


Figure 2e: Detail of Tile 1 showing the first metal near the edge of a unit.

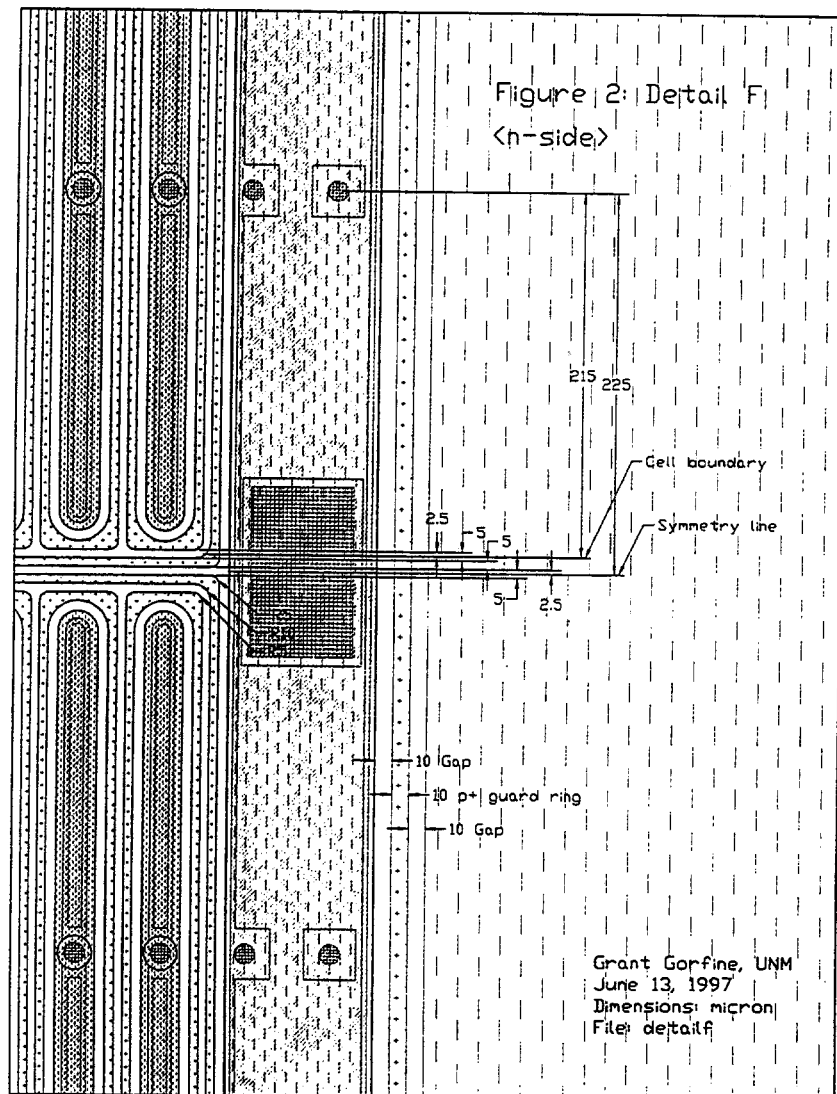


Figure 2f: Detail of Tile 1 showing the structure of isolation implants at the boundary between units.

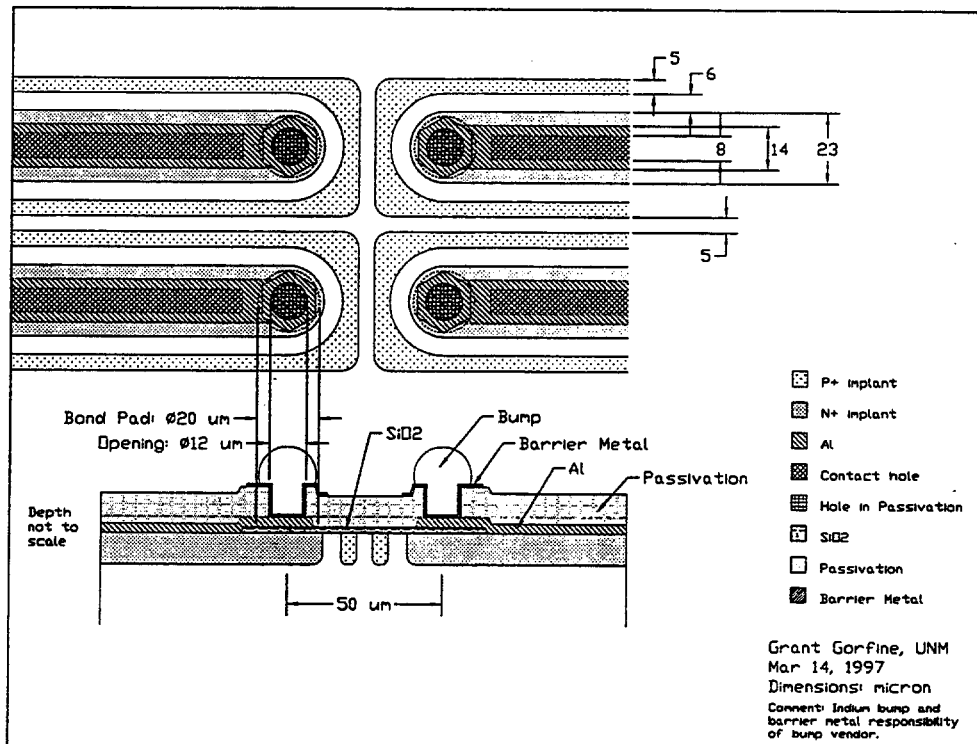


Figure 3: Concept of a Tile 1 bond pad region.

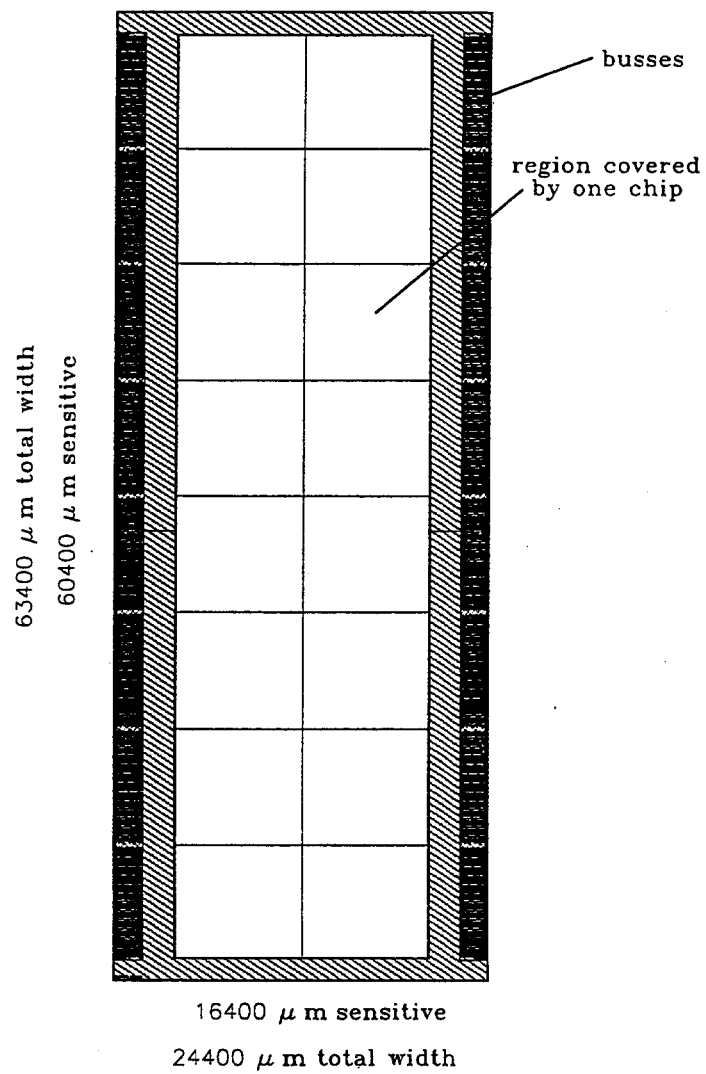


Figure 4: The Tile 2 concept.

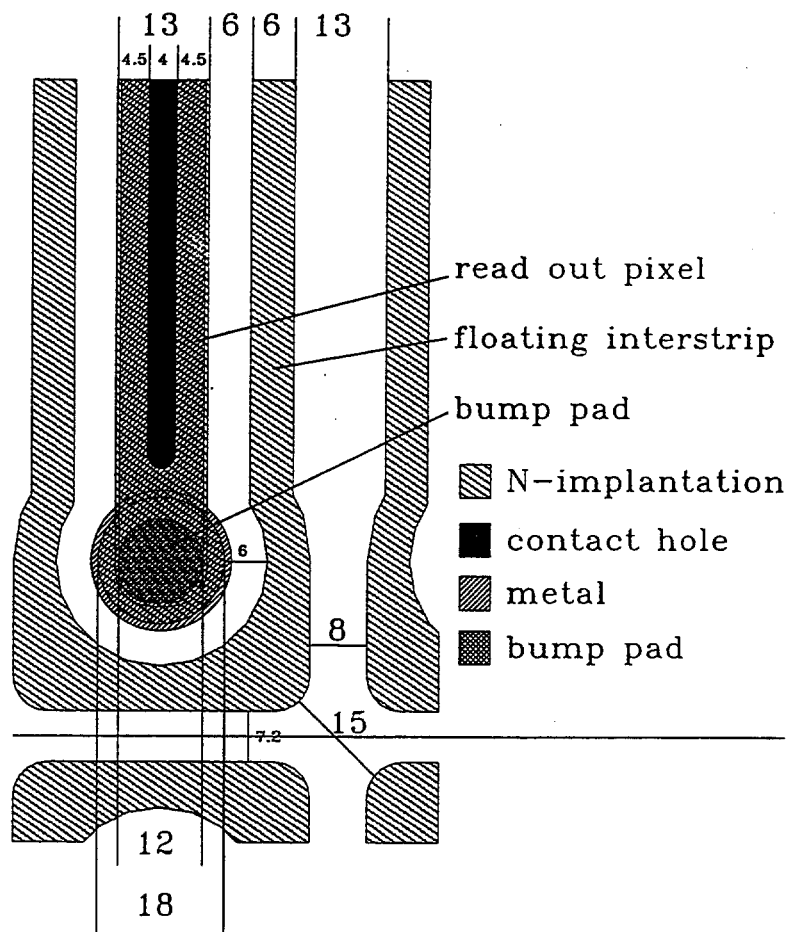


Figure 4a: Portion of a pixel cell in Tile 2.

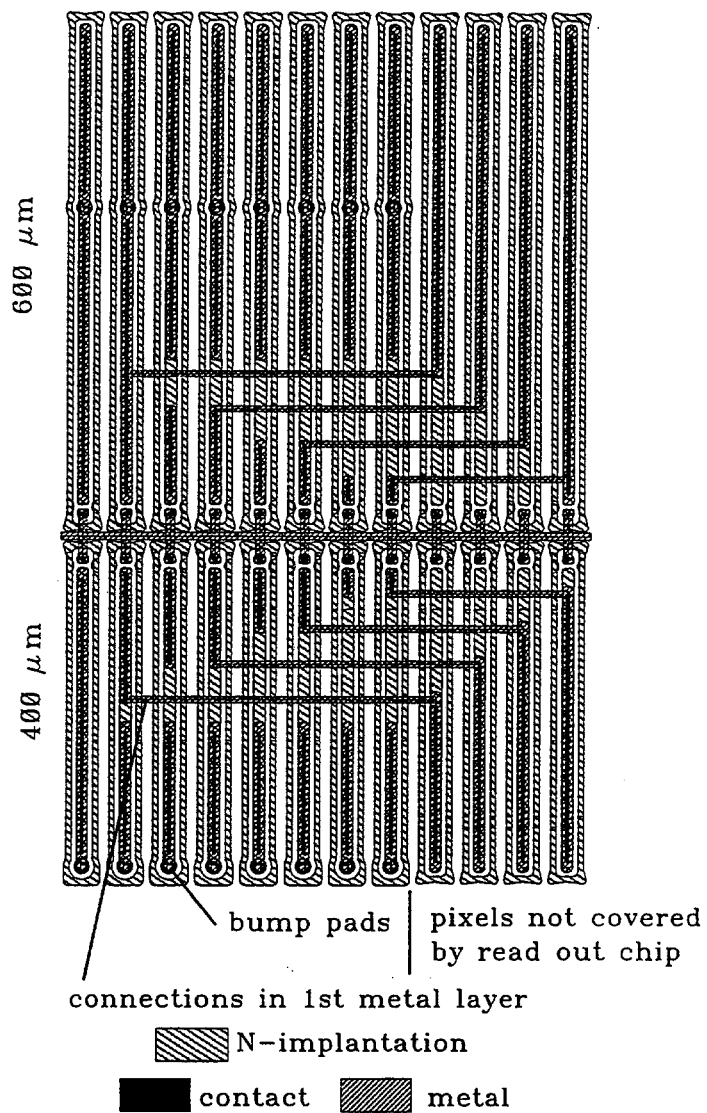


Figure 4b: Detail of Tile 2 showing first metal traces which route signals from implants at the edges of their units to the preamplifiers above neighboring implants.



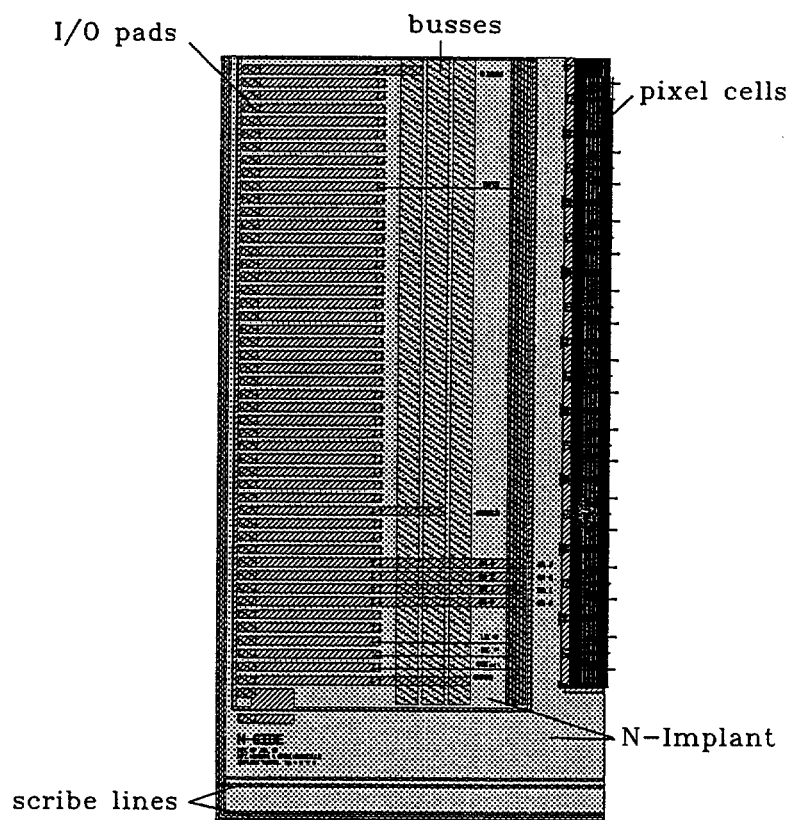


Figure 5: I/O busses on Tile 2.



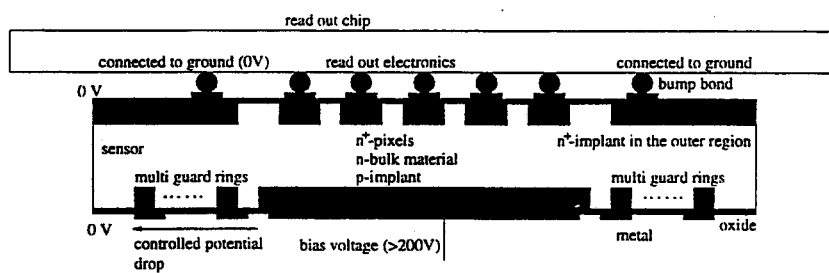


Figure 6: A cross section of a tile showing the guard rings.

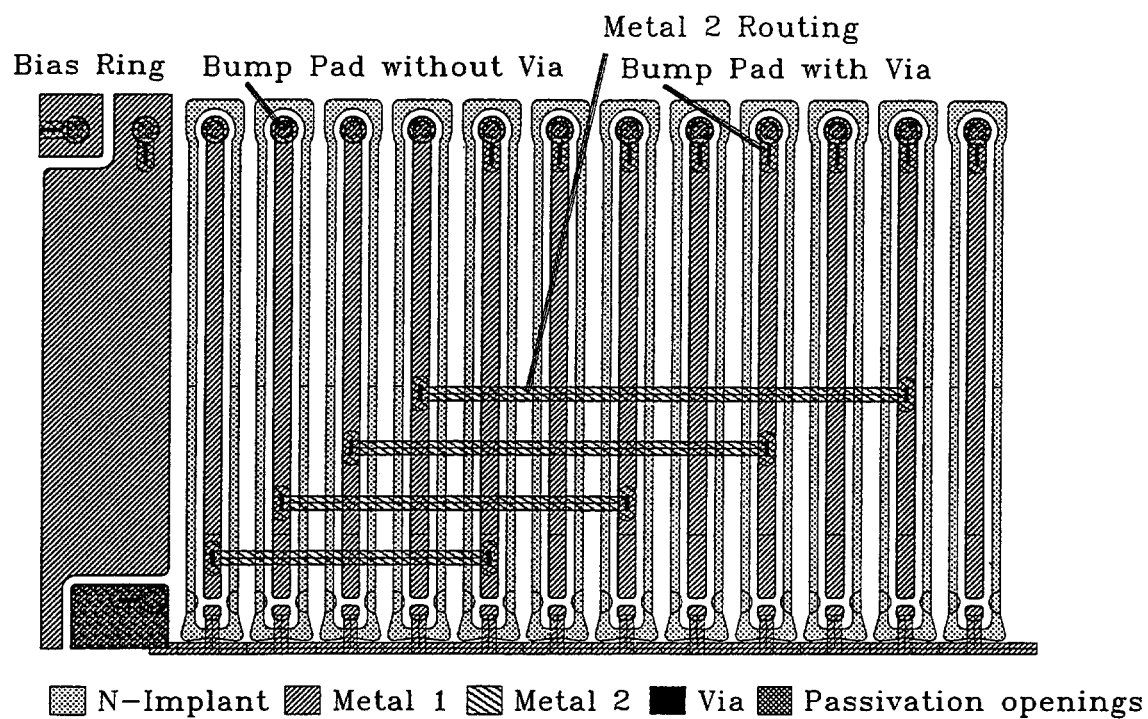


Figure 7: The Metal 2 routing.

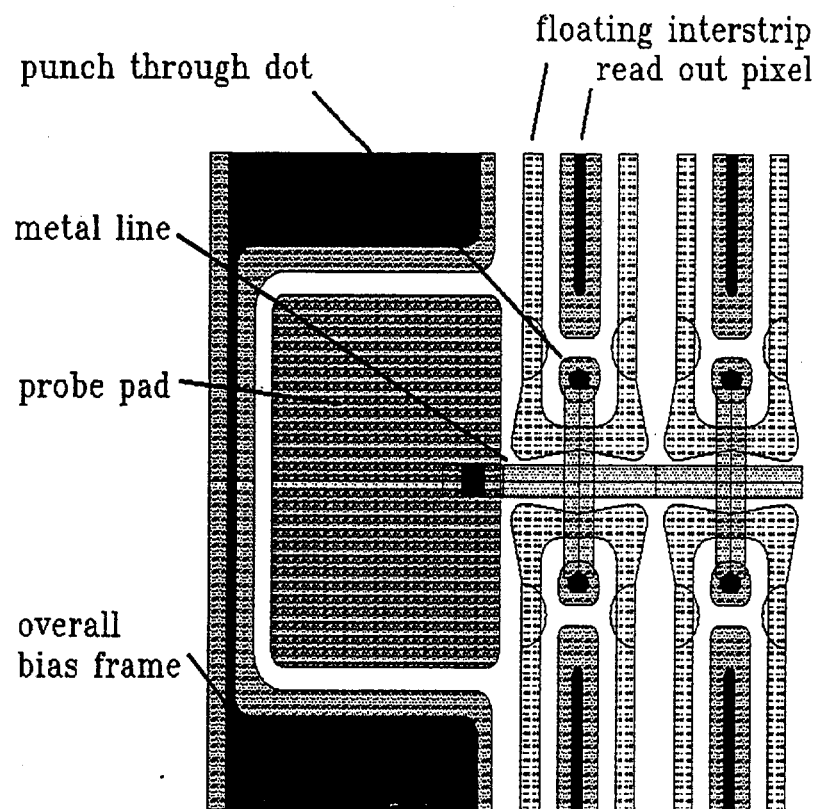


Figure 8: A section of the bias grid.

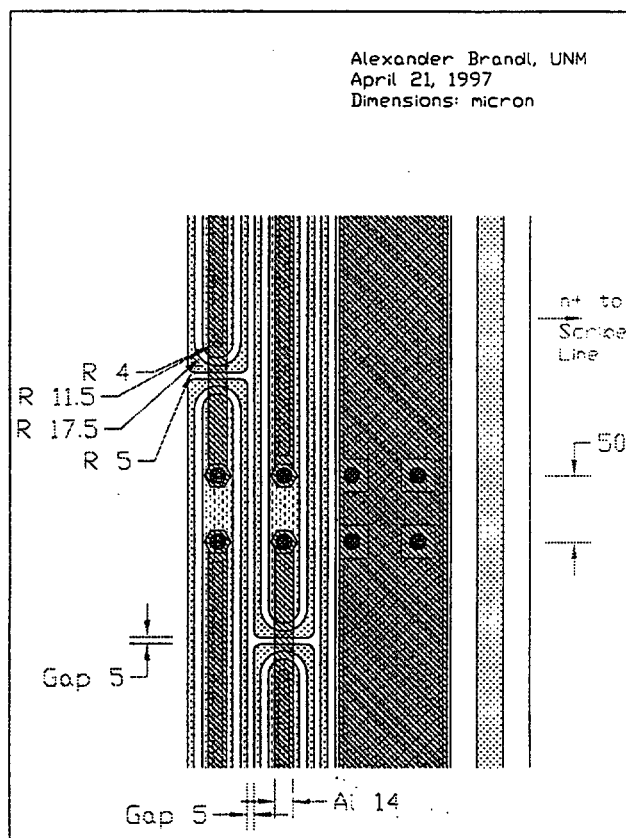


Figure 9: Bricking with single-metal routing.

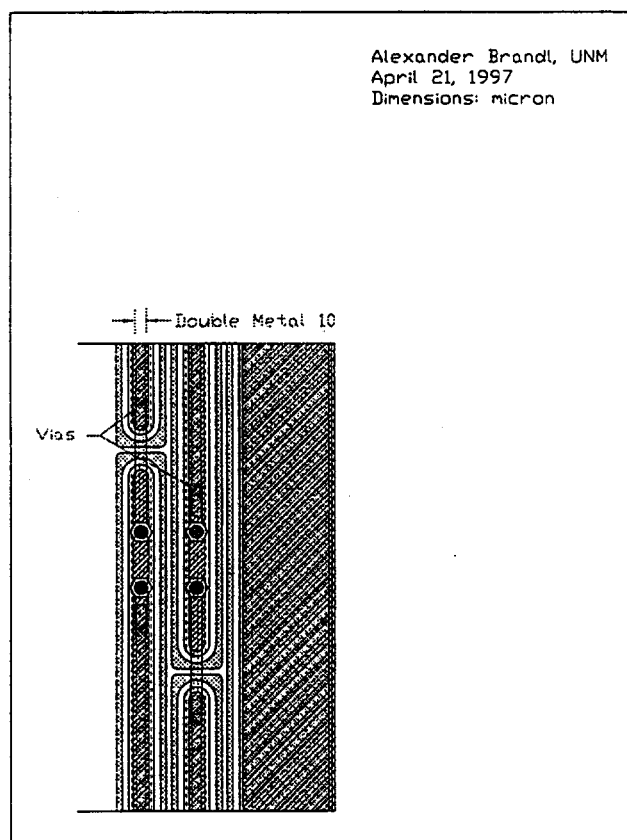


Figure 10: Bricking with double-metal routing.

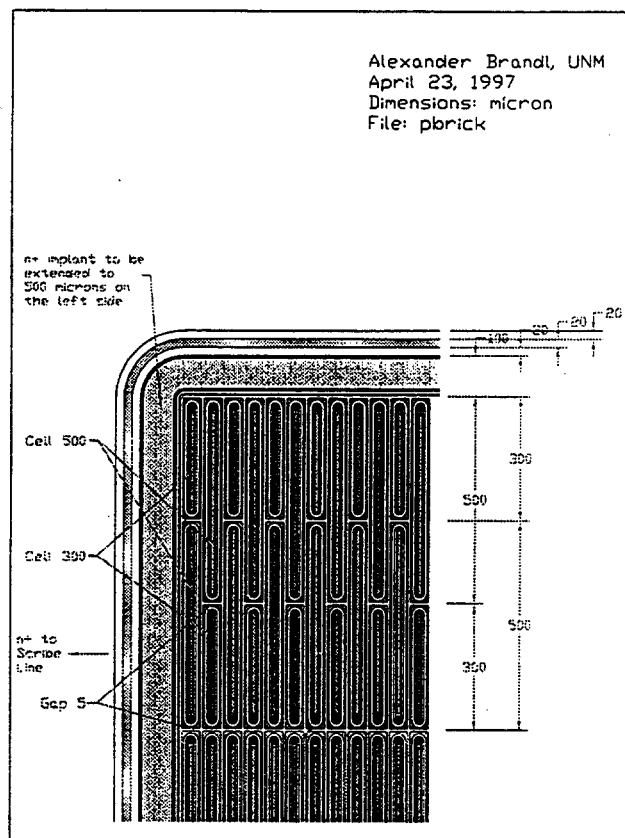


Figure 11: Partial bricking.

## References

- [1] The ATLAS Collaboration, *ATLAS Inner Detector Technical Design Report*, CERN/LHCC/97-17, April 1997.
- [2] T. Rohe et al., *Sensor Design for the ATLAS-Pixel Detector*, Proc. Seventh Pisa Meeting on Advanced Detectors, Isola d'Elba, May 1997, to be published in *Nucl. Instr. and Meth.*
- [3] R.H. Richter et al., *Nucl. Instr. and Meth. A* 377 (1996) 412-421.
- [4] A. Bischoff et al., *Nucl. Instr. and Meth. A* 326 (1993) 27-37; B.S. Avset, *Nucl. Instr. and Meth. A* 377 (1996) 397-403.

